Tuning the properties of high-T_c superconductor & Sr_2IrO_4, and exploring transport through single nanocrystals

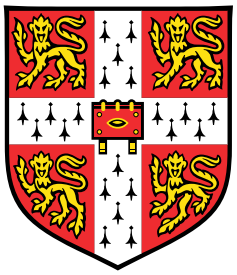

Wenting Guo

Department of Physics
University of Cambridge

This dissertation is submitted for the degree of
Doctor of Philosophy

King's College

January 2019

I would like to dedicate this thesis to my loving parents ...

Declaration

I hereby declare that except where specific reference is made to the work of others, the contents of this dissertation are original and have not been submitted in whole or in part for consideration for any other degree or qualification in this, or any other university. This dissertation is my own work and contains nothing which is the outcome of work done in collaboration with others, except as specified in the text and Acknowledgements. This dissertation contains fewer than 65,000 words including appendices, bibliography, footnotes, tables and equations and has fewer than 150 figures.

Wenting Guo
January 2019

Abstract

This thesis is composed of three projects including the AC magnetic susceptibility study of high-temperature superconductor $YBa_2Cu_3O_{7-\delta}$, the ionic-liquid gating study of the Mott insulator Sr_2IrO_4, and the single-electron study of quantum dot device with self-assembled nanocrystal PbS. Chapter 1 covers a general introduction to all three projects. The basic background and the motivation to each project is presented.

Project I is covered in Chapter 2, Chapter 3, and Chanpter 4. The first part of Chapter 2 is a theoretical introduction to the Bardeen–Cooper–Schrieffer theory of superconductivity with its main conclusions presented. This chapter builds a basis for the use of high pressure technique to $YBa_2Cu_3O_{7-\delta}$ in the later chapters. The rest of Chapter 2 reviews the work in the study of high-temperature superconductors, especially on $YBa_2Cu_3O_{7-\delta}$, on both experiments and theories and the possible applications of high-temperature superconductors. Chapter 3 introduces the $YBa_2Cu_3O_{7-\delta}$ sample preparation process and the characterisation. A dry cryomagnetic equipment was employed for the measurement. The results and the discussion are presented in Chapter 4.

Project II is described in Chapter 5, Chapter 6, and Chapter 7. Chapter 5 firstly introduces the background knowledge of the gated material Sr_2IrO_4 and the technical details of the ionic-liquid gating technique. Then the sample growth and the characterisation are presented. The fabrication process of Sr_2IrO_4 and $SrTiO_3$ (material for a control experiment) are described in Chapter 6. Chapter 7 covers the measurement and the result of the fabricated devices and related discussion.

Project III ranges from Chapter 8, and Chapter 9. A literature review of quantum-dot devices and self-assembled nanocrystals is presented in Chapter 8. The experimental design of this nanocrystal quantum dot device is also included. Following it, the fabrication process of quantum-dot devices and the techniques used for fabrication are introduced in the start of Chapter 9. Chapter 9 also gives a descrition of the probe-station for measurements. The results and discussion of the measurements are covered in the last section of Chapter 9.

Chapter 10 summarises and concludes the three projects stated above and gives some suggestions about the directions for future work.

Table of contents

List of figures

List of tables

Chapter 1

Motivation and Outline

This thesis consists of three parts with each focused on an individual project. The first part is the study on the magnetic susceptibility of the high-temperature superconductor $YBa_2Cu_3O_{7-\delta}$ under high hydrostatic pressure. The second part is the ionic liquid gating experiment on the Mott insulator Sr_2IrO_4. The third part is the study of the Coulomb blockade behaviour of self-assemblied zero-dimensional quantum dots.

High-temperature superconductivity is one of the most mysterious topics in fundamental physics research. Scientists are chasing after it not only for the fun of solving a complicated problem but also for the promisingly industrial applications of it. Superconductors could help reduce enormously the large energy loss during electric power supply, construct magnetic levitation trains to send passengers across continents in few hours, and form superconducting qubits in quantum a computer. However, due to the low superconducting transition temperatures ($\sim$ few kevin), the applications of superconductors have to be accompanied with liquid helium with a boiling temperature of 4.2 K, which to a great extent limits its spread. The discovery of the copper-oxide high-temperature superconductor family in 1986 [12] turned a new page in history with 135 K the highest superconducting transition temperature so far [13]. Greatly inspired by this discovery, physicists have spent decades trying to understand the source of such a high transition temperature. $YBa_2Cu_3O_{7-\delta}$ is the one of the most extensively studied members in the high-temperature copper-oxide superconductor family. As $YBa_2Cu_3O_{7-\delta}$ can be synthesized in a very pure form, many experiments have been designed to investigate every aspect of the behaviour. Physicists have found out that when the oxygen concentration $7-\delta$ of $YBa_2Cu_3O_{7-\delta}$ is gradually reduced from 7 to 6, the superconducting transition temperature initially rises up to a peak and thend drops slowly until the superconducting transition disappears at around 6.3 [14]. This is called chemical doping. Material with oxygen deficiency has been thoroughly studied and can be grown without clear defects and other disorder inside. This helps dramatically in clarifying the

real mechanism of high-temperature superconductivity without other sources of interference. Plots of the behaviour of $YBa_2Cu_3O_{7-\delta}$ in its underdoped region and the normal region with less oxygen have been drawn almost completely. However, the part related to the overdoped $YBa_2Cu_3O_{7-\delta}$ and the transient region connecting the underdoped and the overdoped region has received relatively less attention. Until now, no agreement about the mechanism of high-temperature conductivity has been reached, and the study of overdoped $YBa_2Cu_3O_{7-\delta}$ has a critical role to play in the quest of understand it.

The main reason for people putting less time and energy into the study of overdoped region is that overdoped $YBa_2Cu_3O_{7-\delta}$ cannot be achieved simply by increasing the oxygen concentration in $YBa_2Cu_3O_{7-\delta}$, which will become chemically unstable and decompose. The more common way of synthesizing overdoped $YBa_2Cu_3O_{7-\delta}$ is to replace Y by Ca to obtain $Y_{1-x}Ca_xBa_2Cu_3O_{7-\delta}$ [15, 16], or to replace Y by Tl and some of Cu to form $Tl_2Ba_2CuO_{6+\delta}$ [17]. With new substitutes having different atomic sizes from the old ones, the crystal structure will change slightly simultaneously. The other factor needing consideration when we are studying this type of overdoped $YBa_2Cu_3O_{7-\delta}$ is that the introduced atoms will also bring in their own physical properties, which complicate the original pure $YBa_2Cu_3O_{7-\delta}$ system. To design better controlled experiment, one option is to use high pressure to tune the optimally doped $YBa_2Cu_3O_{7-\delta}$ into the overdoped region. This is the original idea of the first part of this thesis. Hydrostatic pressure tuning introduces neither extra dissimilar atoms nor chemical disorder into the original system. The other advantage of using hydrostatic pressure is that the whole pressure process is completely controllable and reversible within a reasonable range, which provides the convenience to repeat and to double check results.

In this thesis, an optimally doped $YBa_2Cu_3O_{7-\delta}$ was pressurised between two diamond anvils up to 90 kbar in a small pressure cell. The AC magnetic susceptibility of it was measured by two coils, one acting as the driving coil and the other one the pick-up coil. The structure of the pressure cell and the principle of AC magnetic susceptibility measurements of type-II superconductors will be firstly introduced. Following it, the result of measurements of the AC magnetic susceptibility of $YBa_2Cu_3O_{7-\delta}$ under hydrostatic pressure will be presented and discussed. Finally a conclusion will be given followed by suggestions for possible improvement of this experiment.

As physicists are focusing on the study of $YBa_2Cu_3O_{7-\delta}$, an other approach with the same aim is proposed. This is to study other materials sharing some kind of similarity with $YBa_2Cu_3O_{7-\delta}$. Sr_2IrO_4 enters the field of view with a similar crystalline structure to both the copper-oxide high-temperature superconductor family and the *p*-wave superconductor Sr_2RuO_4. Sr_2IrO_4 is an insulator with tetragonal crystalline structure. Thus the proposed research is focused on the quesitons, why with only one element Ru replaced by Ir, Sr_2IrO_4

shows so much difference from Sr_2RuO_4 and what is the connection between the insulating state of Sr_2IrO_4 and that of La_2CuO_4, the parent material of the first discovered copper-oxide high-temperature superconductor [12].

The layered material Sr_2IrO_4 has a tetragonal structure $I4_1/acd$ with IrO_6 octahedra rotating around the c-axis by 11.8°, which is similar to the structure of the La_2CuO_4. However, due to the rotation of the IrO_6 the lattice parameter of the unit cell is twice the size of La_2CuO_4 unit cell. Cooling from room temperature down to around 240 K, a ferromagnetic transition appears, indicated by an upturn in the DC magnetic susceptibility. Surprisingly, with the detection of spin structure by neutron scattering, it is found that there is actually a canted antiferromagnetic transition also appearing in La_2CuO_4. A later spectroscopic study further gives some evidences about the d-wave gap feature. Counterintuitively, Sr_2IrO_4 with a d-band does not behave like a metal giving a decreasing resistance as temperature decreases. With the strong spin-orbit coupling energy from Ir^{2+}, even relatively moderate Coulomb interaction between atoms is able to open a gap leading to the robust insulating behaviour in Sr_2IrO_4. This gap vanishes quickly with small amount of oxygen depletion, but persists under high hydrostatic pressure up to 80 GPa.

Searching for the potentially new high-temperature superconductor family, physcists have been trying to tune Sr_2IrO_4 into the metallic regime with a series of methods. One is to use chemical doping by substituting Sr or Ir atoms by other atoms with different number of valence electrons. $Sr_{2-x}La_xIrO_4$ has a more filled band, but leaves the spin-orbit coupling unchanged. The substitution of an Ir atom will reduce the strength of spin-orbit coupling in materials like $Sr_2Ir_{1-x}Ru_2O_4$ and $Sr_2Ir_{1-x}Rh_2O_4$. These substitutions all exhibit metallic states, even if the desired superconductivity does not show up. The other way to make a metallic state is to decrease the distance between atoms by applying high pressure to the material to achieve a broadened electronic band. This method has the advantage of not introducing disorder into the material. However, with pressure as high as 80 GPa, the insulating behaviour still persists, showing no sign of a metal-insulator transition.

Besides the tuning methods stated above, there is another method becoming popular recently in condensed matter physics field, which is the ionic liquid gating technique. This technique applies a gate voltage to an ionic liquid placed on the top surface of the material being studied to generate a very thin polarised capacitance layer right above the samples. As calculation and practice shown, a much higher electric field is able to be produced by ionic liquids than by conventional solid dielectrics. Some insulators have been tuned into the superconducting state with this technique. This tuning method will not only produce remarkably large electric fields to introduce more carrier density to the surface of the samples than the conventional chemical doping method, but also there is no disorder arising from

the introduced foreign atoms. Furthermore, by changing the gate voltage, one can switch between hole doping and electron doping. The aim of this thesis is to study Sr_2IrO_4 by ionic liquid gating to explore its potential superconductivity.

Zero-dimensional quantum-dot devices attract substantial attention from both academia and industry for their simplicity in showing quantum phenomenon and the great potential in industrial application since firstly been observed in a semiconductor microcrystal [18] in 1982.

A quantum dot is literally a region of material in which the potential confines electrons in all three dimensions, so that the electrons' energy levels are quantised and the number of electrons in the dot is well-defined. While they may have useful optical properties and so not need to be electrically contacted for transport measurements, the dot must be sandwiched between source and drain electrodes with tunnel barriers in between. By controlling the bias and any gate nearby, the inflow and the outflow of electrons to and from the quantum dot one by one can be realised. Thus this type of device is also referred as "single-electron transistor". This quantisation effect is potentially relevant to solid-state quantum computation. This is analagous to the current gate operation we are using in the computers every day, but with higher speed and less driven bias. Besides, quantum dot device can be fabricated into very small size and integrated to a higher device density. In biology field, quantum dots provide many useful applications as well, like highly sensitive cellular imaging [19].

Initially, quantum dot devices made out of a semiconductor or metal particle were a few microns in size. However, with the fast development of nano-fabrication techniques recently, much smaller quantum dots can be produced now. If synthesised by a chemical method, nanocrystal with radius of 2 to 50 nm can be achieved. The wide range of nanocrystals gives scientists more effective ways to engineer the energy band and to control the efficiency of quantum dot devices as transistors. It is also more convenient and easy to fabricate the devices. Simply immersing substrate into nanocrystal solution for a period of time will produce a layer of self-assembled nanocrystals attached. This is very helpful for mass production in factory. But there is a hugh challenge in making electrodes close enough to the dot to make reliable contact in a way that could be scaled up from one dot to billions.

To further understand the electronic transport properties of quantum dots with PbS nanocrystal as quantum dots, we investigated various techniques in this part. Quantum dot devices with both lateral and verticle structures are explored. The vertical structure is based on a GaAs wafer consisting of two highly doped n+GaAs layers and one AlAs spacer. The lateral structure consists of two gold contacts and two gate electrodes with a nanometre-sized gap in the center fabricated on a SiO_2/Si substrate using electron-beam lithography and electroplating. Self-assembled PbS nanocrystal quantum dots were processed. Then the

measurement was conducted on the lateral fabricated devices and their results and analysis are presented. Finally a conclusion will be given as well as a prospect for future experiments.

Chapter 2

Introduction to $YBa_2Cu_3O_{7-\delta}$ and High Pressure Technique

High-temperature superconductivity has attracted phycists' attention for decades for its fascinating physics and prospect applictions in industry. $YBa_2Cu_3O_{7-\delta}$ is one member of the copper-oxide high-temperature superconductor family, which has been studied experimentally the most. $YBa_2Cu_3O_{7-\delta}$ is one of few high-temperature superconductors that can be highly purely synthesised in laboratory, which provided much advantange to experimental design, such chemical doping experiment. Though chemical doping is able to tune $YBa_2Cu_3O_{7-\delta}$ to both underdoping and overdoping levels and has provided many evidences important to understanding high-temperature superconductivity, it also introduces some chemical disorders into $YBa_2Cu_3O_{7-\delta}$ because of the mismatch of size of the substitutes [16, 20]. Aonther technique without introducing any chemical disorders is hydrostatic pressure technique. Due to the difficulty of making pressure cell and realising measurement in small pressure cell chamber, $YBa_2Cu_3O_{7-\delta}$ under extremely high hydrostatic pressure has not been fully explored before. In this project, we are aiming to explore the AC magnetic susceptibility of $YBa_2Cu_3O_{7-\delta}$ under high hydrostatic pressure (90 kbar). A piece of single crystal $YBa_2Cu_3O_{7-\delta}$ at optimal superconducting temperature was used here and tuned to overdoped region under hydrostatic pressure.

2.1 BCS Theory of Superconductivity

BCS theory was firstly proposed by Bardeen-Cooper-Schrieffer in 1957 as the first microscopic theory of superconductivity. Copper presented in 1956 that a weak attraction can cause the binding of a pair of electrons [21] (Cooper's problem). This is the foundation of the instability of the Fermi sea of electrons. The electron-phonon interaction in solid is able to

provide this required attraction, when it overrides the repulsive screened Coulomb interaction. BCS theory writes all the electrons in metal Fermi surface into an individual wavefunction, known as the BCS wavefunction [22] for ground state [23, 24]. Following this assumption, the original Cooper's problem can be solved resulting in a superconducting outcome, from which the well-known energy gap Δ between ground-state energy and normal-state energy can be deduced as:

$$k_B T_c = 1.13\hbar\omega_D \exp(-1/\xi), \tag{2.1}$$

where k_B is Boltzmann constant, T_c is superconducting transition temperature, ω_D is Debye frequency, and ξ is coupling strength. As ω_D is a measure of the strength of phonon interaction, the masses of atoms consisting of superconductor will also affect the superconducting properties, which is known as isotope effect. Other external forces like pressure can influence ω_D by changing crystalline lattice paramters.

Another physical properties often taken as in indicator of the strength of superconductivity is the superconducting energy gap at zero temperature,

$$\frac{2\Delta}{k_B T_c} = 3.52. \tag{2.2}$$

When the gap is completely closed, that is $\Delta = 0$, superconductivity disappears and normal metallic state is resumed.

2.2 $YBa_2Cu_3O_{7-\delta}$ Background Introduction

The first superconductor mercury was found at 4.2 K on April 8, 1911 in Leiden by Heike Kamerlingh Onnes after he successfully liquefied helium [25]. Then the gate to a new world has opened to physicists. Since then, more than a hundred years has been spent on trying to find out as much as possible superconductors in nature and are even synthesising new materials with superconductivity. This passion is driven not only by the interest in physics itself, but also by superconductivity's great potential in industrial applications. To systematically study the properties of superconductivity, theorists in 1957 as stated in the last section developed the BCS theory to describe it, which later was proved experimentally in many type I superconductors [23]. Based on this theory, almost all the properties of type-I superconductors can be quantitatively predicted and explained. However, BCS theory also predicted that no superconducting transition can go above 30 K, which was taken as a firmly agreed prediction at that time. Until in 1986, $La_{2-x}Ba_xCuO_4$ [12], the first member of the copper-oxide high-temperature superconductor family was discovered by Bednorz and

M*ü*ller, with a superconducting transition temperature of 35 K. The transition temperature of this material was later improved to 40 K quickly by applying high pressure. Materials in this family were soon found showing even higher transition temperatures up to 135 K[26] in the following years with chemical doping and pressurisation being used extensively. The great energy and funding devoted to the research related to copper-oxide high-temperature superconductor unprecedentedly deepened our understanding of the superconductivity, or broadly speaking, the field of strong-correlated materials.

In the study of high-temperature superconductors, the purity is an important factor which limits the physical properties detected in experiment. However, due to the instability of layered structure of copper-oxide high-temperature superconductor, the synthesis of single crystals with high quality became the first problem. After decades having been dedicated and a large family of copper-oxide superconductors can be obtained now. Among them, $YBa_2Cu_3O_{7-\delta}$ is the purest material. Physicists have developed a process to obtain chemically and structurally high-purity $YBa_2Cu_3O_{7-\delta}$ single crystals [14, 27, 28], which makes it perfect for studying superconductivity.

The $YBa_2Cu_3O_{7-\delta}$ high-temperature superconductor family [29] was firstly synthesised in 1987 following the first copper-oxide high-temperature superconductor discovered in 1986. As the first superconductor with the transition temperature above 77 K, the boiling point of liquid nitrogen, $YBa_2Cu_3O_{7-\delta}$ has been attracting numerous research labs working on the physical principles behind its superconducting phenomenon for decades.

$YBa_2Cu_3O_{7-\delta}$ shares a similar tetragonal or orthohrombic structure with other copper-oxide high-temperature superconductors, depending on the oxygen doping level. By carefully studying the transport properties with respect to temperature and magnetic field, a nearly complete phase diagram is drawn for $YBa_2Cu_3O_{7-\delta}$ from underdoped to overdoped as shown in Fig. 2.1.

Physicists tried to chemically dope $YBa_2Cu_3O_{7-\delta}$ by replacing Y, Ba, Cu, or O with other elements, which all show changes of the superconducting transition temperature to some extent, which is actually caused by changing the hole concentration or electron concentration of $YBa_2Cu_3O_{7-\delta}$. Fig. 2.1 is a schematic diagram of the superconducting transition temperature as a function of the doping level denoted by the amount of holes per copper atom. Most of the studies are focused on hole doping as with this tuning the highest superconducting transition temperature can be obtained.

Depleting the oxygen out of $YBa_2Cu_3O_7$, that is tuning the value of δ in $YBa_2Cu_3O_{7-\delta}$, is one of the common ways of tuning its superconducting transition temperature. With $\delta = 1$, the corresponding hole doping level p is 0.194, giving a superconducting transition temperature $T_c = 85.3$ K. Reducing δ, the superconducting transition temperature will firstly

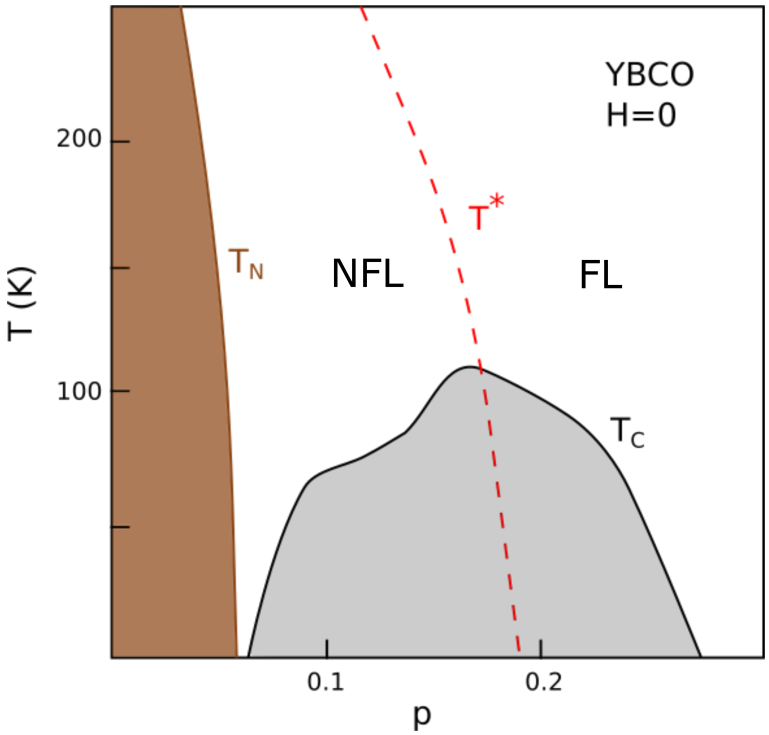

Fig. 2.1 Schematic of the $YBa_2Cu_3O_{7-\delta}$ phase diagram with zero magnetic field applied. The horizontal axis is the hole concentration p per Cu taken as an indication of the doping level. The vertical axis is the temperature axis. T_N represents the antiferromagnetic transition temperature at low doping level as shown in the brown region. FL is short for Fermi liquid, and NFL is short for non-Fermi liquid. With the hole concentration increasing, $YBa_2Cu_3O_{7-\delta}$ gradually becomes metallic from an insulating state, but with strange metal behaviour under the line of T^*, which characterise the start of so-called pseudogap. In this region, $YBa_2Cu_3O_{7-\delta}$ does not perform like a Fermi liquid and goes into the superconducting state at low temperature. Interestingly, with higher hole doping level the superconducting transition forms a dome with droping transition temperature T_c. For large p's, the strange metallic behaviour disappears.

rise up to 94.3 K with p being close to 0.125, followed by a drop until the superconductivity disappears at around $p = 0.05$. The decrease of the transition temperature on the phase diagram with increasing p is called overdoping. However, individual oxygen depletion cannot tune the superconducting transition temperature into the overdoped region, so cation substitution needs to be employed [30]. These two chemical replacements appear to be similar, but they actually differ greatly in tuning the physical properties of high-temperature superconductors. More oxygen-vacancy disorder will be introduced simultaneously in oxygen depletion, but not in cation substitution [16, 20]. The prominent cation substitution is to partially replace Y^{3+} by Ca^{2+} to increase hole carrier concentration. For fully-oxygenated $YBa_2Cu_3O_{7-\delta}$ case, Ca doping will reduce the superconducting transition temperature from its maximum. Unfortunately, the empirical relation between T_c and the hole concentration per Cu does not fit into Ca-doped $YBa_2Cu_3O_{7-\delta}$. This is believed to come from the accompanying disorders, because the reduced superconducting transition cannot be restored to its optimal value [31].

To tune pristine $YBa_2Cu_3O_{7-\delta}$ into the overdoped region, hydrostatic pressure is another option. Pressure is appliyed mechanically on the superconductor to change its density of states at the Fermi surface, phonon frequency, and the strength of the interaction between phonons and electrons which will in turn influence the superconductivity. For most type-I superconductors superconducting transition temperature will drop with the increase of external pressure (different from type-II superconductors). This is attributed to the decrease of the density of states around the Fermi surface and the interaction of phonons and electrons. At the early development of this technique, uni-axial pressure was applied mostly, owing to its simplicity and convenience in experiments. Uni-axial pressure is applied via solid media in a single direction. Generally, the uni-axial pressure affects along the three lattice axes differently [32–34]. A prominent case on $YBa_2Cu_3O_7$ [34] revealed that the superconducting transition temperatures dropped when the uni-axial pressure was applied along a-axis or c-axis while rised when the uni-axial pressure was applied along b-axis. This phenomina was explained by that the number of charge carriers in the CuO_2 planes is increased by pressure along a- and c-axis how the contrary is ture when pressure is applied along b-axis.

Recently, physicists have improved the high-pressure technique by taking advantage of liquid pressure media, such as silicone oil. Proper liquid can create hydrostatic pressure environment for the samples inside. Thus when pressure is applied, the force comes from all directions to isotropically squeeze the sample. A superconductor under hydrostatic pressure usually has a higher superconducting transition temperature, which greatly enlarges the experimental range in searching for new exotic high-temperature superconductors. To obtain a high enough hydrostatic pressure, essential elements like diamond anvils with good quality

and small tips, a sample space small enough, and a reliable pressure media are critical. However, due to the hardness of diamond, the smaller the tip is, the more likely it will crack with a tiny misalignment. Besides, a small sample space normally means that the sample will be small, too. If electric resistance is to be measured, some extra space is also necessary for conducting wires. As for pressure media, there are no media that can meet the requirement of hydrostatic pressure in a wide pressure range. The highest hydrostatic pressure recorded is 90 GPa, realised in pressing H_2S into the superconducting state [35]. Even with all these difficulties, physicists are still dedicated to working on this technique, because hydrostatic pressure is a clean technique, which does introduce extra chemical disorder into materials. Unlike the Ca doped $YBa_2Cu_3O_{7-\delta}$ mentioned above, hydrostatic pressure only modifies the internal interaction bewteen phonons and electrons, which makes it easier to build a theoretical model to describe high-temperature superconductivity and to verify a model's predictions.

To suppress the superconductivity of $YBa_2Cu_3O_{7-\delta}$, a hydrostatic pressure as high as up to 90 GPa is required. Until now no experimental results have been reported to fully suppress it. In this thesis, we are trying to go over the dome into the overdoped region of the phase diagram by applying hydrostatic pressure to $YBa_2Cu_3O_{7-\delta}$ and measuring its AC magnetic susceptbility. To reach a high enough pressure to reduce T_c, the sample space has to be made very small, which will lead to a difficulty in making electrical contacts to tiny samples. Therefore, the AC magnetic susceptibility measurement was chosen instead as a contactless technique.

AC magnetic susceptibility measurements have been widely used in condensed matter physics research starting from the study of magnetism of materials, such as spin glasses, superparamagnets. The basic method is to measure the AC response from the sample while externally an alternating magnetic field is applied. The normal setup of the experiment includes two coils with one as pick-up coil for the sample enclosed and the other as driving coil placed coaxially to generate a AC magnetic field as stimulus. A lock-in amplifier is generally employed as signal generator and collector. Due to the alternation of the external magnetic field, dynamic magnetization is actually obtained, in contrast with the static magnetization from DC magnetic susceptibility measurements. Usually the applied AC magnetic field is very small and will not disturbe the measured material into other states. Therefore, if at this moment a much larger DC magnetic field is applied to tune material into other phases, it will be able to map the phase diagram of the materials' magnetic dynamics as a function of magnetic field. A typical magnetic dynamic response is shown in Fig. 2.2 [1].

Superconductors can be classified into type-I and type-II by the formation of magnetic vortices (a structuring consisting of a normal core and surrounding superconducting current)

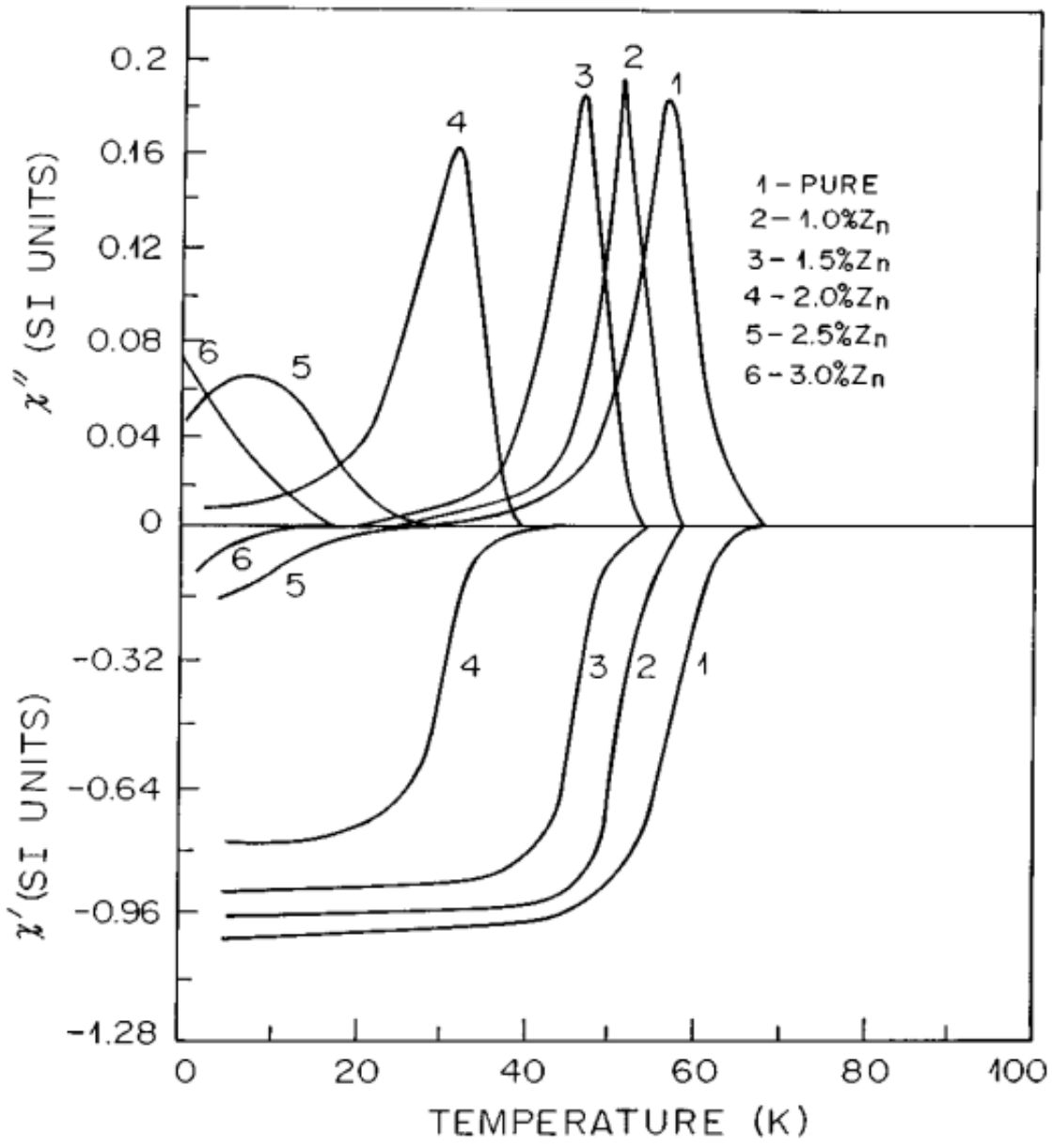

Fig. 2.2 AC magnetic susceptibility of high-temperature superconductor $LaBaCaCu_3O_{7-\delta}$ for a series of Zn concentrations as a function of temperature. χ' and χ" are the real and imaginary part of AC magnetic susceptibility, respectively. Adapted from [1]. Copyright 2019 by American Physical Society

in external magneti field. In type-II superconductor, a large amount of research has focused on the study of vortex melting after materials have become superconducting, getting close to the upper critical field H_{c2} [3, 36]. The upper critical field is a prominent feature in a type-II superconductor differentiating it from conventional type-I superconductor. It is characterised by the Ginzburg-Landau parameter $\kappa > 1/\sqrt{2}$ and negative surface energy. Before the magnetic field approaches the upper critical field H_{c2}, the material will not leave the perfect diamagnetic state immediately, but will be in a vortex state formed with normal-state cores and the superconducting current flowing around them. In each core, there is a quantised flux $\Phi = \hbar/e$. The radius of the normal core is given by the superconducting coherence length ξ. Circulating their cores, the supercurrent decays over the London penetration depth λ. In the region close to the lower critical field H_{c1}, a few vortices exist whose movement is dominated by the Coulomb interaction and cannot move. They will form a triangular vortex lattice or so-called Abrikosov lattice, firstly predicted by Russian physicist A. A. Abrikosov, which was later observed by experiments.

Due to the loss of energy in the transition from vortex liquid to vortex lattice, AC magnetic susceptibility measurement, with the imaginary part χ" representing energy loss, is a good method to looking for the melting transition of vortex lattice. Looking back at Fig. 2.2, the peak of the imaginary part of magnetic susceptibility χ" is defined as the vortex lattice melting point with the greatest energy loss.

The aim of this project is to verify that AC magnetic susceptibility measurement can be applied to obtain information about highly pressurised $YBa_2Cu_3O_{7-\delta}$ in a diamond anvil cell. The experimental results on chemically overdoped $YBa_2Cu_3O_{7-\delta}$ had been obtained in the past. But they were not pure $YBa_2Cu_3O_{7-\delta}$ single crystal, so we planned to tune pure $YBa_2Cu_3O_{7-\delta}$ single crystal into its overdoped region by high-pressure and to measure its physical properties under this extreme conditions followed by comparison with existing results from chemically doped $YBa_2Cu_3O_{7-\delta}$ to verify the effectiveness of our technique.

2.3 Crystal Structure

In solid-state physics, the periodic crystal structure of a material completely determines its chemical and physical properties, because the positions of the atoms shape the way the electrons inside interact with one another, the so-called electronic structure.

The crystal structure of the copper-oxide high-temperature superconductor family belongs to the oxygen-deficient Ruddlesden-Popper structure, which is closely related to the perovskite structure and buffer rock salt by stacking one over another. The general formula for copper-oxide compounds is $(Ln_{1-x}M_x)_{n+1}Cu_nO_{3n+1-m}$, where Ln is a rare-earth element

or yttrium (Y), and M is a divalent alkaline element. As is shown in Fig. 2.3, $YBa_2Cu_3O_{7-\delta}$, a typical copper-oxide high-temperature superconductor, has CuO_2 sublattice layer and buffer layer BaO layer alternating. Thus it is also called the layered perovskite structure.

In the crystal structure of $YBa_2Cu_3O_{7-\delta}$, the CuO_2 is mainly responsible for the conducting electrons in electronic transport. This is very critical to the superconductivity in copper-oxide high-temperature superconductors. In the chemical doping method that we will talk about in a later section, the holes-created oxygen deficiency will be introduced into these layers and eventually affect the superconducting transition temperature. It is also found that with more CuO_2 layers, a higher superconducting transition temperature can be achieved. A prominent example is $HgBa_2Ca_{n-1}Cu_nO_{2n+2+\delta}$ ($n = 1 \sim 6$). In the $n = 3$ case, the superconducting transition temperature can reach as high as 138 K [37]. However, the material also becomes more unstable, which makes it very difficult to synthesise. The other BaO layers work to provide enouge electrons for the CuO_2 layers, which are called the charge reservoir. Chemical doping cannot easily change the oxygen concentration in the charge reservoir.

2.4 Electronic Band Structure

A solid material's electronic structure reveals how its electrons move and distribute within the material, which can explain many physical properties of solid. Thus, before looking into the general physical properties of copper-oxide high-temperature superconductors, it is necessary to understand their electronic structure.

With a small change in crystal structure a drastic difference may occur. The most common example would be the Peierls metal-insulator transition taught in almost every solid-state textbook [38]. In brief, the Peierls transition as shown in Fig. 2.4 describes a phenomenon in which the deformation of the lattice of a one-dimensional metal will create an energy gap, thereby lowering the total energy of the electrons. The saved electronic energy needs to be larger than the increase of elastic and kinectic energy. Therefore, it is meaningful to learn more about crystal structure of materials before looking into other properties.

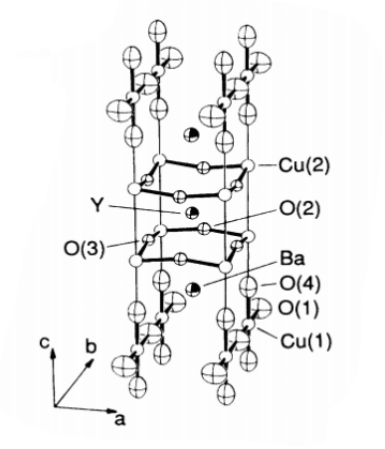

(a) Orthorhombic structure

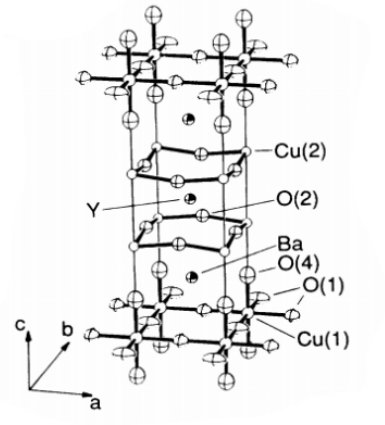

(b) Tetragonal structure

Fig. 2.3 Crystal structures of $YBa_2Cu_3O_{7-\delta}$ in the (a) *Pmmm* orthorhombic and (b) $P4/mmm$ tetragonal phases. CuO_2 layers as charge conduction layers are sandwiched between yttrium atoms and BaO layers as charge reservoir layers. Pictures adapted from [2]. Copyright 2019 by American Physical Society

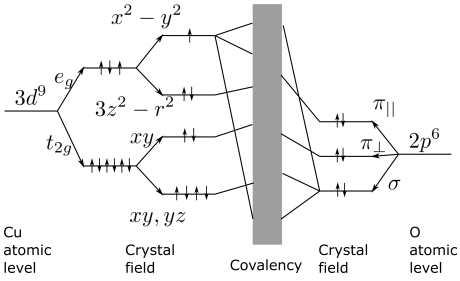

Fig. 2.5 Electronic structure of Cu atom and O atom on the CuO_2 plan in the crystal field of copper-oxide high-temperature superconductor together with their covalent bonds considered. The $3d$ band of Cu is firstly split into two subbands, then furthur into four subbands. For $2p$ band of O, the final split gives three subbands. The subbands from Cu and O then hybridise together forming covalent bonds.

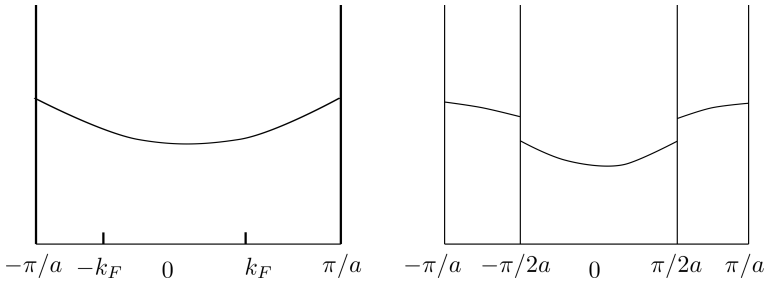

Fig. 2.4 Energy band diagram of the Peierls transiton. The parabolic curve continuous at the wave vector k_F is the energy dispersion spectrum before crystal structure deformation, while it breaks into two sections to lower the electronic energy of the system after crystal structure deformation.

A copper atom Cu on the CuO_2 planes is actually located in a CuO_6 octahedron. In a crystal field of cubic symmetry, its $3d$ electronic energy band will be split into two subbands, a doublet $e_g = \{d(x^2-y^2), d(3z^2-r^2)\}$ and a triplet $t_{2g} = \{d(xy), d(yz), d(xz)\}$. If a crystal field of tetragonal symmetry is apllied after that, the doublet will be further split into two singlets $b_{1g}\{d(x^2-y^2)\}$, $a_{1g}\{(3z^2-r^2)\}$ and the triplet into a singlet $b_{2g}\{d(xy)\}$ and a doublet $\{d(xz), d(yz)\}$. The degeneracy of the $2p$ energy band of the oxygen atom will be split into three singlets $(p\pi_{||})$, $(p\pi_\perp)$, and $(p\sigma)$.

Experimentally, the initial parent copper-oxide is a Mott insulator. However, with holes or impurities doped into it, a metal followed by superconductor appears. In the Mott-Hubbard model, this is explained by a large charge transfer gap that separates the conduction band into an upper Hubbard band (UHB) and a lower Hubbard band (LHB) caused by a large Coulomb correlation energy. Doping holes into the CuO_2 plane can gradually change the dominant interaction and generate a narrow band around the Fermi level, which makes it possible to conduct.

2.5 Transport Properties

Copper-oxide high-temperatrure superconductors behave differently in their normal states from normal metals. Linear resistivity as a function of temperature is the most prominent property. In Fermi-liquid theory, metals have a resistivity quadratic as temperature decreasing until a plateau is reached persisting down to zero temperature. This is called residual resistivity with a source of impurities in the material. In angle-resolved photoemission spectroscopy (ARPES) [39] and scanning tunneling microscope (STM) [40], an energy gap (pseudo gap) was clearly observed to open on the Fermi surface even far away above the superconducting transition temperature T_c, which is proposed to be the precursor of superconductivity. Other transport properties also revealed a similar phenomenon [41]. Much effort [42, 43] has been expended on the pseudo gap as people believe this is the critical point to understand the copper-oxide high-temperature superconductor.

2.6 Theoretical Models of Copper-Oxide High-Temperature Superconductors

From the anomalous behaviour obtained experimentally so far as shown in the previous sections, the BCS theory for conventional superconductors cannot apply to the copper-oxide high-temperature superconductor which is based on the picture of a Fermi-liquid. To explain both the normal state and the superconducting state of the copper-oxide high-temperature superconductor, several models have been devised since the discovery of the first high-temperature superconductor [44–47].

The Hubbard model [45] is considered to be the simplest model capturing the essence of a copper-oxide high-temperature superconductor. It has two terms in its Hamiltonian describing the kinetic energy and the potential energy between on-site interaction of two neighbouring Cu atoms. This model was firstly proposed in 1963 with a purpose of explaining

the interaction bewteen transition metal oxides. Later it was generalised to describe the behaviour of copper-oxide high-temperature superconductors in the 1980s and of ultracold atoms trapped in optical lattices [48] in the 1990s.

The Hubbard model is an improvement from the tight-binding model taking into account the strong Coulomb interaction between electrons and it can successfully explain the Mott insulator, thus it is also called the Mott-Hubbard model.

Physicists have been debating whether the electron-phonon interaction is the glue forming the superconductivity in copper-oxide high-temperature superconductors as the conventional superconductor is well described by BCS theory. Some propose that it is the spin fluctuation that is truly taking effect other than electron-phonon interaction [49, 50]. The main idea is that the antiferromagnetic spin fluctuations can mediate superconductivity of single pairing with d-wave character [51, 52]. This theory has a popular grounding in the research on unconventional superconductors, like heavy fermion superconductors, which predicts non-Fermi-liquid behaviour in their normal states as observed in experiments. However, there is no determitive experimental evidence up to the present.

2.7 Applications

The high-temperature superconductors have numerous important applications in academia and industry. The most well-known in the lab may be the superconducting magnet which can generate an extremely high static magnetic field. The strongest nondestructive magnetic field was realised in 2012 in the National High Magnetic Field Laboratory in Tallahassee, which provides a convenient facility for scientists from various fields to study the behaviour of objects under extreme conditions. In addition, several other applications are also remarkable.

In medicine field, high-temperature superconductor is used for generating a strong magnetic field for magnetic resonance imaging (MRI) technique in radiology to scan through the organs in the body for medical diagnosis. MRI has been commonly seen in almost every large hospital all over the world and has brought more precise diagnosis and less radiation than CT scan.

The property of lossless energy transmission of superconductor because of its zero resistivity is possibly the most attractive aspect to industry. American Superconductor Corporation (AMSC) utilise high-temperature superconductor wire in place of traditional alminium or copper conductors. The cables can transmit 10 times more power than conventional cables. In both AC and DC cases, superconductors help to improve the resillent electric grid (REG) systems' reliability against harsh weather situation. However, due to large amount of liquid nitrogen required for cooling, it has not been applied in large area.

Electrodynamic suspension (EDS) is one type of magentic levitation technology that is adopting superconducting magnets to create a static magnetic field to pulse and pull the trains along the guide track. Without losing energy from the friction from the touching of two interfaces, the train can travel as fast as 603 km/h, even with a heavy load [53].

Superconducting quantum computing devices are another exciting application of superconductors. Superconductors are employed to form qubits which are the basic units of processor for realsing quantum computation. Google, Microsoft, IBM and Intel have been participating the related research and are trying to commercialise this technique.

More proposed applications of superconductors, especially the high-temperature superconductors, are on their way to appearing in the world, which makes it important to fully understand the mechanism of high-temperature superconductivity. If T_c could be raised closer to room temperature, then these applications would be far more widespread, and a theoretical understanding may help us to design new type of high-temperature superconductor, such as by incorporating strain into the lattice.

2.8 Introduction to Vortex Physics

In 1950 V. L. Ginzburg and L. D. Landau developed their model from the Landau theory of phase transitions by expanding the Gibbs energy around the critical field with respect to the square of the order parameter Φ. Φ is defined as the wave function of superconducting electrons. The square of it is the superconducting electron density, which is an important indicator of the state of superconductivity. In 1957, A. A. Abrikosov[54] solved the GL equation approximately near the critical field and developed the concepts of vortex line and vortex lattice, which greatly enrich the GL theory. Abrikosov introduced a concept referring to "interface energy" κ for describing the interfacial energy between normal region and superconducting region, or the ratio of the London penetration depth to coherence length. A remarkable finding was that $\kappa = 1/\sqrt{2}$ is a threshhold that divides superconductors into two categories, one of which is called type-I superconductor with positive surface energy, while the other is a type-II superconductor with negative surface energy. $YBa_2Cu_3O_{7-\delta}$, studied here, is a strongly type-II superconductor with vortices present over a large region of the phase diagram.

The phase diagram of a type-I superconductor consists of a Meissner phase with magnetic flux completely repelled at low magnetic field $H < H_c$ and a normal phase without expelling flux at high magnetic field $H > H_c$. In type-II superconductors the lower critical field H_{c1} having similar property as that of type-I, while above it is a mixed state with magnetic field penetrating in the form of vortices. The vortices form a triangular vortex lattice, which can

be derived from Abrikosov's theory[54] and has been proved experimentally [55–57]. With increasing field, the vortices overlap with one another and the superconductor resumes its normal state at upper critical field H_{c2} and above. There are mainly three dominant factors affecting the behaviour of vortices in type-II superconductors, i.e. quenched disorder, thermal fluctuations, and quantum fluctuations. In the mixed phase, the vortices will start to move under the condition that the external current density j applied to the system is larger than a specific value called the critical current density j_c. This movement will cause the system to dissipate energy. Quenched disorder, however, is able to pin the vortices and keep the system dissipationless. In strongly type superconductor like $YBa_2Cu_3O_{7-\delta}$, thermal fluctuations are another crucial force that cannot be ignored due to the extremely high superconducting transition temperature compared with conventional type-I superconductor. Large thermal fluctuations influences the dynamic properties of vortices in type-II superconductors by introducing a phase transition from vortex lattice to vortex liquid. This transition is also known as thermal depinning transforming two vortex states continuously. The strength of thermal fluctuations can be quantified by Ginzburg number G_i measuring the condensation energy within a coherence volume at $T = 0$ relative to that at the superconducting transition temperature T_c. Thus, the increase of Ginzburg number reflects an enlargement of the critical fluctuation region of the $H - T$ phase diagram. The third factor, quantum fluctuation, can affect superconductivity via the quantum motion of vortices (called quantum creep). Due to the reason that both thermal fluctuation and magnetic field close to H_{c1} can melt the vortex lattice to a vortex liquid, in the intermediate field range, $H_{c1} \ll H \ll H_{c2}$, there exist two melting lines on the $H - T$ phase diagram (reentrance). Here we are mainly studying how the second factor, thermal fluctuation, works in $YBa_2Cu_3O_{7-\delta}$ at fields close to the upper critical field H_{c2}.

The layered structure of a high-temperature superconductor is another source of interesting behaviours. We denote a mass anisotropy ratio by $\varepsilon^2 = m/M < 1$. Superconductors with large ε can be taken as quasi-two-dimensional materials in GL theory giving rise to 2D pancake vortices interconnected by the Josephson effect between two adjacent superconducting layers. However, $YBa_2Cu_3O_{7-\delta}$ is technically treated as a 3D superconductor in the copper-oxide superconductor family in GL theory though strictly it is also with layered structure. In a type-II superconductor we define a thermodynamic critical field H_C having the form

$$H_C = \frac{\Phi_0}{2\sqrt{2}\pi\Lambda\xi}, \tag{2.3}$$

where $\Phi_0 = h/2e$ is the quantum flux, Λ is the GL penetration depth, and ξ is the GL coherence length. This physical quantity cannot be directly measured experimentally, nevertheless,

it has a physical meaning for type-II superconductors, which is derived from the Gibbs energy difference of normal and superconducting states.

To estimate the melting transition caused by thermal fluctuation in the $H-T$ phase diagram, the Lindemann criterion

$$< u^2(T_m) >_{th} \approx c_L^2 a_0^2, \tag{2.4}$$

with Lindemann number $c_L \sim 0.1-0.2$ is often used. This criterion comes from the assumption that vortex lines become unstable with respect to thermal fluctuation when the mean-squared amplitude of fluctuations ($< u^2 >_{\text{th}}$) goes beyond a certain value. Then a melting temperature can be obtained:

$$T_m(B) \approx 2\sqrt{\pi}\varepsilon_0 c_L^2 \left(\frac{\Phi_0}{B}\right)^{1/2} \tag{2.5}$$

$$\approx \left(\frac{\beta_m}{Gi}\right)^{1/2} c_L^2 \left(\frac{H_{C2}}{B}\right)^{1/2} T_c, \tag{2.6}$$

with $\beta^2 \approx \pi^2$. With the choice of $\beta = \pi^2$, inversion of Eq. 2.6 will define a melting line in the $H-T$ phase diagram as

$$B_m(T) \approx \beta_m \frac{c_L^4}{Gi} H_{C2}(0)(1-\frac{T}{T_C})^{1/2}, \tag{2.7}$$

where $H_{c2}(0)$ is the extrapolated upper critical field at zero temperature. This Eq. 2.7 can be simplified into

$$\frac{\sqrt{b_m(t)}}{1-b_m(t)} \frac{t}{\sqrt{1-t}} \left[\frac{4(\sqrt{2}-1)}{\sqrt{1-b_m(t)}} - 1\right] = \frac{2\pi c_L^2}{\sqrt{Gi}}, \tag{2.8}$$

in which the reduced magnetic field $b_m = B_m/\mu_0 H_{c2}$ and the reduced temperature $t = T/T_c$ are used. The explicit form of Ginzburg number Gi is

$$Gi = \frac{1}{2}\left[\frac{T_c}{H_c^2(0)\xi^3(0)}\right]^2, \tag{2.9}$$

where the thermodynamic field $H_c(0)$ is obtained from the relation $H_c(0) = H_{c2}(0)/\sqrt{2}\kappa$. Gi can determine the width of the fluctuation in the region close to the upper critical field H_{c2}.

2.9 High-Pressure Physics

2.9.1 Theory and Related Discussion

High-pressure studies of materials plays an important role in the development of solid-state physics, especially for the studies of the normal state and the superconducting state in a superconductor. The idea is to use physical force to adjust the lattice parameters of a crystal's structure, thereby changing the electronic structure of the material. The transition temperature is usually also pressure dependent.

The phenomenon of decreasing transition temperature T_c with externally applied pressure P has been observed long time ago in conventional superconductors. This can be explained easily by classical BCS theory. As presented in the previous section, BCS theory demonstrates that the superconducting transition temperature T_c can be written as

$$kT_c \simeq \hbar\omega \exp(-1/\xi). \tag{2.10}$$

If equation 2.10 is differentiated with respect to the pressure P. The relation

$$\frac{d\ln T_c}{dP} = \frac{\partial \ln \omega}{\partial P} + \frac{1}{\xi}\frac{\partial \ln \xi}{\partial P} \simeq \frac{\partial \ln \omega}{\partial P} + \frac{1}{\xi}\left(\frac{\partial \ln \eta}{\partial P} - 2\frac{\partial \ln \omega}{\partial P}\right), \tag{2.11}$$

is obtained, where the interaction parameters $\xi = \eta/M\omega^2$ and $\eta = N(0)\gamma^2$. For most conventional superconductors, experimentally it has been observed that the superconducting transition temperature T_c decreases with pressure P. Because of the high electronic density of metals, both the density of states $N(0)$ and the electron-phonon interaction γ are weakly dependent on the mechanical pressure applied externally. Thus the second term on the right-hand side of Equation 2.11 dominates the influence of pressure on T_c. The corresponding $dT_c/dP < 0$ is due to the decreased lattice stiffness with the applied pressure [58–60]. With some d-band metals, their energy band structure makes it possible to have a pressure-dependent density of states $N(0)$ leading to a positive dT_c/dP.

However, for the case of the copper-oxide high-temperature superconductor, the dependence of T_c on the density of charge carriers needs to be considered. To differentiate the two contributions from the intrinsic part of the pair interaction and the charge transfer p part from pressure, we calculate that

$$\frac{dT_c}{dP} = \left(\frac{\partial T_c}{\partial P}\right)_{\text{intrinsic}} + \left(\frac{\partial T_c}{\partial p}\frac{\partial p}{\partial P}\right), \tag{2.12}$$

in which p represents the carrier concentration in the CuO_2 planes. This is called the modified charge-transfer model. The intrinsic contribution comes from the reduction of the lattice parameters if factors like the structure transition, oxygen ordering effect, and carrier concentration are kept constant.

Experimentally it has been found that the superconducting transition temperature T_c is dependent on hole carrier concentration p per Cu atom on the CuO_2 plane, with a relationship [28, 61]

$$T_c(p) = T_c^{\max}[1 - \beta(p - p_{\text{opt}})^2] \tag{2.13}$$

where $\beta \simeq 82.6$ and $p_{\text{opt}} \simeq 0.16$ for $La_{2-x}Sr_xCuO_4$ where x represents the concentration of Sr [28], as illustrated in Fig. 2.6.

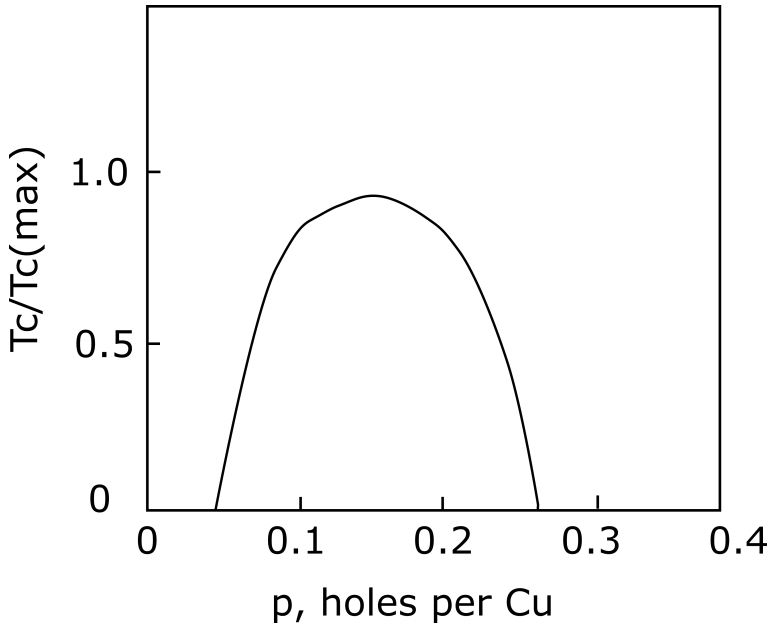

Fig. 2.6 Schematic phase diagram of $La_{2-x}Sr_xCuO_4$ showing a parabolic superconducting domain with respect to the hole concentration p per Cu on the CuO_2 plane.

$La_{2-x}Sr_xCuO_4$ is one of the two copper-oxide high-temperature superconductors first discovered in 1986. It was also fully characterised by scientists, including the empirical relationship between the doped hole concentration per Cu on a CuO_2 plane and the stoichiometric oxygen vacancy as shown in Eq. 2.13. This relationship is reasonably correct for $YBa_2Cu_3O_{7-\delta}$, except for the region around $p = 1/8$ ($x = 0.67$) which was later characterised in more detail by Liang et al. [14] in 2006 as illustrated in Fig. 2.1. At this doping region, T_c is suppressed by the tendency of charge strip formation, thus does not follow Eq. 2.13. The overdoped region of $YBa_2Cu_3O_{7-\delta}$ that we will discuss in the following section is basically matching the $La_{2-x}Sr_xCuO_4$ relationship in Eq. 2.13.

From Fig. 2.6, it can be seen that T_c initially increases with p on the underdoped side to a maximum transition temperature $T_c^{\max}$ at optimal doping $p = p_{\text{opt}}$, then decreases with p on the overdoped side. Obviously, $dT_c/dp > 0$ on the underdoped side and $dT_c/dp < 0$ on the overdoped side.

Thus at the optimal doping level, the pressure-dependent superconducting transition temperature T_c also reaches its optimal value. For underdoped and overdoped copper-oxide high-temperature superconductors, under pressure T_c exhibits the opposite behaviour, that is

$$\left(\frac{dT_c}{dP}\right)_{\text{underdoped}} > 0, \tag{2.14}$$

$$\left(\frac{dT_c}{dP}\right)_{\text{overdoped}} < 0. \tag{2.15}$$

The relations shown above can only roughly describe the superconducting transition temperature T_c behaviour as a function of hole carrier concentration per Cu. As we can imagine, a material with crystal structure as complex as a high-temperature superconductors' distorted quasi-two-dimensional perovskite structure (which will be introduced in the next section) will certainly be more complicated. Moreover, in actual high-pressure experiments more effects will occur and such considerations have to be to taken into account.

2.9.2 High Pressure Technology

The study of high-pressure phenomena dates back to Boyle's law of compressing a gas in thermodynamics. Later high pressure was used to realise the liquefaction of gas to observe the phase transition between gas and liquid. In the beginning of the 20th century (1906), P. W. Bridgemann, who is considered who has been the father of modern high-pressure research, invented the widely used Bridgemann pressure cell and put it into practice, completing a series of high-pressure studes. We can also say that the diamond-anvil cell which can create an even higher pressure could not have been born without the pioneer Bridgemann.

There are three types of forces that can be applied to materials, as shown in Fig. 2.7. The first is tension expanding material along a single axis. The second is compression applied along a single direction, called uniaxial pressure. The third is to compress the material from all directions, called hydrostatic pressure.

Uniaxial pressure is firstly put into actual high-pressure research because it is convenient to realise and can achieve extremely high pressures. Through applying uniaxial pressure along a particular axis, we can easily separate the physical properties affected by this axis with others, which provides advantages for designing comparative experiments. However, some

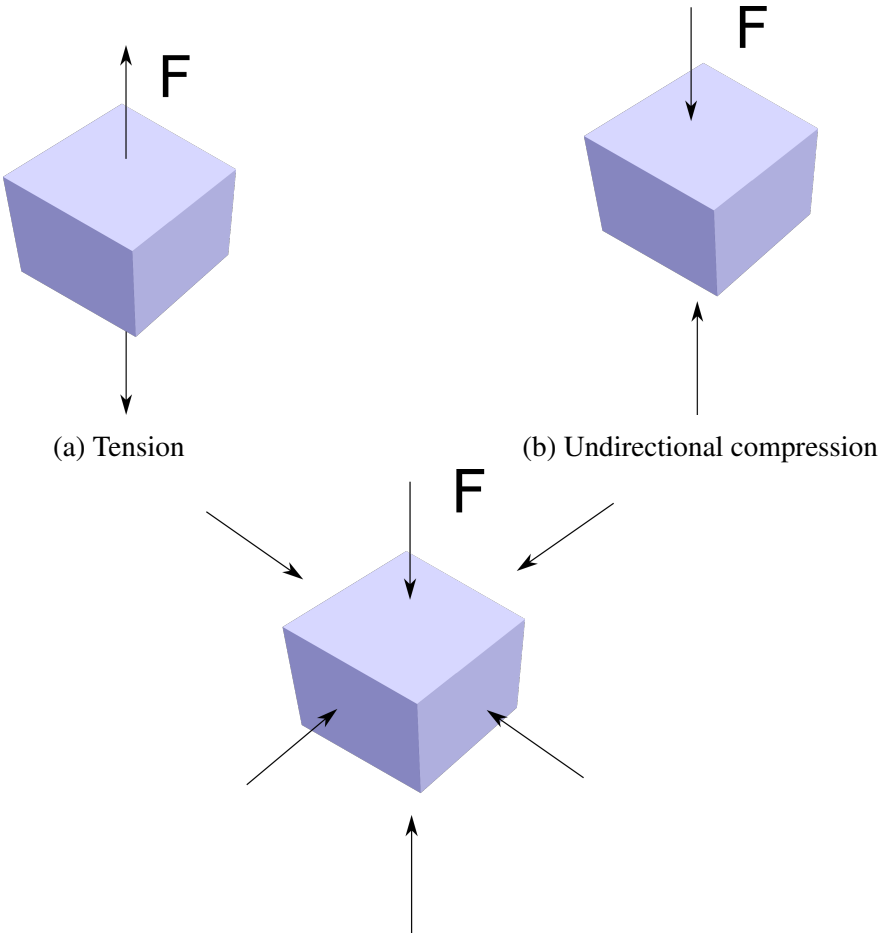

(a) Tension

(b) Undirectional compression

(c) Hydrostatic compression

Fig. 2.7 Three types of pressure applied to a material. (a) Tension to expand the crystal structure,(b) Unidirectional compression created by a solid pressure medium, (c) Hydrostatic compression created by liquid or gaseous pressure media. F represents the force applied.

disadvantages accompanying it occur together. A prominent one is the corresponding change in other directions during the pressurisation. The experimental results may be contaminated by uncontrolled parameters, such as the change of other lattice parameterss. Thus more and more groups have turned to the hydrostatic pressure technique.

Hydrostatic pressure is the pressure that is exerted by a liquid or gas (pressure media) at equilibrium at a given pressure within the liquid or gas. The object bearing the pressure normally stays inside the pressure medium, which can only be realised in a liquid or gas.

In principle, the transmission of pressure has to have low shear strength. For solid pressure media, they need to be stable enough not to undergo a structural phase transition with applied uniaxial pressure. For hydrostatic pressure, the pressure-transmitting medium has to be a compressible fluid that can fill the sample space and is able to transmit the applied pressure. Hydrostatic pressure is more popular among high-pressure experiments because fluid can remain in a good compressible state up to very high pressure. The commonly used pressure fluid includes silicone oil, 4:1 methanol/ethanol, and He and N_2 gases [62]. They are conveniently available in the laboratory and are easy to load into a pressure apparatus. However, it should be noted that each pressure medium has its own suitable pressure range, beyond which it will no longer be hydrostatically compressible.

Three types of pressure cell are used for solid-state physics research. One is the Bridgemann anvil pressure cell, and the other is the diamond anvil pressure cell. The last one is the piston-cylinder pressure cell. These pressure cells share a similar design as illustrated in Fig. 2.8.

The piston-cylinder was initially widely used in Earth sciences for experimentally simulating the Earth's core with extremely high temperature (up to 1700°C) and pressure (up to 6 GPa) simultaneously. Due to the convenience and simplicity of setting up a piston-cylinder pressure cell, a large number of experiments that do not require extremely high pressures still adopt this technique.

A Bridgemann anvil pressure cell has a longer body ($\sim$ 10-15 cm) with a larger sample chamber compared with a diamond anvil pressure cell. Most transport measurements can be conducted inside with enough space for sample, wires, and pressure gauge. The diamond anvil pressure cell was developed based on the Bridgemann anvil pressure cell in 1958 at the National Bureau of Standards (NBS) by Charles E. Weir, Ellis R. Lippincott, and Elmer N. Bunting. It was designed to achieve the highest pressure without destroying the anvils. The material that is used for making anvils is diamond. After decades of successive effort put into improving the anvil design, the attainable hydrostatic pressure extends to as high as 640 GPa [63].

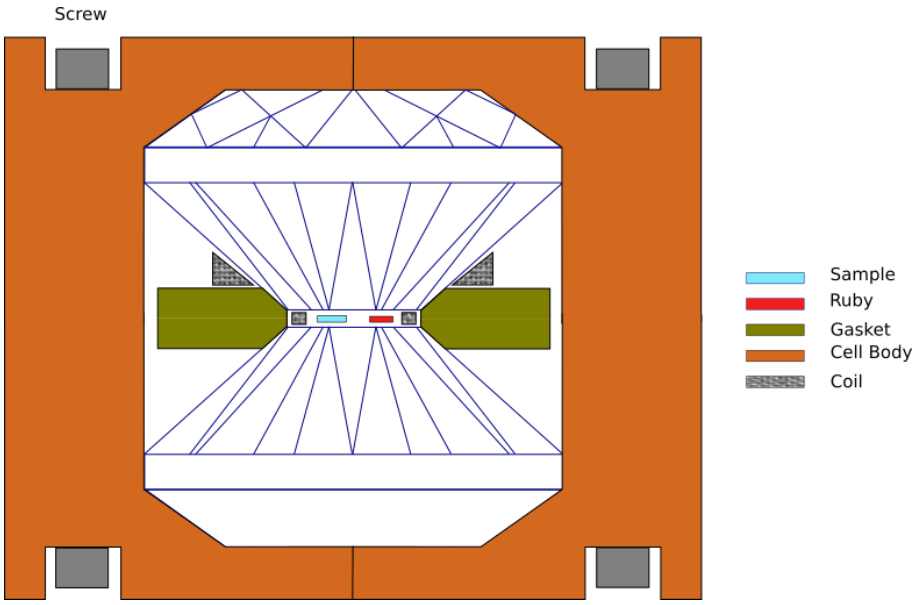

Fig. 2.8 Schematic structural diagram of diamond-anvil pressure cell widely adopted now. The Bridgemann anvil pressure cell has a longer body, but with a similar inner structure as the diamond-anvil pressure cell.

The question of how to exactly measure the pressure in the sample chamber of a pressure cell comes naturally after samples have been loaded. Generally there are two methods. One is to seal a type of material with known physical properties under pressure together with the sample to be tested. Following it, we can measure either its structural information with X-ray diffraction or its transport properties like resistance, to identify the actual loaded pressure. For example, the metal lead (Pb) is often used for pressure gauges as it can give a shift in superconducting transition temperature under different pressures. However, to measure the pressure X-ray equipment or a low-temperature cryostat are necessary, which greatly reduce the practicability of this method. Then in 1971, the NBS found that the wavelength of ruby fluorescence emissions can be used as an indicator of pressure as its fluorescence line shifts with pressure. A tiny ruby crystal is able to generate a strong signal in a fluorescence spectroscope.

Chapter 3

Superconductor: Experiments

3.1 Sample Preparation and Pressurisation of $YBa_2Cu_3O_{7-\delta}$

A pressure cell is designed to create a high pressure environment for the materials being studied. It mainly comprises of a pressure-cell body, a pair of diamond anvils, and screws as shown in the schematic of Fig. 2.8. In this technique, the small sample space, anvils hard enough to bear extremely high pressures and the pressure medium are the critical factors impacting the success of experiments. The high pressure technique was initially introduced and developed in Earth Science for the study of stimulating the high-pressure state in the core of Earth. Those scientists do not require low temperatures, so their pressure cells can be made considerably large and may even occupy a whole room. Later, this technique was transferred into low-temperature physics research for tuning the crystal structures of materials. However, to meet the requirement for a low-temperature experimental environment, the issues of cooling and keeping the temperature of the pressure cell cannot become problematic. The pressure cells then were sinked further and further until the latest are 6 cm in length and 10 mm in diameter. Besides the size, the hardness of the anvils is also an important factor. The anvil shape is specially designed to withstand a hundred gigapascals pressure. Of course, the only material suitable for this purpose is diamond. The third factor to consider is the pressure medium. To create hydrostatic pressure (the same pressure from all directions) on a sample, the medium needs to be able to keep its ideal-fluid property under high pressure. Each of the pressure media adopted currently in condensed-matter physics has its own scope of application. It is important to select the most appropriate one carefully before starting experiments.

3.2 Cryomagnetic Equipment Setup

3.2.1 Dry Cryomagnetic System for AC Magnetic Susceptibility Measurements

An ICEOxford 1.4 K dry cryomagnetic system was used for AC magnetic-susceptibility measurements of pressurised $YBa_2Cu_3O_{7-\delta}$. The so-called dry cryomagnetic system means that no top-up of liquid helium is needed while the system can generate liquid helium from gaseous helium itself by compressing it. The only consumable is electricity, which is considerably cheaper than liquid helium. Without any other accessories, a standard dry system can reach as low as 1.4 K which already meet many experimental requirements. When integrated with a dilution fridge, millikelvin temperature are also achievable easily. The system used in this thesis is a standard one, utilising a two-stage cold head and high-power compressor to refrigerate high-purity helium to the liquid state in its cooling loop, while the circulation loop for cooling the sample thermally contacts the cold head to achieve liquid-helium temperature and further takes the temperature down to 1.4 K by lowering the helium gas vapour pressure. As Fig. 3.1 shows, the helium in the cooling loop is physically segregated from the circulation loop. As the main cooling power source, high-purity helium (99.99999%) is required for the cooling loop. For most of the time, this loop is very clean and well sealed. To cool a sample down, the probe can be first clamped onto the top of the IVC and then loaded down into the IVC through the valve installed on the neck of the IVC. Without a can for the probe, the sample mounted at the bottom of the probe will be exposed and quickly cooled in the cold helium flow. These loading and unloading precedures will cost a small amount of helium from the circulation system. However, with the open-space design for the sample the temperature control of the probe would be challenging as the temperature and the pressure of the helium flow and thermal disturbance from the heater to helium flow are all the necessary factors demanding careful consideration. This is particularly obvious in the warm-up stage. As for the measurements in this study, the pressure cell body forms a relatively closed space for samples which moderates the abrupt changes from helium flow and heat disturbance.

The standard setup for AC magnetic-susceptibility measurement consists of two coils. One is for generating magnetic field and is called the driving coil. The other one is for detecting the response from sample and is called the pick-up coil. This sample is loaded in the pick-up coil. Usually driving coil is much larger than the pick-up coil as driving coil needs to provide a homogeneous magnetic field for the sample in pick-up coil. The principle of the circuit is sketched in Fig. 3.2.

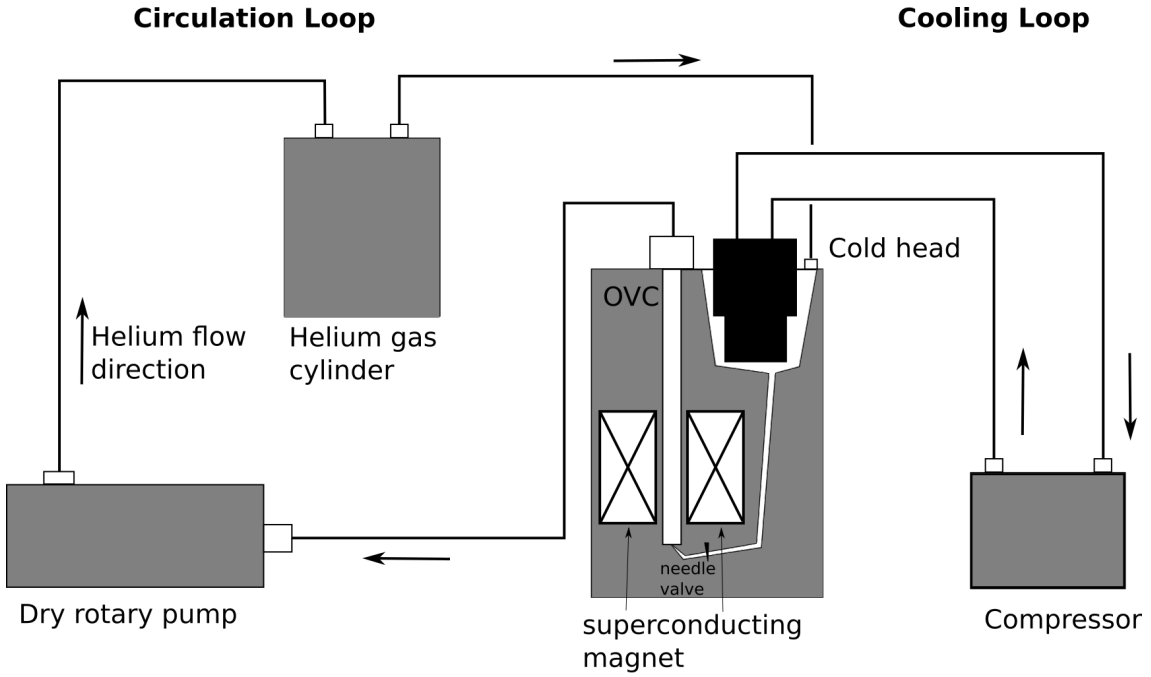

Schematical structure of dry cryogenic system

Fig. 3.1 Dry cryomagnetic system for AC magentic-susceptibility measurement of pressurised $YBa_2Cu_3O_{7-\delta}$ polycrystal. The system consists of two parts, cooling loop and circulation loop. Through the thermal contact with the cold head in the cooling loop, the circulation loop is able to cool the probe sitting in the IVC to as low as 1.4 K. The refrigeration of the cold head is carried out by a large-power compressor compressing helium gas in the cooling loop.

We assume the AC magnetic field generated by the driving coil can be written in the form

$$H_a = H_{a0} \cos \omega t. \tag{3.1}$$

From the material equations of electromagnetic theory, the total magnetic induction generated together by the external magnetic field and the induction field of the material itself is

$$H_a + M = \frac{B}{\mu_0}, \tag{3.2}$$

in which M is the magnetisation of the material, in which, in terms of χ, the magnetic susceptibility to be determined,

$$M = \chi H_a. \tag{3.3}$$

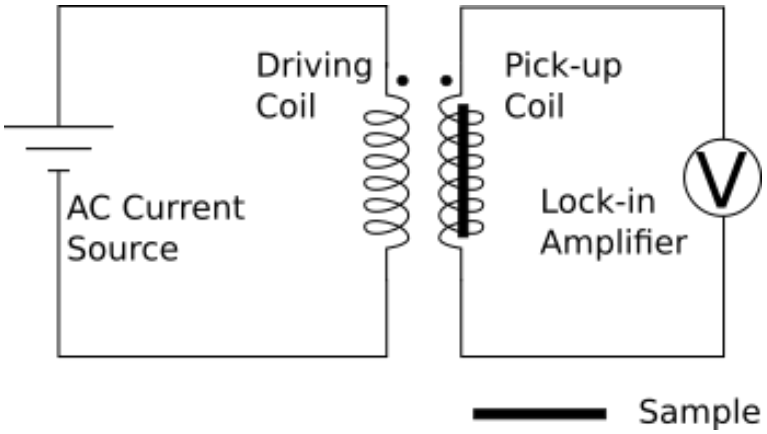

Fig. 3.2 Schematic circuit for AC magnetic-susceptibility measurements. Based on Ampere's law stating that AC current can generate a magnetic field, which will cause a diamagnetic or paramagnetic response from sample. By oscillating this signal, it can be picked as an electromotive force in a secondary coil.

With all the relations above, the magnetic field

$$B = \mu_0 \mu_r H_a \tag{3.4}$$

with μ_0 vacuum permeability and μ_r relative permeability.

Based on Faraday's law of induction, an AC magnetic field will cause an electromotive force (EMF) to be induced around in the circuit enclosing magnetic flux Φ in the field, which can be detected by a voltmeter. The value of the induced voltage can be obtained by the equation

$$\mathscr{E} = -N\frac{\partial \Phi}{\partial t} = -N\frac{\partial (BS)}{\partial t}. \tag{3.5}$$

N is the number of turns of the pick-up coil and S is the cross-sectional area of the pick-up coil.

With an AC magnetic field applied, the response from the material is also oscillating and in the complex representation with the original AC magnetic field was expressed as

$$H_a = H_{a0} e^{i\omega t}, \tag{3.6}$$

χ has components in and out-of phase

$$\chi = \chi' + i\chi''. \tag{3.7}$$

The final magnetic field will be

$$B = \mu_0 H_{a0}(\mu_r' \cos \omega t + \mu_r'' \sin \omega t). \tag{3.8}$$

where

$$\begin{aligned} \chi' &= \mu_r' - 1, \\ \chi'' &= \mu_r''. \end{aligned} \tag{3.9}$$

Chapter 4

Superconductor: Results, and Discussion

4.1 Results and Analysis of AC Magnetic Susceptibility of Pressurised $YBa_2Cu_3O_{7-\delta}$

In this section, the data collected from the AC magnetic-susceptibility measurements of pressurised $YBa_2Cu_3O_{7-\delta}$ up to 90 kbar will be presented. Following that, data analysis will be introduced and the related background will also be provided. Finally, the possible problems and the limitation of this method will be discussed and possible improvements of the experimental setup and experimental plan will be suggested.

4.1.1 AC Magnetic Susceptibility Measurement

The pressure cell with a $YBa_2Cu_3O_{7-\delta}$ sample sealed inside was mounted by screws at the bottom of the probe shown in the next section. The wires coming out the pressure cell were fixed on the outside wall of the pressure cell by GE vanish. This was to prevent the wires from vibrating in the external magnetic field. All the wires were soldered to a 24-pin lemo connector installed on the probe. The probe with the sample were then loaded into the fridge from the top of it. The helium gas keeps flushing out the space to clear the possible air. Two Stanford Research System (SRS) 124 single-channel analogue lock-in amplifiers were used for measuring AC voltage signals. An AC current source manufactured by the Electronics Workshop in Cavendish Laboratory was served to convert AC voltage from SRS 124 to AC current with the same frequency. The frequency was fixed to 1.3 kHz and the amplitude of the current was 20 mA. The sample's AC magnetic susceptibility was measured with a series of external magnetic fields applied ranging from 0 to 8 T with 0.5 T step. Due to the better

controllability of the temperature sweep while warming up, all the data were collected in this stage.

4.1.2 Data Analysis and Discussion

Fig. 4.1 and Fig. 4.2 show waterfall plots of the data of the in-phase component, X, and the out-of-phase component, Y, measured as a function of temperature for a series of DC magnetic fields.

It can be observed that at zero magnetic field a dip in the X component appears at around 70 K. In the superconducting state, superconductor shows a perfect diamagnetism when placed in an small external magnetic field with $\chi = 1$ as presented in Fig. **??** in the previous section. Based on this principle of AC magnetic susceptibility in superconductor, it was defined as the superconducting transition. However, there is a background signal that cannot be ignored, which shows a slope in the region above 80 K and below 60 K. As the magnetic field is increased, this dip gradually fades away while a peak-like feature persists. This peak-like feature was not observed in the case where the sample was un-pressurised and measured outside the pressure cell. Thus it is considered as a background signal which is dependent of magnetic field and temperature. The noisy data from 3.25 T, 3.5 T, and 3.75 T are possbily caused by the vibration of loose wires sealed inside the pressure cell. After few temperature cycles, the loose wires stuck and the noise disappeared. To extract the real signal from the raw data, the pressure cell itself needs to be measured without a sample inside under the same physical conditions. A similar background can also be seen in the Y component, while the Y component gives a clearer peak up to 4.5 T. Comparing both components, it is confirmed that the feature we choose is consistent in both components. However, due to the reason that the magnitude of the background signal increased quickly with increasing magnetic field, most of the transition points for model fit were taken from the Y component.

To extract the superconducting transition temperature carefully, the data was first smoothed to average away the noise and the first derivative was taken. Afterwards, the derivative was further smoothed to select the point which crosses the zero line to identify the minimum. The data collected at zero magnetic field is presented below (Fig. 4.3) as an example. Applying this method to all the curves at different magnetic field, a phase diagram can be drawn as shown in Fig. 4.4 in red dots. Due to the limitation of our fridge, all the data points are collected at low magnetic field below 10 T.

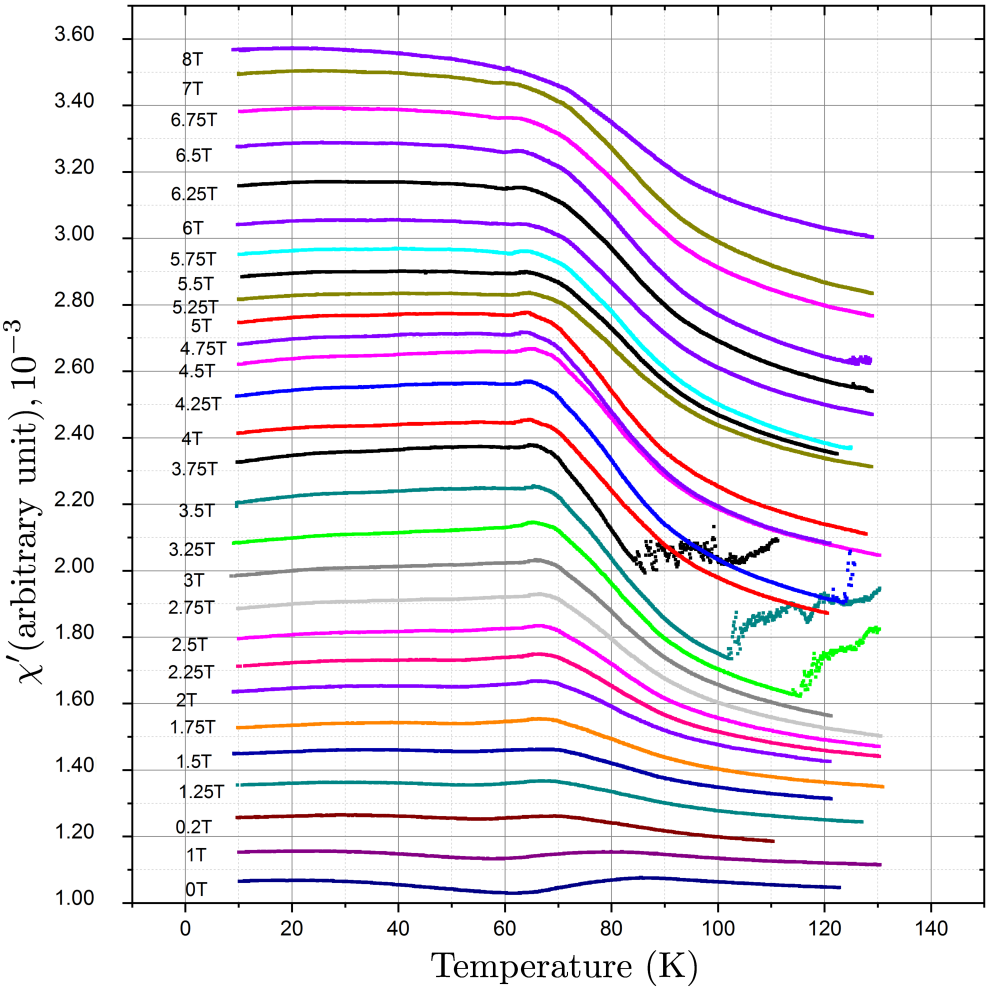

Fig. 4.1 Waterfall plot of the in-phase (X) component χ' of the AC magnetic susceptibility measurement over a series of external DC magnetic fields. The vertical axis is set to arbitrary unit. The curves from differnce magnetic fields have been offset correspondingly in order to separate them and obtain a clear view.

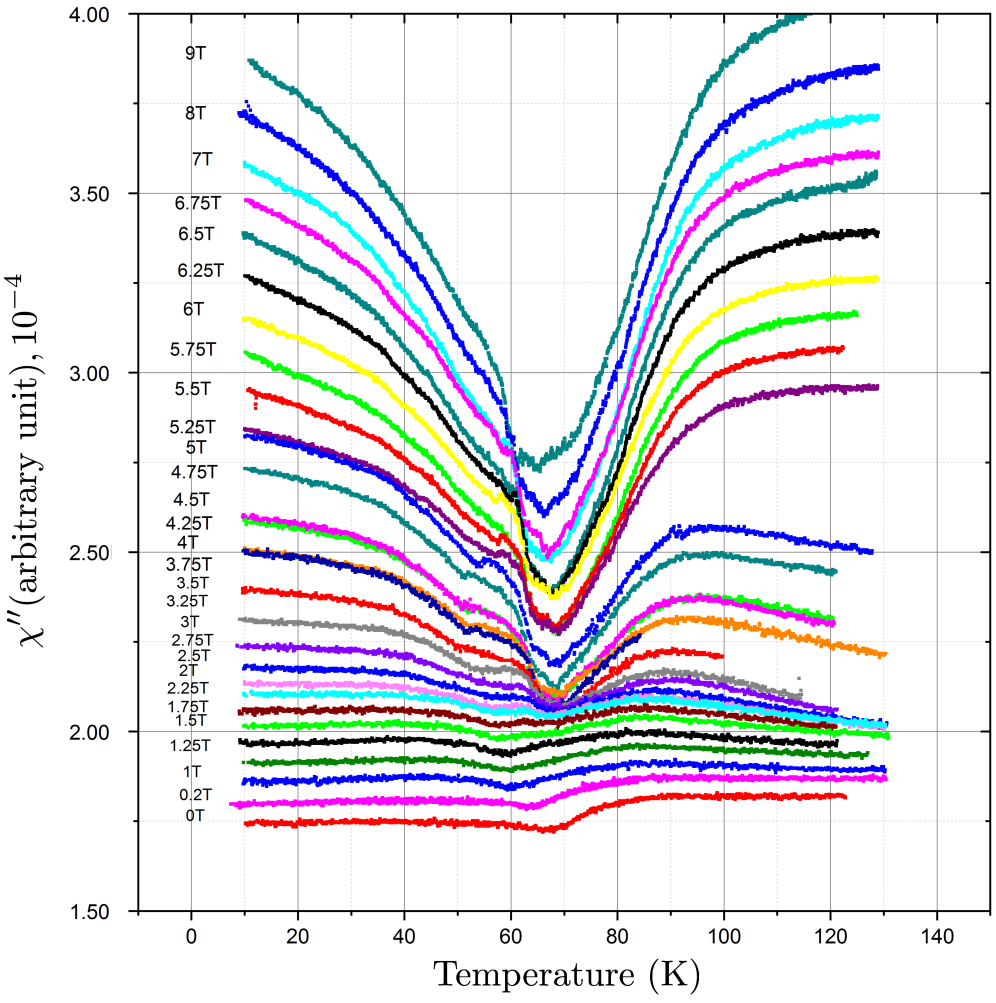

Fig. 4.2 Waterfall plot of the out-of-phase (Y) component χ'' of the AC magnetic susceptibility measurement over a series of external DC magnetic fields. Similar to Fig. 4.1, the vertical axis is with arbitrary unit and curves have been offset.

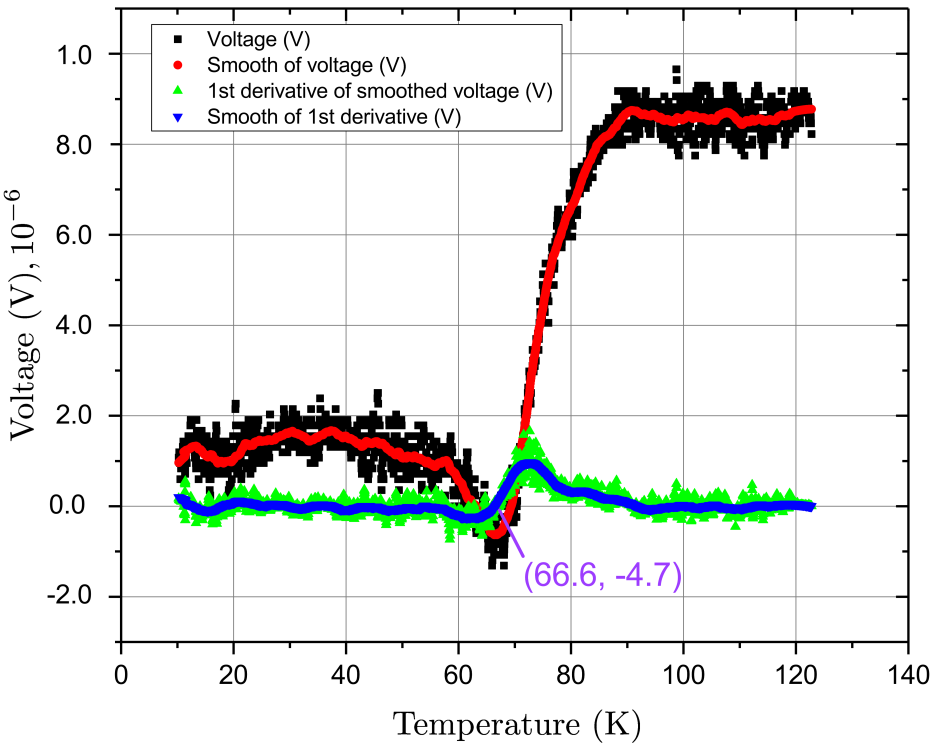

Fig. 4.3 One example of the Y component data processed from 0 T. The raw data was firstly smoothed and then took first derivative with respect to temperature. The temperature point of the first derivative at zero value is selected as the transition temperature.

In the actual experiment following the vortex physics introduced in Chapter 2, the requirement for the extremely high upper critical field (a few hundred Tesla) cannot be met as the strongest pulsed non-destructive magnetic field in the world is around 100 T well below the value needed. To draw a constructive conclusion from GL theory for experiments, Eq. 2.7 can be simplified further by assuming $b_m(t) \ll 1$ which leads to a melting line:

$$B_m(T) \approx \beta_m \frac{c_L^4}{Gi} H_{c2}(0) \left(1 - \frac{T}{T_c}\right)^2, \tag{4.1}$$

with the coefficient β_m taking the value 5.6, and the Lindemann number $c_L \sim 0.1 - 0.2$.

To explore the intriguing properties of copper-oxide superconductor in the region close to the upper critical field, various experiments such as Nernst effect and resistance measurement have been designed trying to establish a convenient method to approach it by fitting the data accessible, though not physically reaching such a high magnetic field[64, 65].

To use the data points collected from AC magnetic susceptibility to fit the overdoped melting line, *Gi* can be firstly written as:

$$Gi = \frac{1}{2}\left(\frac{k_B T_c \lambda}{\frac{4\pi}{\mu_0}[\mu_0 H_c(T=0)]^2 \xi_0^3} z\right)^2 \tag{4.2}$$

$$\approx [9.225 \times 10^8 (Wb^{-1}K^{-1}) \times \mu_0 H_{C2}(0) T_c \lambda_{ab} \lambda c]^2, \tag{4.3}$$

where $\lambda = \lambda_c/\lambda_{ab}$ is the anisotropy ratio and $H_{c2}(0) = \frac{4\pi}{\mu_0}\lambda_{ab}^2[\mu_0 H_c(T=0)]^2/\Phi_0$ is the extrapolated zero-temperature upper critical field. The table below gives all the parameters used for the least-squares fit:

Table 4.1 Parameter list for fitting zero-tempetature upper critical field of $YBa_2Cu_3O_{7-\delta}$

Transition temperature T_c (K)	Hole doping (p)	λ_{ab} (nm)	λ_c (μm)	c_L	H_{c2} (T)
86.6	0.126	133.7	4.4	0.237	31.03

The fitting started from initial values of $H_{c2}(0) = 50$ T and c_L =0.3.

The values of λ_{ab} and λ_c in overdoped high-temperature superconductor from [66, 67] were used for intraplolation. A commonly used parabolic relation [28] for hole doping and superconducting transition temperature has been employed to obtain the proper hole doping level p.

From the fitting parameters $H_{c2}(0)$ and c_L, it can be found that they match the derived data points from the references mentioned in [64, 65] quite well over a reasonable range. The assumption that an overdoped cuprate is a mirror image of an underdoped cuprate is tenable in some sense.

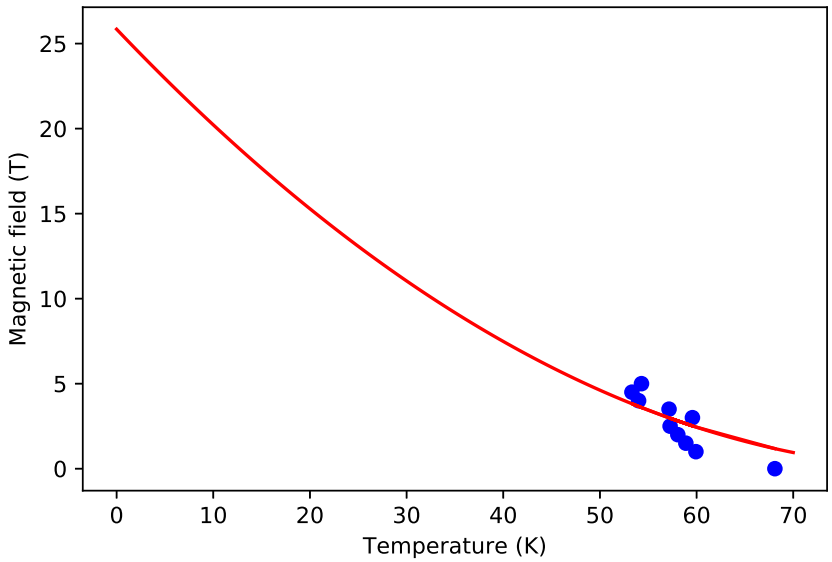

Fig. 4.4 Fitted vortex melting line using melting-transition-field model described in Blatter's review [3].

Combined with data points collected from more pressures taken later by other student, we are able to draw a phase diagram as shown in Fig. 4.5. These results have been published in [6]. All the superconducting transiton temperature T_c were measured without externally applied DC magnetic field.

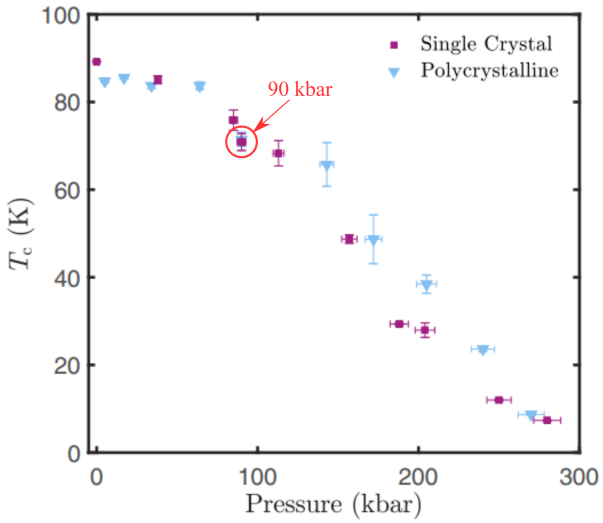

(a) Superconducting transition temperature as a function of pressure applied to $YBa_2Cu_3O_7$.

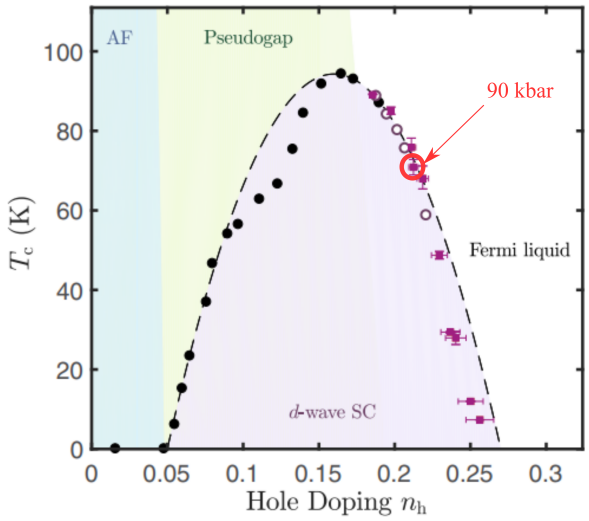

(b) Phase diagram of hole doping level against superconducting transition temperature. The overdoped data are from the pressurised $YBa_2Cu_3O_7$ in this work with adapted hole doping levels and the underdoped data from ambient pressure $YBa_2Cu_3O_{7-\delta}$ from work [4, 5].

Fig. 4.5 (a) Both polycrystals and single crystals of $YBa_2Cu_3O_7$ were pressurised and measured using the AC magnetic susceptibility technique. The data is for up to 280 kbar, where $T_c \leq 10$K. (b) Implemented phase diagram with the data points from (a) with purple solid squares for single crystals and blue triangles for polycrystals. Note that the hole doping levels on the overdoped side are actually indirectly converted from the pressurised $YBa_2Cu_3O_{7-\delta}$ samples' T_c. Each purple square corresponds to one pressure point. The hollow circles are from the calcium-doped $YBa_2Cu_3O_{7-\delta}$ experiment [4] and the filled black circles from oxygen deficient $YBa_2Cu_3O_{7-\delta}$ experiment [5] under ambient pressure. The 90 kbar point obtained in this thesis is marked. These results were published in [6].

4.1.3 Conclusions and Possible Improvements

From the data shown in the previous section, we can see that the background signal is actually very large compared with the superconducting transition signal. This was assumed to come from the pressure cell made of BeCu or the MP35N gasket with externally applied magnetic field or the deformation of the coils. However, it seems that the background signal is also temperature dependent, which was unexpected before the experiments. The second peak appearing with the increase of the magnetic field was considered to be from the same source. BeCu was used here because it is the hardest and strongest of the known copper-rich alloys once it is heat treated, and is non-magnetic. No data related to the magnetic susceptibility of BeCu at lower temperature than room temperature is found in the literatures. Besides, different concentrations of BeCu and the possible doping from other metals will affect the magnetic properties of BeCu, too. It is suggested to collect as much information about it as possible in future experiments. This information can be found from the manufacturer of the pressure cell or should be tested in the lab. That is to say that a control experiment with only the pressure cell but no sample is also necessary. This will be helpful in precisely deciding the exact position of the Y component though this may not affect the final result of the analysis.

The material used for the gasket in the DAC pressure cell is MP35N. MP35N is a nickel-cobalt base alloy which has a series of outstanding physical properties including ultra-high strength and toughness. The typical chemical composition by weight of MP35N has nickel (35%), cobalt (35%), chromium (20%), and molybdenum (10%). It has been systematically found that the magnetic susceptibility of the aged MP35N is about ten times smaller than that of the as-received paramagnetic MP35N [68]. Note that the as-received MP35N also has a weak ferromagnetic phase below a Curie temperature $T_c = 6.4$ K. In Ref. [68], the authors annealed the as-received MP35N to 550°C for 8 hours in an argon environment and quickly cooled in the air to room temperature. However, due to the reason that the superconducting diamagnetism is also very small with a tiny sample, it is possible that the reduced magnetism from the gasket is strong enough to mask it. It is recommended to test a single MP35N gasket after aging it to confirm its magnetism, especially at a temperature of a few kelvin.

Besides the removal of the background signal from the raw data, to take more data at higher DC magnetic field and lower temperature will be of benefit in deciding the melting line more decisively, as all the current data are accumulated around the low magnetic field region.

Due to the reason that this project was later transferred to other students, deeper investigations were not completed in the work for this thesis.

Chapter 5

Introduction to Sr_2IrO_4 and Ionic-Liquid Gating Technique

While the exploration of high-temperature superconductors are going on, it is also worthwhile to pay some attention to searching potential high-temperature supercondutor families. The study of Sr_2IrO_4 was firstly stimulated by this idea, because Sr_2IrO_4 shares a similar crystal structure with La_2CuO_4, as well as electronic structure and has a close relationship with *p*-wave superconductor Sr_2RuO_4 on chemical constituion. Chemical substituions have been tried to tune Sr_2IrO_4 into superconductivity though not successfully. For the project demonstrated in this thesis, ionic-liquid gating technique was applied to single crystal Sr_2IrO_4 in order to introduce carrer density cleanly without disturbing the original crystal structure and introducing chemical disorders like chemical substituions do. Ionic-liquid gating will also bring more carrier density into material by at least two orders of magnitude than chemical substituions.

5.1 Introduction to Sr_2IrO_4

In this chapter, the physical properties of Sr_2IrO_4 will be reviewed firstly with crystal structure, transport properties, and theoretical models proposed. It can be clearly seen that the links between Sr_2IrO_4 and the copper-oxide high-temperature superconductor family are represented almost everywhere which certainly triggers a hugh amount of interest in this material.

The ionic-liquid gating which was employed in this project will then be introduced to give a sketch of its development, advantages and disadvantages.

5.1.1 Crystal Structure

Sr_2IrO_4 has a distorted K_2NiF_4 structure with IrO_6 octahedra rotated along their central axis that is the crystallographic c-axis by 11° [69, 70]. This structural distortion not only reduces the space group from I4/mmm to $I4_1/\alpha cd$, but also splits the original energy band of Ir to separated subbands with energy gaps. The Fermi energy level just sits in one of the gaps giving an insulating material. La_2CuO_4, the parent material of the copper-oxide high-temperature superconductor family, has a similar structure, which is an insulator as well, as shown in Fig. 5.1.

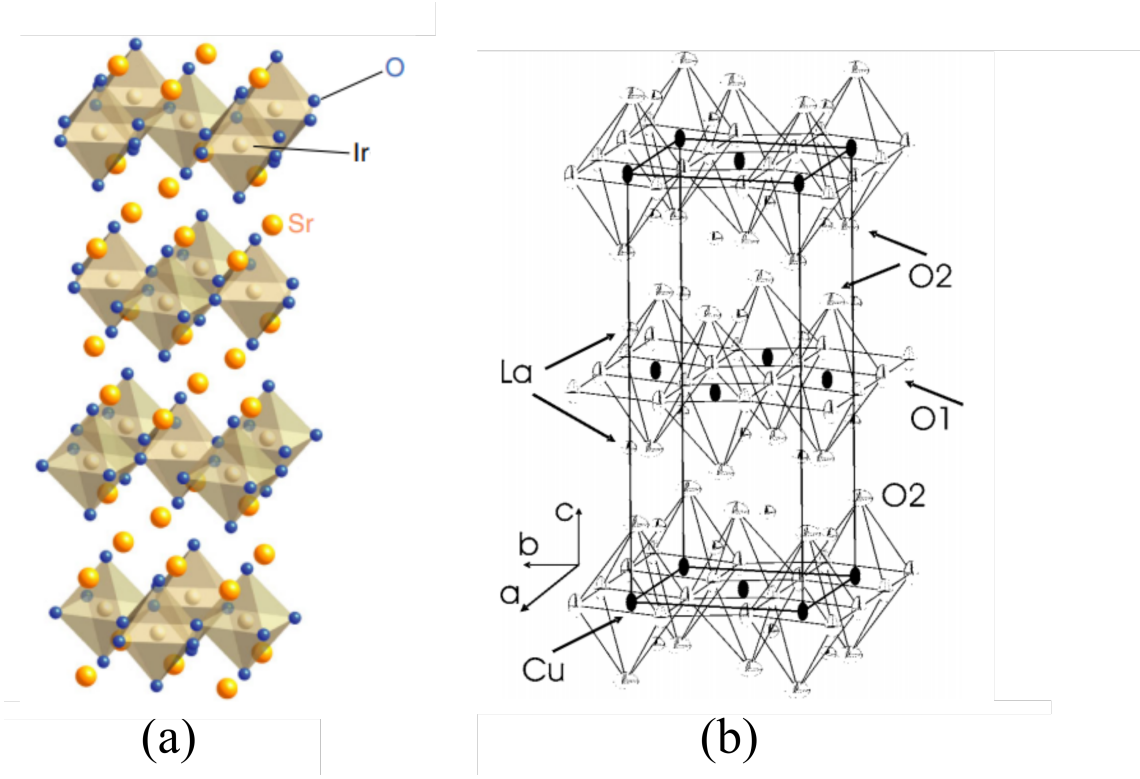

Fig. 5.1 The crystal structures of Sr_2IrO_4 (a) and La_2CuO_4 (b).Since the IrO_6 octahedra are rotated by 11° with respect to the crystallographic c-axis, the unit cell of Sr_2IrO_4 has been doubled along the c-axis, while La_2CuO_4 does not have this issue. The pictures are adapted from [7] and [8]. Copyright 2019 by American Physical Society

5.1.2 Electronic Structure

The element Ir has a strong spin-orbit coupling, which further splits the energy band into subbands. A schematic of the band diagram is shown in Fig. 5.2. Sr_2IrO_4's dominant 5d band from the Ir is split into three subbands (e_g, $J_{\text{eff}} = 1/2$, and $J_{\text{eff}} = 3/2$, J_{eff} is the effective

total angular monentum quantum number.) under the interaction between the Coulomb interaction, spin-orbit interaction, and crystal field as illustrated in Fig. 5.2 (e) [9].

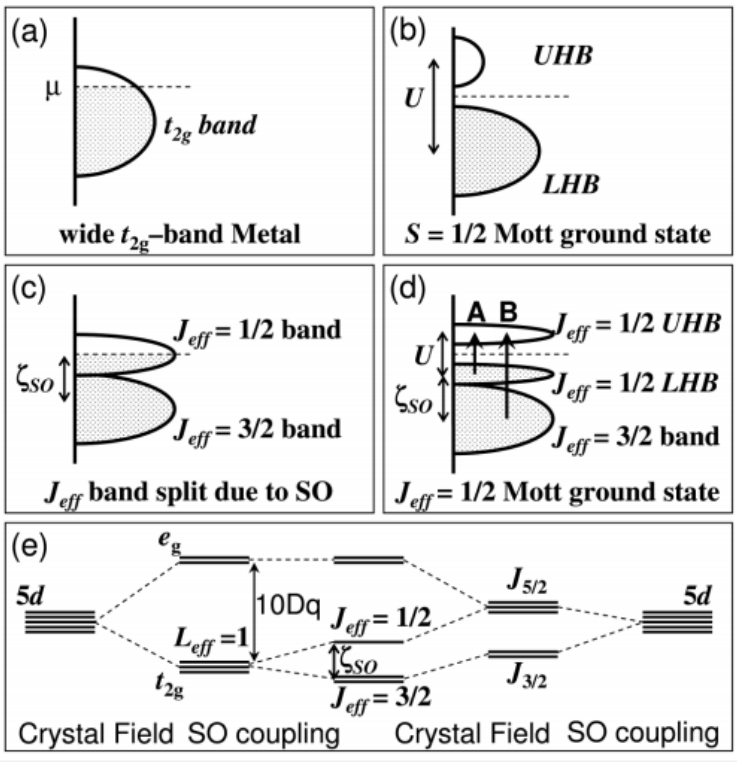

Fig. 5.2 Schematic energy band diagram of Sr_2IrO_4. (a) is the energy band of a t_{2g} band with Fermi surface locating in the band. μ denotes the chemical potential of the material. (b) is the energy band with strong Coulomb interaction U which splits the previously continuous energy band of (a) into two subbands. The upper one is called upper Hubbard band (UHB), while the lower one is called lower Hubbard band (LHB). Spin-orbit coupling interaction ξ_{SO} tends to mix two neighbouring energy bands as shown in (c). If both Coulomb interaction and spin-orbit interaction are considered, an energy gap appears from the split of the upper energy band of (c). This is the case of (d). J_{eff} is the effective total angular monentum quantum number. In the actual material of Sr_2IrO_4, the final energy band diagram forms as shown in (e) with crystal field environment. Dq denotes the unit of crystal field splitting energy. Adapted from [9]. Copyright 2019 by American Physical Society

5.1.3 Transport Properties

At around 240 K, a weak ferromagentic transition appears giving a small effective paramagnetic moment μ_{eff} ($= 0.5\mu_{\text{B}}$) [10] as shown in Fig. 5.3. This magnetic transition does not appear in the resistivity as a function of temperature, which on the contrary behaves like an insulator all the way from room temperature to 4.2 K [10, 71]. The energy gap obtained from fitting the resistance curve to variable-range-hopping (VRH) theory is about 37 meV [71].

To study the evolution of the energy gap of Sr_2IrO_4 with carrier density when it is chemically doped, element substitution and oxygen depletion were experimented and the transport properties were measured [72]. Oxygen depletion is equivalent to electron doping. It turns out that even very dilute oxygen vacancies are able to alter the physical properties of Sr_2IrO_4 greatly. From Sr_2IrO_4 to $Sr_2IrO_{4-\delta}$ (δ=0.04), the original octahedron distortion of IrO_6 is decreased and a metallic state appears at around 105 K as seen from the resistivity. Cationic substitutons of Sr or Ir reveals similar insulator-metal transition trends, though they do not fully tune Sr_2IrO_4 into a metallic state [73]. However, chemical doping has a disadvantage of introducing disorder into the system, which may create insulating behaviour.

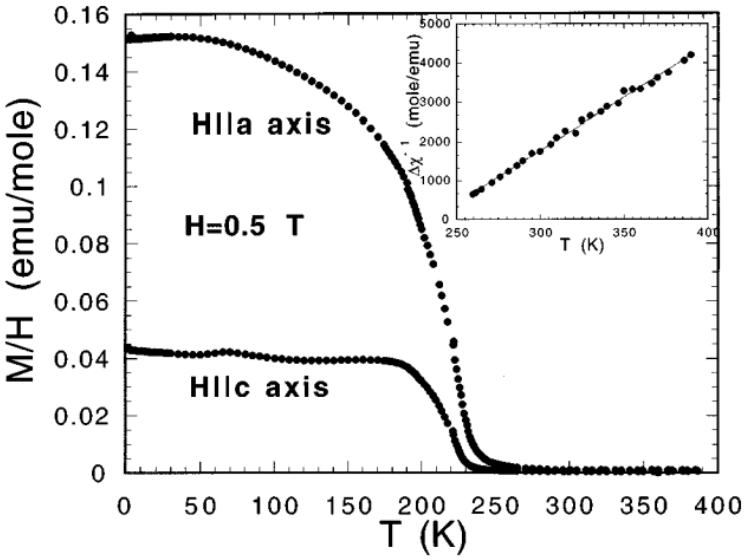

Fig. 5.3 Magnetic susceptibility with respect to temperature at $H = 0.5$ along two crystalline axes. Inset shows $\Delta\chi^{-1}$ with respect to temperature T at $T > T_M$ where $\Delta\chi = \chi(T) - \chi_0$. Adapted from [10]. Copyright 2019 by American Physical Society

5.1.4 Other Physical Properties

High-pressure have also been applied to Sr_2IrO_4 with a similar experimental idea to that on copper-oxide high-temperature superconductors, without however, being able to create a metallic ground state [11] in it. The pressure was realised with a diamond anvil pressure cell reaching up to about 70 GPa. Both X-ray absorption spectrum and resistance were measured down to liquid helium temperatures. A reduction of the energy gap was observed, but it does not close completely. This robust energy gap is an aspect that is rather different from the copper-oxide high-temperature superconductor. The Fig. 5.4 gives a good prescription of it.

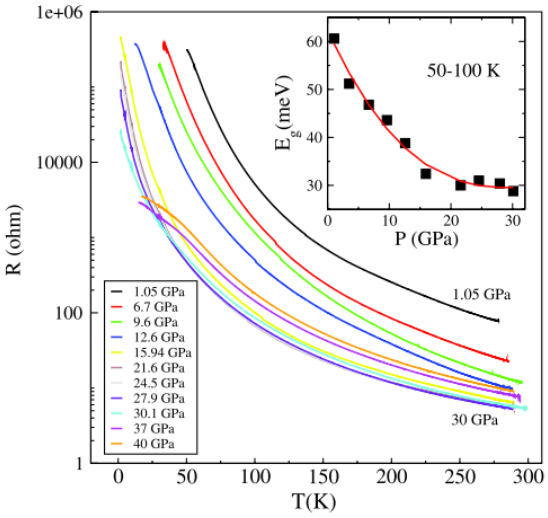

(a) Resistance vs. Temperature at various pressure from four-probe measurements in the diamond pressure cell. Inset shows an estimate of the insulating gap using $\ln R \propto E_g/2k_BT$ in the 50-100 K range. Adapted from [11].

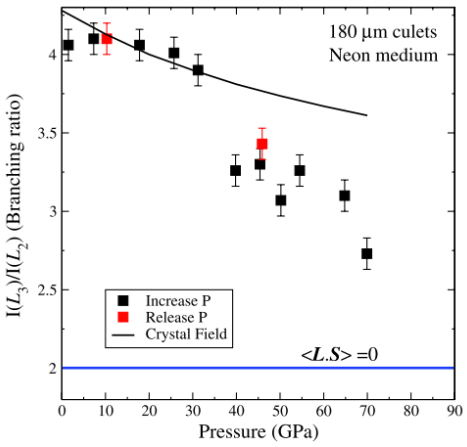

(b) Ir $L_{2,3}$ XANES data at $T = 300$K with respect to pressure up to 70 GPa, together with the derived branching ratio. Adapted from [11].

Fig. 5.4 The above results were obtained from [11] from x-ray absorption circular near edge structure (XANES) technique. $< L \times S >$ is calculated via sum rules analysis as a measure of the strength of spin-orbit coupling, therefore indicating the magnitude of energy gap of material. Copyright 2019 by American Physical Society

5.2 Ionic-Liquid Gating Technique

Besides the chemcial substitutions mentioned above, another new technique that is becoming more popular in tuning the carrier density of a material is ionic-liquid gating [74], which takes

advantage of the electrostatic field effect. This technique has advantages of introducing higher carrier density, but not disturbing original crystal structure and not introducing extra elements and disorder into the material compared with conventional chemical doping methods.

In the simplest band theory [38], an insulator is defined with only fully filled valence band and an empty conduction band, while a metal has partially filled conduction bands. In principle, introduction of a large enough amount of carrier densities to an insulating system may lead to at least one energy band being partially filled, creating a metal. Conceptually, we want to introduce carriers into the studied system, but not to modify its energy band structure.

To realise this aim, there are two possible methods. One is to use thin drain-source (DS) channels only a few nanometers thick, allowing for a small absolute number of carriers, but a large number of carrier densities ($\approx 10^{14}$ cm^{-2}). The second is to apply a large electric field across the gated channel. Conventionally, a field-effect transistor utilises a solid dielectrics separated from the channel to gate to form as a capacitor, aiming to generate the high electric field needed for switching on or off the device underneath. To introduce enough carriers into the tuned channel, high-dielectric-constant gate insulators are normally employed. The insulator is also made very thin to increase the capacitance between the gate the surface of the device. The general carrier density induced in this way to the surface of the material is about 10^{15} cm^{-2}. However, this value is not high enough to deal with highly correlated-electron oxide materials to change their physical properties as expected. The other disadvantage of using a solid medium is the difficulty of fabrication. For example, the thinnest commonly adopted oxide SiO_2 with thickness only 1 nm cannot support the required electric field. Alternative gate dielectrics are needed. To explore the properties of materials with higher carrier density, ionic-liquid gating was found to be an good solution [74, 75].

In brief, ionic-liquid gating uses a highly-polar and low-melting-point ionic-liquid on targeted material to achieve a high electrostatic field. Under external bias, the two types of carriers in the ionic-liquid will move in the opposite directions, forming an extremely thin layer of charge on the surface of the gate material. Correspondingly, the other type of charge inside the gated material will move close the surface and create a ultra thin capacitor with the charges from the ionic-liquid. The common thickness of this super capacitor is less than one nanometer, which cannot be realised by depositionic techniques as the insulator would break down in the extremely high electric field. The carrier densities observed up to now have been as high as 10^{18} cm^{-2}. From Fig. 5.5 it can be seen that two layers of electric charges are actually formed, which is termed as electric double-layer (EDL) structure.

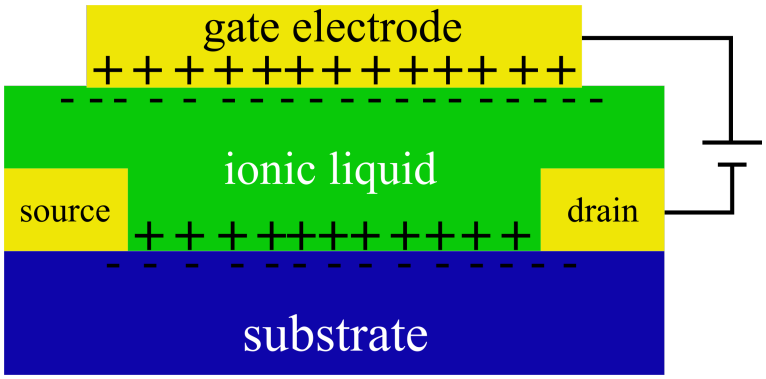

Fig. 5.5 Schematic diagram of the ionic-liquid gating technique. The substrate shown is electron doped. To obtain a hole-doped diagram, gate voltage of opposite sign is used for reversing the polarity of the current source in the picture.

Ionic-liquid gating has been employed in many experiments and has demonstrated exotic phenomena in strongly correlated materials. For example, stoichiometric $SrTiO_3$ has had superconductivity realised below 400 mK, just like the oxygen-depleted $SrTiO_3$. The difference is that the superconductivity of gated $SrTiO_3$ only occurs along the gated surface, while oxygen-depleted $SrTiO_3$ exhibits bulk behaviour. Magneto-electric coupling in tricolour superlattices such as $CaMnO_3$/$CaRuO_3$ can be tuned by the electric field generated by an ionic liquid, as well [75].

With the great potential from the ionic-liquid gating described above, we hope to apply it to explore the possibility of discovering superconductivity in Sr_2IrO_4 without introducing extra uncontrollable factors. The next chapter will present the method of fabricating devices on as-grown single crystal Sr_2IrO_4 for ionic-liquid gating experiments and will discuss possible improvement.

Chapter 6

Ionic-Liquid Gating: Techniques and Experiments

6.1 Single Crystal Growth of Sr_2IrO_4 and Characterisation

This section will introduce briefly the basic principle of single-crystal growth and the specific methed used for growing Sr_2IrO_4 in this study. X-ray diffraction, resistance and DC magnetic susceptibility measurements with respect to temperature were used to charaterise the quality of the as-grown single crystals.

6.1.1 Growth Method

High-quality single crystals are critical in condensed-matter-physics experiments in order to achieve expected results and uncover new phenomena as impurities will disturb the lattice and introduce uncontrollable parameters. In pursuit of perfect single crystals, material scientists have developed many techniques to improve crystal qualities based on their physical properties. Generally, single crystals can be classified into bulk crystals and thin film crystals. Bulk crystal will be used in this study.

Crystal growth techniques provide a range of growth methods for a variety of systems with distinct thermodynamic and kinetic properties. Specifically, materials science categorises the growth methods by the nutrient phase from which the crystals are grown, i.e. liquid phase (melt or solution), vapor phase (condensation, sublimation or reaction), or strained solid. In solid-state physics, many bulk materials studied are grown from a melt liquid. The most used methods include the Czochralski, Bridgman–Stockbarger, and float zone methods. The

single crystals used in this study were grown by the flux solution method, which involves na incongruent process of dissolving, nucleation, and growth. By carefully controlling the supersaturation and melt composition through slow cooling, the crystals grow from proper flux on the crucible walls. Normally the function of the flux is to reduce the high melting point of the mixed starting materials.

In this study, the starting materials for single crystal Sr_2IrO_4 growth consists of Sr_2CO_3, IrO_2, and $SrCl_2$ mixed in a molar ratio of 1.5:1:15 with $SrCl_2$ as the flux solvent. The mixed powder was melted in a platinum crucible sealed with a cap at 1240 °C for 10 hours for the purpose of homogeneous intermingling. Then the melt is slowly cooled down to 900 °C at a rate of 2 °C per hour. A platinum crucible is selected for its inertness and lack of erosion at high temperature, and it therefore will not leave impurity substances in the growing crystals. To improve further the size and quality of the final crystals, the crucible was placed sloping downwards to produce a temperature gradient assisting the growth of single crystals, as shown in the Fig. 6.1.

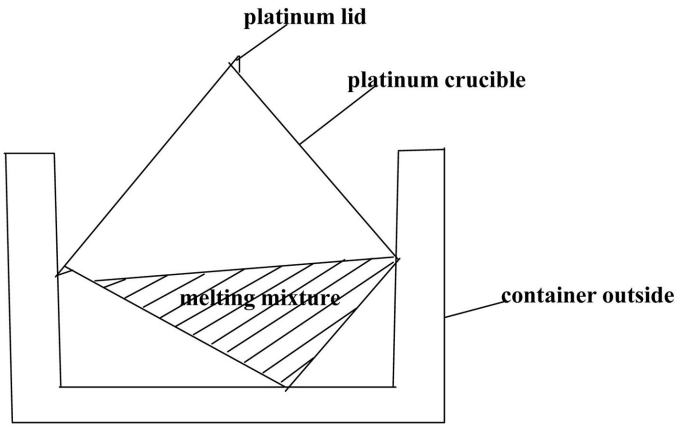

Fig. 6.1 Configuration of platinum crucible and the mixed melting in the furnace.

To further increase the size of single crystals, some small single crystals can be used as seeds for the subsequent growths. This was also experimented with, resulting in much larger ($\sim$2 mm $\times$ 2 mm) single crystals. One of them is shown in Fig. 6.2.

6.1.2 Sample Characterisation

To identify the as-grown single crystal and to inspect its quality and the possible lattice imperfections, characterization is a necessary produce after crystal growth. X-ray diffraction is used for crystal structure identification as well as identification of impure phases. Elastic scattering is assumed here. Employing X-ray beams with inelastic scattering, physical properties from other aspects can also be obtained. In this study, powder X-ray diffraction is

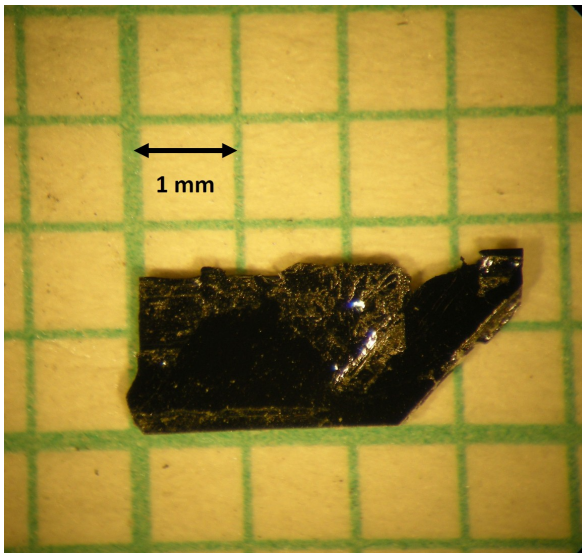

Fig. 6.2 Photo of a Sr_2IrO_4 single crystal grown by the flux solution method. The dimension of each background square is 1 mm $\times$ 1 mm.

mainly used for identifying Sr_2IrO_4 through the structure information. Beside the structural information on this material, due to the feature of the ferromagnetic transition at around 240 K in this material, DC magnetic susceptibility is taken as another characterization method.

X-ray diffraction is based on Bragg's law in which incident beams will be reflected elastically by specific lattice planes.

$$2d\sin\theta = \lambda\,. \tag{6.1}$$

d represents the inter distance of two neighbouring reflective planes, θ the incidence angle with respect to the lattice plane direction, and λ the wavelength of the incident beam. In practice, X-ray diffraction instruments will fix the X-ray detector for the reflected beam and rotate the X-ray tube emitting the X-ray beam. The angle between the X-ray detector and X-ray tube is 2θ which is normally shown as the horizontal axis in the output graph. For single-crystal X-ray diffraction, the X-ray detector can only detect a few particular lattice planes corresponding to the orientation of the crystal sitting on the sample holder of the X-ray diffraction instrument. To achieve a complete set of lattice planes for a material, powder X-ray diffraction is an easy and convenient method. The single crystal has to be ground firstly into a very fine powder to obtain all the possible lattice-plane orientations before measurement. In this thesis, to identify the grown crystal and to compare the results with previous work from other labs, powder X-ray diffraction was adopted.

The selected and cleaned single crystals were ground into very fine powder in a mortar and stuck on a round plastic slice using grease. Fig. 6.3 shows the results of powder X-ray diffraction. On comparing the powder X-ray diffraction with the PDF card in the International Center for Diffraction Data (ICDD) database, we can see the single crystal Sr_2IrO_4 I synthesized has only one very pure phase. There are no extra peaks found from impurity phases. The background signal (very broad low curve) from the sample holder of the X-ray instrument has not been removed.

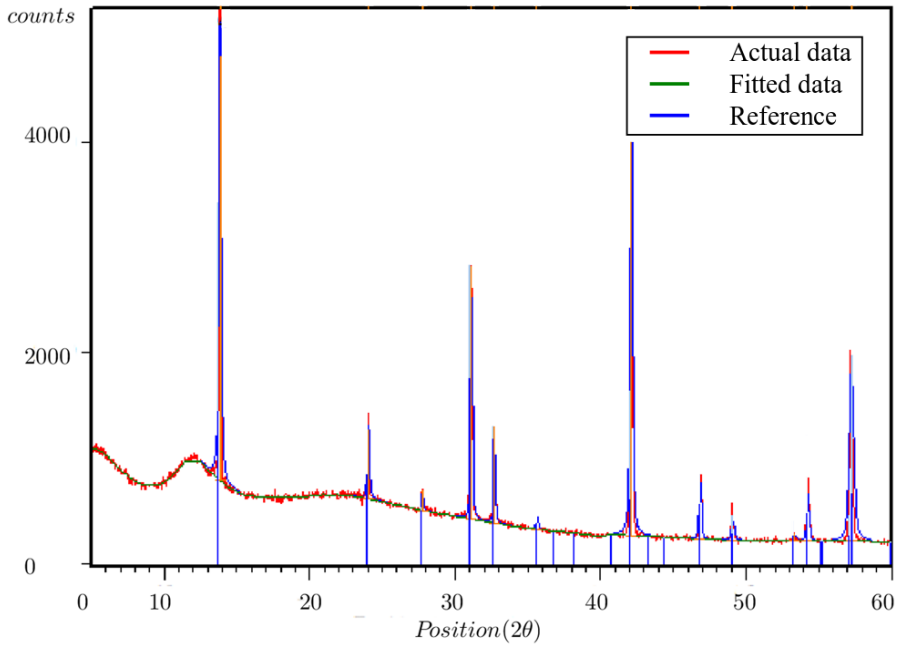

Fig. 6.3 Powder X-ray result of single crystal Sr_2IrO_4. The lines at the bottom axis are the data from ICDD database, which are references from the published literature. The curves are plotted from experimental data. The line peaks at the top axis show the peaks from the experimental sample. By comparison, there are no impurity-phase peaks from the sample, indicating its high quality.

Magnetic susceptiblilty is a measure of the degree of the magnetization of a material in response to an external magnetic field defined as $\chi = M/H$ with M magnetization and H magnetic field, providing insights into the magnetic properties of materials. Sr_2IrO_4 shows a ferromagnetic transition at around 240 K. This transition can be detcted by DC magnetic susceptibility measurement as a function of temperature.

Our magnetic susceptibility measurements were conducted on a Magnetic Properties Measurement System (MPMS) produced by Quantum Design. Inc. MPMS uses a superconducting quantum interference device (SQUID) to provide a strong signal with high sensitivity.

In detecting the magnetic response from a SQUID, a second-derivative detector array is used to collect the response from the sample. The sample was mounted in a plastic tube with a low magnetic moment before being inserted into coils array in MPMS chamber. Computer controlled temperature sweep mode was used to perform a temperature scan from 300 K to 10 K. Measurements were performed both for the magnetic field oriented along the c-axis and the ab-plane. The results (Fig. 6.4) reveal a magnetic transition at 240 K.

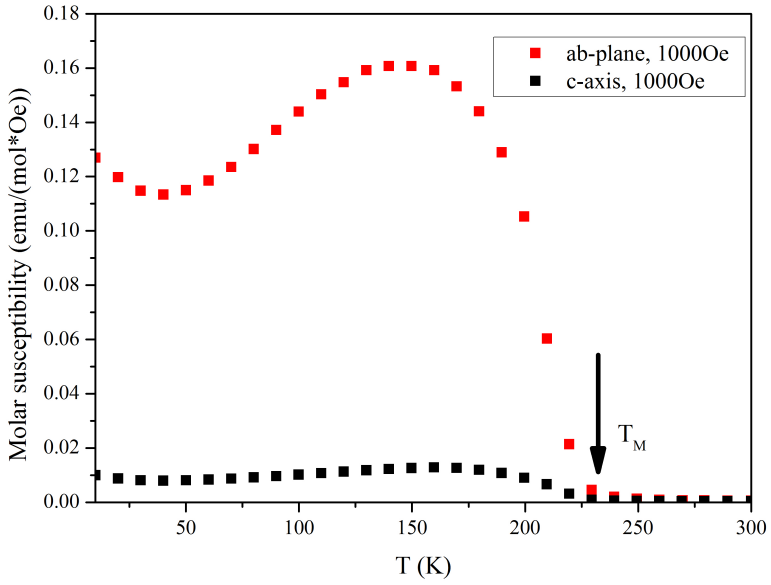

Fig. 6.4 Magnetic-susceptibility result of single crystal Sr_2IrO_4 measured using a SQUID in the Cavendish Laboratory. The red upper squares denote the magnetic susceptibility with applied magnetic field along the ab-plane. The black lower squares denote the magnetic susceptibility with magnetic field applied along the *c*-axis. The applied magnetic field used in this measurement was 1000 Oe. An obvious magnetic transition at about T_M = 240 K can be observed as indicated by the arrow in the plot.

6.2 Fabrication Techniques

6.2.1 Introduction

This section is about the fabrication of Sr_2IrO_4 and $SrTiO_3$ single crystals for gating experiments. Firstly, the basic principles of optical lithography and electron-beam (e-beam) lithography will be introduced. The routine procedures for a general lithography process are then listed. Optical lithography is mainly applied on $SrTiO_3$ single crystal for its flat top

surface and relatively large area. Secondly, the focused-ion beam (FIB) technique used for Sr_2IrO_4 device fabrication is presented.

6.2.2 Lithography Techniques

Optical Lithography

Optical lithography patterns a polymer-coating layer by passing UV light into a specific area through the transparent part of a photomask. UV light breaks the long polymer chains of a positive photoresist, which are easily removed by a solvent, called a developer. For a negative photoresist, UV light cross-links molecules so that they cannot be removed by a solvent. The basic process of optical lithography consists of substrate cleaning, photoresist spin-coating, pre-exposure baking, mask alignment, exposure, and development in sequence, as will be described in more detail below.

Surface treatment before photoresist spin-coating is a necessary step in reducing the possible impurities, including solvent traces and dirt. As the dimensions of the features to be patterned can be as small as a few micrometers long, a small dirty point may cause unsuccessful fabrication. This is also why all cleanrooms for nano-lithography process have strict standards with regards to the temperature, moisture, and air cleanliness. Using acetone and isopropanol for washing substrates in an ultrasonic bath and drying with compressed ntrogen followed by hotplate baking can remove most of the dirt and solvents. If a higher standard of surface cleanliness is required, oxygen plasma ashing can be helpful.

The second step is to spin coat a layer of photoresist on top of the sample. The homogeneity of the coated photoresist is extremely crucial to the final result. Due to surface tension, photoresist tends to accumulate around the surface edges of the samples, forming a much thicker film. Thus under the same exposure dose, some photoresist will remain along the sample edge while the photoresist in the center is completely removed. In the subsequent metal evaporation, metal can only reach the central region without photoresist, but leaving broken patterns surrounding. Edge bead removal of exposing the edges for a much longer time firstly under UV light can be adopted before actual exposure. For large samples, this is less of a problem.

As photoresist contains solvent, a baking step is necesary to drive it out. Either oven or hotplate can be used for this purpose. An oven is able to generate a homogeneous temperature and is recommended. For fast baking, a hotplate is more convenient. The baking temperature varies for different photoresists. Manufacturers of the photoresists usually provide related technical data sheets as references for users.

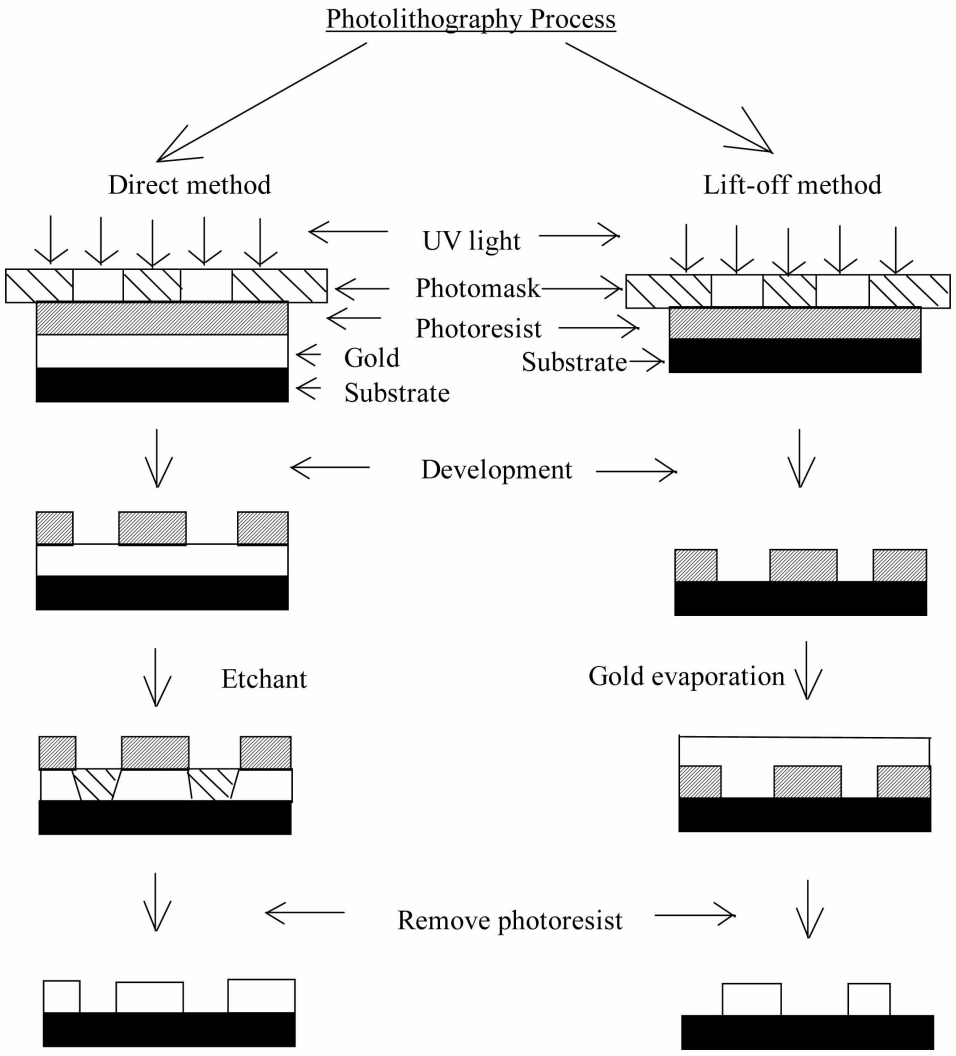

Fig. 6.5 Direct method and lift-off method for photolithography process. In this illustration, positive photoresist is applied. The blank area of photomask denotes the transparent region on the photo mask, which is designed for letting UV light go through, while the rest of the mask is opague. After UV light exposure, a developer is used to removed the uncrossed-linked photoresist.

The next step is alignment which requires the coated substrate to be positioned precisely beneath the specific pattern of the mask. For multiple-layer structure, this precise alignment is critical, because in view of the tiny dimensions of the features even small deviation will cause a significant mismatch. One of the common tricks to make this process easier is to leave some shaped small windows on the photomask around the main features to show directions.

Next, contact sample with the photomask and expose the photoresist with UV light. The mask has to be clean enough to avoid impurities blocking the UV light. Acetone, isoproponal, deionized water, and compressed nitrogen gas are the tools commonly used to clean masks. The exposure time is determined by the type of the photoresist and the thickness of the photoresist layer. The accurate parameters may vary and need detailed tests.

Then we need to develop (remove) the exposed photoresist. The exposed resist photoresist can dissolve in certain chemicals called developer much faster than the linked does. Thus by controlling the development time properly, a clear, shaped pattern can be obtained. The selectiveness of developers also varies with respect to photoresists.

After photoresist development, etching, metal evaporation, or other process are feasible according to experimental designs. Just remember to remove the left photoresist in the final step afterwards with acetone, isoproponol, and compressed nitrogen gas.

The schematic of the process flow is shown in Fig. 6.5. The left column is the direct method employing etching to remove predeposited metal while the right column is the lift-off method in which metal is deposited after the development. Due to the better resolution given by the lift-off method, it is widely used.

Electron-Beam (E-beam) Lithography

E-beam lithography has similar lithographic procedures to optical lithography, except for using e-beam resist as a replacement for photoresist and being exposed by an electron beam instead of UV light. With the much shorter wavelength of high-energy electrons, e-beam lithography can normally reach much higher resolution than optical lithography. The other advantage of e-beam lithography is that it is maskless. Users only need to submit a computer-designed document to the computer controlling the electron beam scanning, which gives more flexibility to researchers.

Basic Principle of Focused-Ion Beam (FIB) Lithography

A focused-ion beam (FIB) microscope is a scanning-ion microscope integrated with milling and deposition functions besides the basic imaging function. Simply speaking, FIB can be constructed by replacing the electron-beam column in a scanning-electron microscope with

ion-beam column. Due to the flexibility of FIB, it has been extensively used in physics, materials science, and biological research in the last decades.

A typical FIB system contains an ion source, lense system, sample stage, vacuum chamber, and controlling computer. The ion source used in most FIB systems is a so-called liquid-metal ion source (LMIS) which can form a tightly focused beam to achieve a high resoluton. The gallium beats other metals being used in the LMIS with its low melting temperature, low volatility, and low vapor pressure. The relatively simple physical properties of gallium make LIMS easy to manufacture. Practically, Ga^+ ions on the needle tip are attracted by a strong electric field whose strength can reach as high as 10^{10} V/m. Then a single Taylor cone will generate current from the needle tip, being a balance between the electrostatic force and the Ga^+ surface tension. The current usually ranges from 5 pA to 80 nA. The current goes through a system of lenses that focuse it onto the sample. The secondery electrons coming out of the sample surface after the Ga^+ beam collides with the sample will be collected for imaging purpose.

For a dual-beam system incorporating both a FIB and a SEM in a single system, the axes of the ion-beam column and the electron-beam column meet at a point called the eucentric point to coordinate the fabrication using the ion column with the imaging of electron beam. At the eucentric point, tilting the sample stage will not move the sample away from the central view of either column. This offers a special advantage over the single-beam-FIB system, which is nondestructive imaging during the milling process. The ion-beam imaging evitably introduces damage to the sample surface due to the large energy of ions compared with that of the electrons when hitting the target. The level of the damage caused depends on the strength of the beam current (accelerating voltage and current) and incident angle with respect to sample surface. If the view of the sample is always coming from the ion beam, it will definitely destroy the sample in time. However, with a SEM beam which only introduces some electrons, the damage to the sample be reduced to the minimum. Fig. 6.6 give a typical configuration of a dual-beam system.

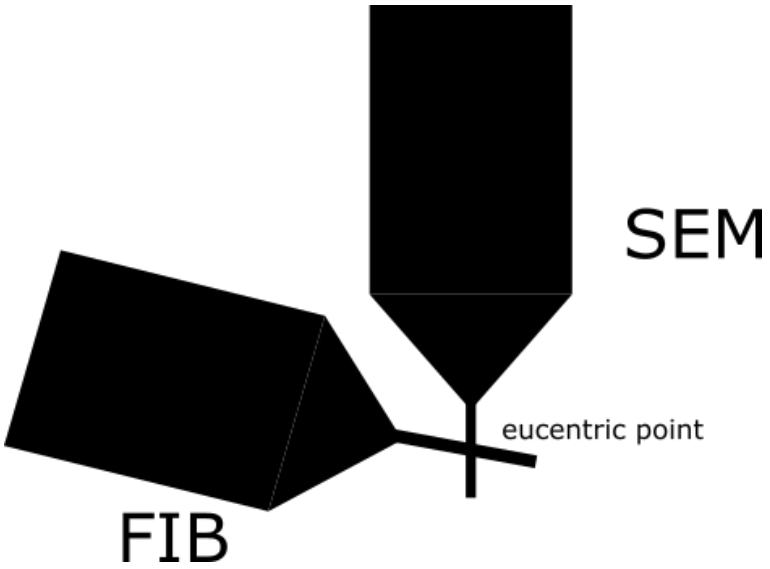

Fig. 6.6 Typical dual-beam FIB-SEM system configuration. The meeting point of the FIB column and SEM column is at the eucentric point. This point is the one that stays fixed ahwen rotating. Placing sample at eucentric point can keep the sample image in the center of the SEM and the FIB windows while rotating the stage.

Based on the principle of chemical vapor deposition (CVD) of a precursor organometallic gas, FIB can also be used for mask-less metal (platinum tungsten) deposition with the aid of precursors. This function attributes to the gas delivery system in conjunction with either the ion beam or the electron beam. The precursor flow is injected towards the sample surface before being hit by the ion beam. The collision decomposes the precursor and leaves only a platinum or tungsten film in the region struck. These films are not pure metals, but compounds containing carbon and other elements. The contact resistances for transport measurements of materials created by FIB are generally considerably high. Many studies [76, 77] have explored this problem and tried to find methods to improve the purity of the film, such as annealing. However, the improvement is very limited. More research in this field is expected.

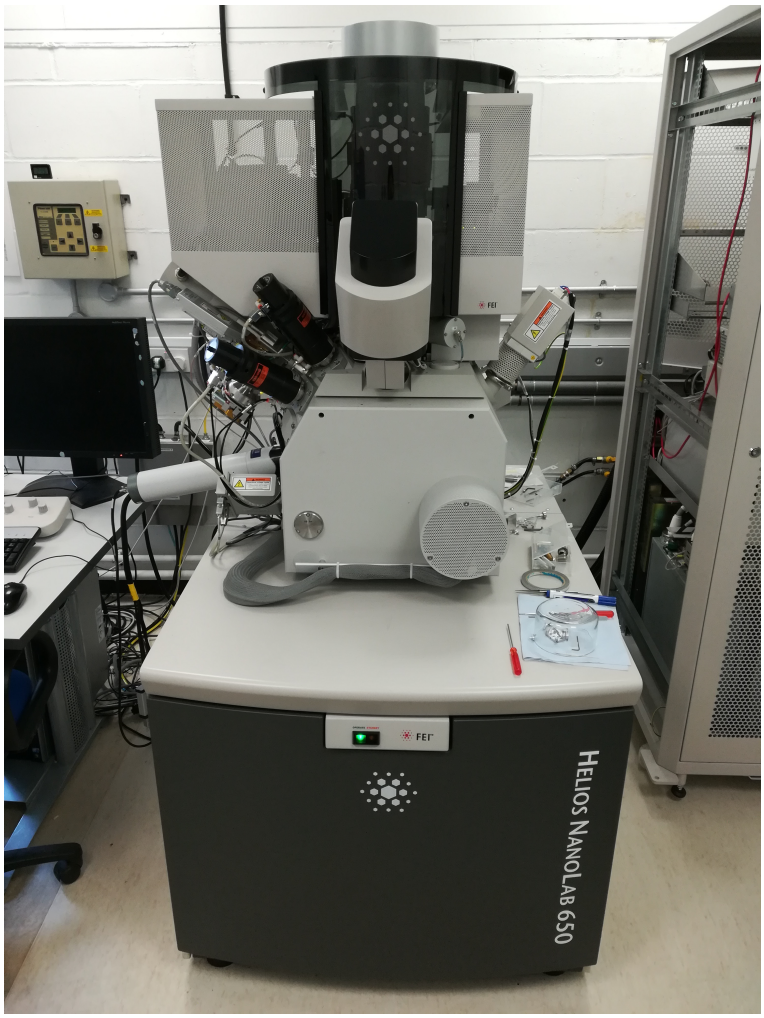

Fig. 6.7 The Helios Nanolab 650 dual-beam FIB-SEM system is located in the SEM suite, Cavendish Laboratory, University of Cambridge, and was installed in 2013. This is the main instrument used for Sr_2IrO_4 device fabrication in this thesis.

The Helios Nanolab 650 dual-beam FIB-SEM system from FEI (Field Electron and Ion Company) in Fig. 6.7 was mainly used for the specimen preparation and fabrication work on as-grown single crystal Sr_2IrO_4. This is a powerful dual-beam system integrated with a self-guiding system, which uses a step motor to move the sample stage to the position selected on the screen providing great convenience for operating samples. Its resolution can reach few nanometers. It has a strong pumping system which can keep the FIB always at high vacuum meeting the requirement for high-standard imaging and milling work as shown in Fig. 6.8.

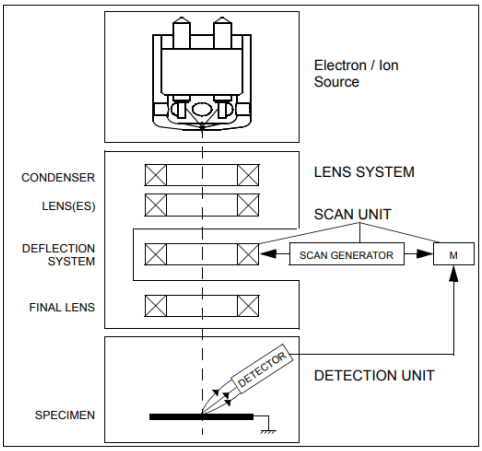

(a) Column schematic overview for the Nanolab dual-beam FIB-SEM system produced by FEI company.

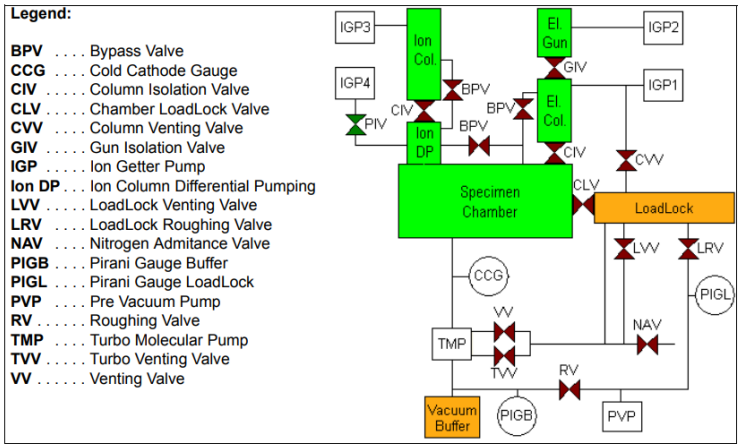

(b) Vacuum system of Nanolab dual-beam FIB-SEM system.

Fig. 6.8 Pictures from the manual of Nanolab 650 system showing a schematic of either columns and the pumping system.

Chapter 7

Ionic-Liquid Gating: Results, and Discussions

7.1 Sr_2IrO_4 & $SrTiO_3$ Fabrication Results

7.1.1 Sr_2IrO_4 Fabrication using A Focused-Ion Beam

Fabrication of as-grown single crystal Sr_2IrO_4 encounters several difficulties. The first is the fabication itself. Due to the irregular shape of as-grown single crystal Sr_2IrO_4, the conventional nanolithography technique cannot be applied directly. For instance, photoresist cannot be spread homogeneously on top of single crystals as its top area is too small ($\sim 1 \times 1$ mm^2). All subsequent processes suspended and the metal contacts thus are impossible to be carried out using lithography. To overcome this, either growing larger single crystals or reducing the single crystal thickness can be helpful. However, both methods are very time-consuming and the results are unpredictable. If we instead apply silver paint or conducting epoxy manually to draw contacts, defining clear contact region and working on a sub-micron area will be new problems, both of which are no easier than the initial one. Worse still, the silver epoxy is likely to react with the ionic liquid during the charging process in the gating experiments and spoil the controlled experiments with unknown chemical reactions. Therefore, there is a need for a new compatable fabrication technique. The development of FIB lithography meets our requirements.

The crystal was firstly selected from the cleaved pieces of Sr_2IrO_4 and picked by toothpick. The static electric charge between the toothpick and the crystal is strong enough to hold the crystal until the crystal touches the epoxy on a substrate. The epoxy is used for integrating an even surface with the crystal flake. Then the single crystal will be much easier to handle. The next step is to evaporate a thick layer of Ti/Au on the substrate. The key is to sure the metal

is continuous everywhere, which is critical to the subsequent FIB fabrication. Fortunately, we can still fix it using the platinum depostion of FIB even if there are some places broken. Then FIB will mill a Hall-bar on the crystal flake as illustrated in Fig. 7.2.

The detailed FIB fabrication process for Sr_4IrO_4 is listed below.

The procedures of fabricating Sr_2IrO_4 by FIB:

1. Select a piece of single crystal with relatively large surface and low thickness.
2. Clean the surface with distilled water and ethonal using a cotton bud.
3. Electric polishing can be used if necessary.
4. Prepare Epoxy 2850 mixed with Catalyst 9 in the ratio of 100:3.5 followed by bubble-removal step in a vacuum desiccator for 15 minutes.
5. Drop a small piece of the prepared epoxy 2850 in step 4 with similar size as the selected single crystal in the centre of a cleaned quartz substrate (5 mm$\times$5 mm).
6. Place on the selected single crystal with the smooth surface upwards on the epoxy. Let it sink naturally and the fluid fill all the gaps forming a complete surface.
7. Wait for the epoxy to set for at least 3 days. This is critical for the subsequent steps as the high temperature generated in the metal evaporation will deform the incompletely cured epoxy and crack the evaporated metal layer.
8. Evaporate a metal layer (Ti/Au = 15 nm/200 nm) covering the whole substrate, cured epoxy, and single crystal.
9. Use FIB to carve a Hall-bar shape in the center of the single crystal. Make sure the milling cuts through the single crystal and reaches to the top of the substrate. (If it was not cut through, the electric current may not go through the Hall-bar channel as expected, but through the cutting originally for separating the metal contacts. This may be the reason that no reasonable Hall signal can be obtained in the magnetic field measurements).
10. Bond the completed device using a wire bonder to a 20-pin leadless chip carrier.
11. Test the device to make sure there are no shorts at room temperature.

Typical resulting devices are shown in Fig. 7.2 and Fig. 7.3.

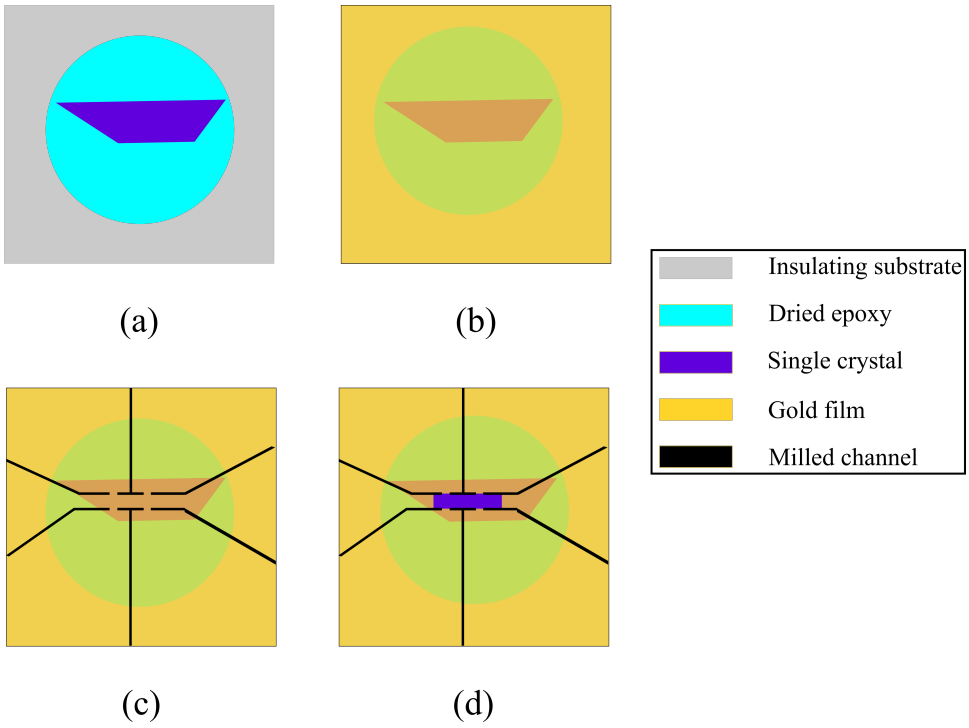

Fig. 7.1 Schematics of the fabrication process of as-grown single crystal Sr_2IrO_4. (a) Embed single crystal into epoxy before it cures. If the flake is too small to sink, a toothpick can be used to press it slightly to ensure that the surface of the flake is roughly forming a level surface with the epoxy. This step is critical as it is needed to guarantee a continuous gold film for the step (b). (b) Deposit a layer of gold film onto the whole substrate covering both the single crystal and the epoxy. This film can effectively conduct the electrons from the SEM colume and lead to a good resolution of image. (c) Use FIB to mill channels to separate the gold film into several pieces, each corresponding to a contact branch to the Hall bar. (d) Use FIB to slowly remove the gold film in the central region of the single crystal. The milling rate should be calibrated beforehand in order to precisely remove the gold, but not so much that the crystal surface is damaged significantly.

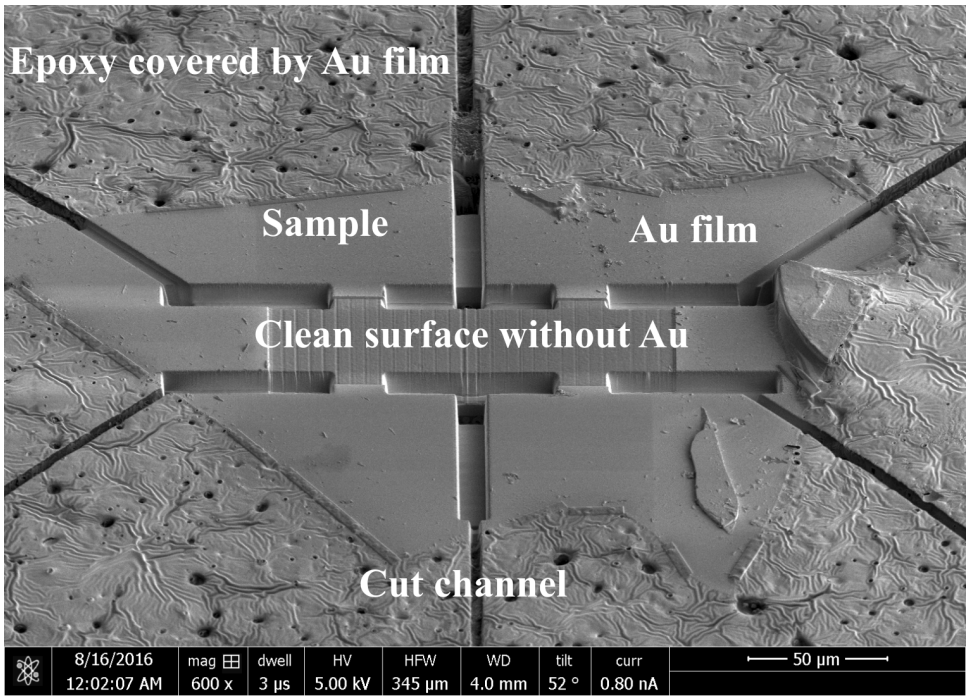

Fig. 7.2 SEM photo of FIB patterned large single crystal Sr_2IrO_4 sample. In this device, a complete piece of single crystal was used. The procedures for the process are the same as used in small flakes. The channel area is larger than that for small flakes which requires longer milling under small ion milling current. Due to the resolution limit at low ion current, the removal of the gold layer on the channel was conducted step by step with small strips shown in the figure. The resistance was measured after the fabrication to confirm no electrical shorts remained.

Table 7.1 Comparison of three types of fabrication method to contact as-grown single crystal Sr_2IrO_4.

Fabrication Method	Advantages	Disadvantage
Silver Epoxy	Low cost and no preference to the shape of samples	Easy to peel off the sample and cannot be used on small samples
Photolithography	Standard process recipe	Cannot deal with special samples like as-grown single crystal with rough surface
FIB	Can be adapted to samples with varying shapes and surface morphology	Takes long time to process

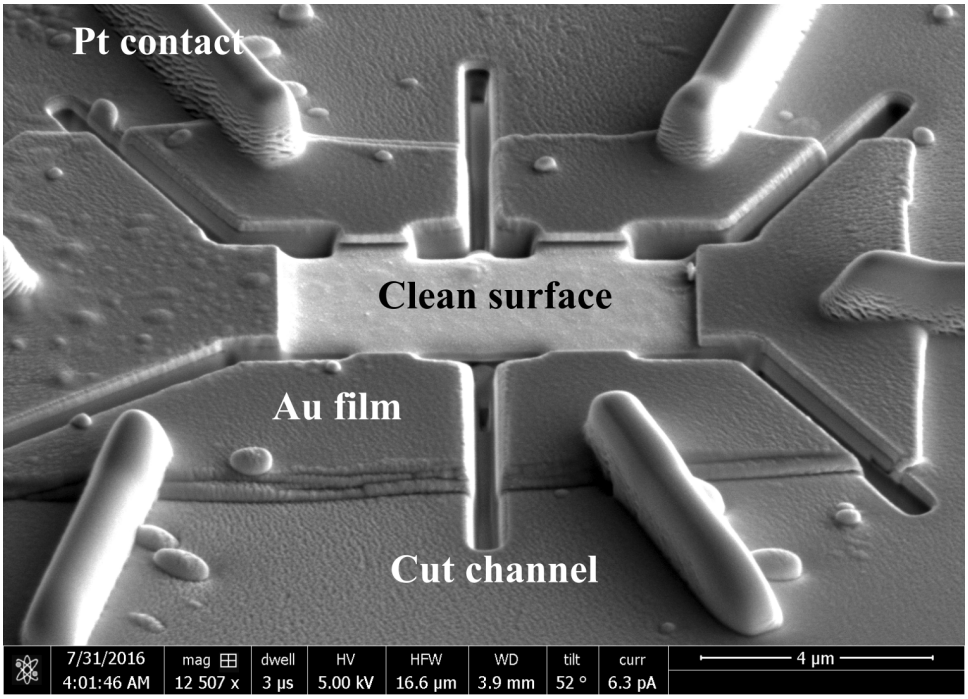

Fig. 7.3 SEM photo of FIB patterned Sr_2IrO_4 flake. The flake used here is as small as 10 μm, which is cleaved directly from a large piece of single crystal by a scotch-tape method and transferred to SiO_2 wafer. The cutting is through the sample down to the substrate. Thus each electrode is not short with each other. A titanium/gold coating was applied before the FIB processing. Then FIB induced platinum deposition was employed to connect the electrodes of Hall-bar-shaped flake to the gold layer on the substrate.

In the exploration of the proper procedures to fabricate a practical device, either small thin flakes cleaved from large pieces of single crystal or original large single crystals were tried. Small flakes are easy to process in the FIB chamber using milling and deposition functions. Small ion current with less damage to samples can achieve a shaped device in short time as shown in Fig. 7.3. However, this type of device would not last more than one thermal cycle in the subsequent resistance test as a function of temperature. The problem may come from the incomplete removal of the titanium layer on top of the sample, which always leads to the breaking of the electrodes of the Hall bar due to the electric current passing through. On the other hand, milling too deep may also cause crack of the thin flakes. After using large pieces of single crystal, similar issuea never occurred again because the top metal layer can be removed completely by milling deeper than the metal thickness without worrying about cutting off the device. The point to be noticed for thick single crystal is that the cut defining a Hall bar on the single crystal has to be going right through the crystal, or else the cut region will still be conducting. The detailed procedures listed above are for using large single crystal.

7.1.2 $SrTiO_3$ Fabrication Results by Photolithography

The mask design for four-terminal measurement of $SrTiO_3$ is shown in Fig. 7.4. There are in total 6 pairs of voltage contacts positioned along the both sides of channel. This is to ensure that the device is still working with few voltage contacts failed. The ratio of width to length of the channel is designed to be smaller than 10 to minimize the geometrical effect when external magnetic field is applied [78].

It is found that hydrogen flouride (HF) can selectively etch away the SrO layer of Sr_2IrO_4 leaving only TiO_2 layers. In order to achieve a fixed $SrTiO_3$ surface structure with less influence from other structural defects, 4×4 mm^2 $SrTiO_3$ was purchased from CRYSTAL GmbH with orientation (100) and was polished on one-side. It was firstly HF-etched for 1 minute and then annealed in air at an temperature of 950 °C for 12 hours to fully oxygenate it and stabilise its surface. This surface-treatment method has proved to be successful in several similar experiment [79, 80].

With standard size and atomically flat surface, $SrTiO_3$ can be processed by conventional photolithography and e-beam lithography to achieve devices for gating experiments. Due to the very low carrier density inside $SrTiO_3$ and the large energy gap, to enssure that the contacts between the bulk $SrTiO_3$ and the metal electrodes are ohmic, the surface of the $SrTiO_3$ needs to be treated firstly to form a layer with reduced barrier height. Argon ion milling is an effective method for this. We adapted the previous reseach [79, 80] studying

Table 7.2 Samplie list of Sr_2IrO_4 for optimisation of FIB parameters

Date	Sample No.	Comment
04/12/2015	SIO001	Direct milling on bare single crystal flake; direct Pt deposition on cut single crystal flake; strong charging effect under 1 nA current.
09/12/2015	SIO002	Following SIO001, try charge neutraliser embedded in FIB; less charge than SIO001.
11/01/2016	SIO003	Following SIO002, try charge neutraliser embedded in FIB with smaller deposition current 100 pA.
01/02/2016	SIO004	Further optimised the setup used for SIO003, charging was still serious with 10 pA, and the deposited Pt contacts were not continuous and open.
11/02/2016	SIO005	Coated a test glass slide with Au film; milled it with 1 nA; deposited Pt film with 100 pA; stable imaging with negligible drift.
05/03/2016	SIO006	Coating large single crystal (1mm^2) with Au; mill and remove the coating to shape a Hall bar; takes 2 days to finish; the Au was not removed completely, need deeper milling next time.
29/04/2016	SIO008	Coating small single crystal flake (100nm^2) with Au; mill and remove the coating to shape a Hall bar; milled deeper than SIO009; used smaller milling current than SIO010 to reduce the damage to sample.
08/07/2016	SIO008	Contacts on sample degraded in the air.
18/07/2016	SIO009	Double checked the sample degradation with a similar sample; it was confirmed that the sample needs to stay in vacuum.
29/07/2016	SIO011	Coating small single crystal flake (100nm^2) with Au; mill and remove the coating to shape a Hall bar; milled deeper than SIO009; used smaller milling current than SIO010 to reduce the damage to sample.
06/08/2016	SIO012	Milled coated small single crystal flake (100nm^2); took 1 h to finish; deposited Pt contact with 10 pA; successfully done; stored in vacuum desiccator.
24/08/2016	SIO013	Repeat the procedures used for SIO012, the fabrication was completed successfully; stored in vacuum desiccator.

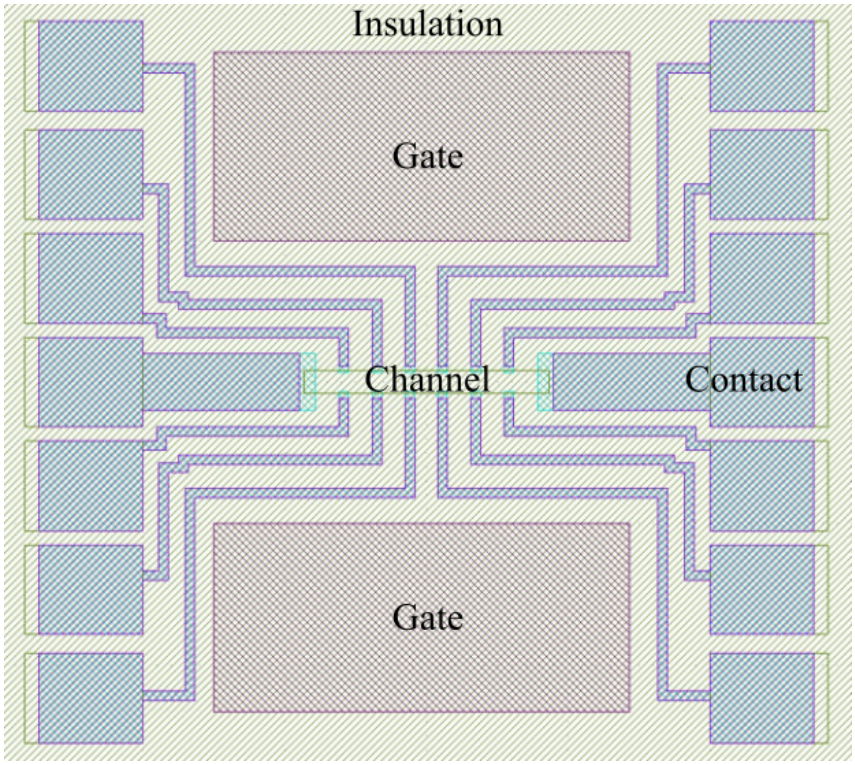

(a) Full mask design for ionic liquid gating. The channel in the central region was left clean in the fabrication process and was gated in experiments.

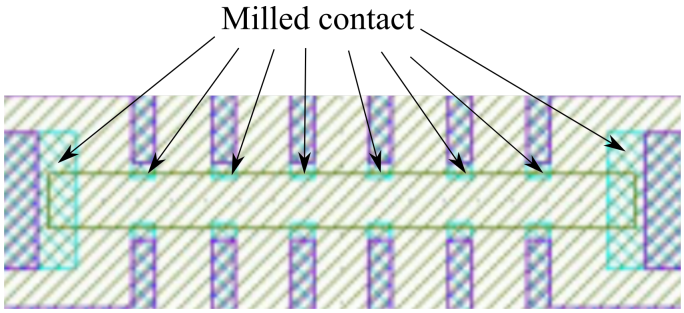

(b) Zoomed-in picture of the mask design around the Hall bar in (a).

Fig. 7.4 Mask design for the Sr_2IrO_4 ionic-liquid experiment. (a) is the full mask design with all layers stacked together. (b) is the zoomed-in channel region to illustrate the details of the argon-milled contacts. The metal contacts were evaporated after 150 nm was argon milled away beforehand to create enough oxygen vacancies to form ohmic contact for the later transport measurements during the gating process.

the conditions under which a lower contact resistance can be obtained to suit the argon ion milling facility we have.

After argon milling, the ohmic contact Ti/Au is thermally evaporated onto the milled region except for the gated channel, which is supposed to be left for ionic liquid gating. Then a layer of Al_2O_{3-x} insulating film is evaporated onto the device aiming to cover the ohmic contacts. This was introduced to overcome current leakage during the gating process and the subsequent measurements. Two final large gate pads were evaporated just over the insulating layer. Using big gate pads ensurea a homogeneous electric field can be generated between the ionic liquid and the channel along its whole length.

The detailed procedures are shown below:

1. Clean the $SrTiO_3$ in sequence with acetone, isopropanol, and deionized water in ultrasonic bath.

2. Spin-coat a layer of photoresist s1813. Expose it under mask alighner for 40s. Develop with MF319 for 90 s.

3. Argon-ion mill the sample for 60 s (900 V accelerating potential, 0.5 mA/cm^2 beam current).

4. Wash away the photoresist layer. Repeat procedure 2. Carefully align the contact mask pattern with ion-milled shape.

5. Thermally evaporate titanium (15 nm) and gold (70 nm).

6. Wash away the photoresist layer to lift off the metal on top of the photoresist.

7. Clean the surface with acetone, isopropanol, and oxygen plasma (15 s).

8. Wire-bond the finished $SrTiO_3$ sample to a chip carrier except for the gate pad. Use epoxy to bond a Au wire to the gate pad instead.

9. To test the electrical connections, the resistance has to be measured below room temperature ($\sim$ 250 K) while being gated by ionic liquid.

Following the list above, a device as shown in Fig. 7.5 can be achieved. The gate pad was connected to the LCC chip carrier by applying silver epoxy to the end of an Au bond wire as the Al_2O_{3-x} insulating layer beneath is very thin and cannot baear the pressure from the bonder. To well control the epoxy for the gate-pad bonding, a method used for positioning an ionic-liquid droplet on the channel was employed, which will be introduced in the next section.

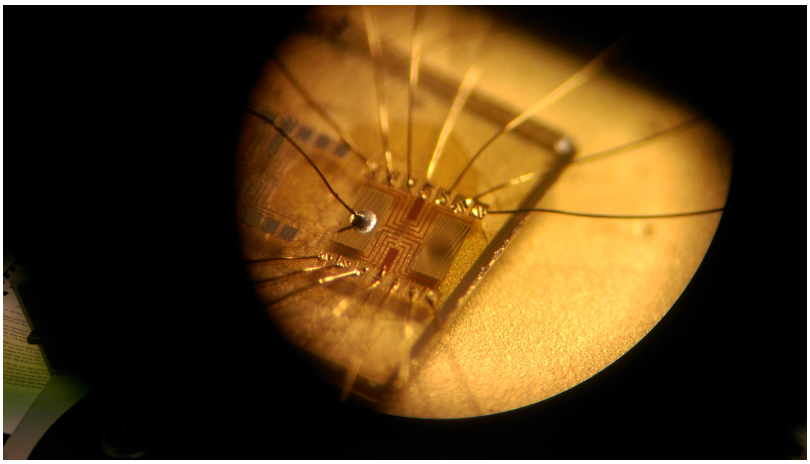

Fig. 7.5 Completed $SrTiO_3$ device for ionic-liquid gating experiments taken from optical microscope.

Because I changed the group and the supervisor, and no agreement were reached about the Sr_2IrO_4 experiments, I did not go any further and did no more attempts on Sr_2IrO_4 and $SrTiO_3$ were done to solve the problems presented above.

7.2 Measurements of Ionic-Liquid Gated $SrTiO_3$ Devices

The ionic liquid used for gating $SrTiO_3$ is DEME-TFSI (Diethylmethyl (2-methoxyethyl) ammonium bis (trifluoromethylsulfonyl) imide) bought from Sigma-Aldrich [81]. DEME-TFSI has a wide electrochemical window (EW) up to 3.5 V at room temperature. Staying at below room temperature, an even wider EW can be obtained. The ionic-liquid gating experiments were all conducted well below 0°C and the bias voltage applied to the ionic liquid belowas w 250 K. All the transport measurements have been repeated through several temperature cycles to confirm that the quality of the ionic liquid used, and the gated samples are still in their original states.

Before starting the measurement of an ionic liquid gated $SrTiO_3$ device, the DEME-TFSI was baked in a vacuum oven for more than 12 hours to completely remove any water content. Water may cause irreversible chemical reaction of ionic liquid, which is not desirable in the gating experiment. Most of the time the DEME-TFSI was stored in a desiccator to avoid water in the air, but the baking in vacuum is still necessary.

To drop a suitable size of ionic-liquid droplet onto the device to cover the whole gated channel without touching the exposed contact pads, several stratigies were tried. The size of the gated channel is 500×50 μm^2, which is too small to use a pipette even with a 1 μL pipette tip. Normally it causes lead to a large amount of uncontrolled liquid covering the whole

device including the bonded Au wire and this leads to short. After much practice and many unsuccessful attempts, the pipette method was abandoned. It was also found that manually controlling a pipette to put a liquid drop on a specified site as small as few millimeters across could be disastrous and ineffective. A slight hand shake may result in the pipette hitting the fabricated device and destroying it. Naturally a replacement I came up with a solution to the problems mentioned above at aking advantage of a micro-manipulator used for handling tiny objects under an optical microscope, a sharpened toothpick was fitted into a movable arm to drop ionic liquid onto the device. The tip of the sharpened toothpick not only needs to be big enough to hold ionic liquid, but also small enough to just cover the gated channel. This requirement is not difficult to meet. However, in practice the ionic liquid does not form a small liquid ball on the tip of the toothpick. It tends to move upwards because of surface tension, which makes it hard to flow ionic liquid onto the device. Some liquid is able to stay on the device surface, but it takes multiple times touching the device surface with the toothpick to leave enough ionic liquid. The other disadvantage is that these multiple touches often allowed the liquid to flow to some bonded Au wire, which is something we want to avoid.

To overcome these issues, the idea of dropping ionic liquid with the help of the ball bonder came to mind. The Au wire with a spark-generated ball on its end is used for bonding to metal. The diameter of the Au ball is normally 50 μm for 15 μm Au wire, which is the size used in our cleanroom. Due to the spherical shape of the end, more liquid will tend to stay around it instead of moving upwards or flowing down. 50 μm is slightly smaller than the size of the gated channel, which makes it perfect for our purpose. Besides, the optical microscope and the mechanical arm equipped with ball bonder provide a smooth and precisely designed control. After a few trials, the ionic liquid can be put down on the surface of device in a single attempt.

To measure a fully gated device, the charging process has to be completed when the ionic liquid is in its liquid state, that is above its freezing point. For DEME-TFSI, the freezing point is at around 230 K. Thus in the cooling down process, the temperature withheld at around 250 K to wait for the graduate charging of the ionic liquid. The source-drain bias V_{SD} applied through the channel was 0.1 V and was held constant. Gradually increaseing the gate bias V_G from 0 V to 3.0 V using a Keithley 2400 source-measurement unit (SMU), a leakage current was observed through the ionic liquid. This leakage current should be kept low below 1 nA by controlling the temperature, not inreasing the voltage until the temperature is low enough for the leakage to be below the allowed maximum. When the $SrTiO_3$ channel switches on, the gate voltage is large enough and the liquid has charged up, the source-drain current I_{SD} increases quickly to a few nano amperes. The whole charging process takes around 4 to 5

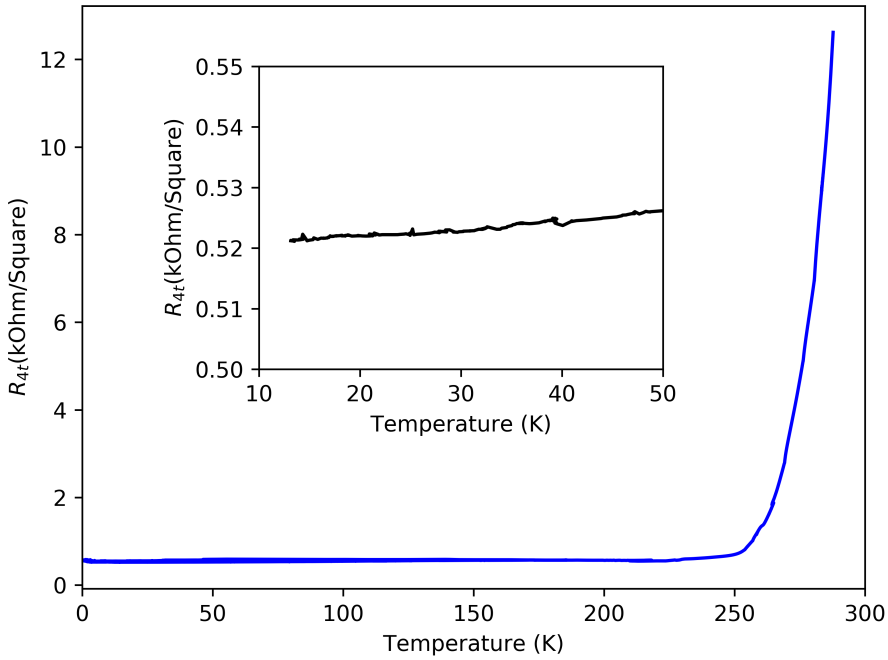

Fig. 7.6 The sheet resistance of $SrTiO_3$ as a function of temperature when the applied gate voltage was 3 V. The inset is a zoomed-in plot from around 10 K to 50 K to show clearly the residual four-terminal resistance of $SrTiO_3$.

hours to complete. Following the charging, the device can be cooled down further for the resistance measurement.

Fig. 7.6 shows the resulting resistance as a function of temperature. This measurement was conducted in a 4 K dip probe station, in which the probe was inserted directly into a helium dewar and manually moved down to the cool it gradually until the liquid helium (at 4.2 K) is reached. The vertical axis on the graph is the four-probe sheet resistance calculated from the dimension of the gated channel. It can be observed that from 270 K to 4.2 K the resistance drops quickly to 500 Ω/square with gate bias 3.0 V. This is consistent with the published result [79] which confirms the effectiveness of our device.

Chapter 8

Introduction to Self-assembled Quantum-Dot Device

8.1 Quantum-Dots and Coulomb Blockade

Small solid state devices with quantum dots have been receiving attention over decades for their prospect in industrial applications such as qubits to be used in quantum computer. This type of device is usually made of quantum dot structure consisting of drain, source, and quantum dot in the middle, as shown in Fig. 8.1.

A quantum dot is a quasi zero dimensional semiconducting structure in which electrons are confined in all three dimensions. Applying quantum mechanics to this case will lead to a series of discrete energy levels. In transport experiments, it is usually realised by lithography to fabricate two metal contacts acting as source and drain around a electronically isolated metal/semiconducting island. If an extra gate metal gate is also fabricated next to the island, it can be used to tune the energy levels on the dot. Due to the resemblance of the energy levels on a quantum dot and a single atom, quantum dots are referred to "artificial atom". When a sufficient bias is applied, the average number of electrons in the dot changes one by one. For this reason, a quantum dot device has another name of single-electron transistor. External bias will create an energy difference between the electrochemical potential of the dot occupied by electrons and that of the metal contacts, thus resulting in a finite conductance. Fig. 8.2 shows a schematic of electron tunneling through quantum dot.

The total energy of the electrons confined on a quantum dot can be expressed as

$$U(N) = \sum_{i=1}^{N} E_i + \frac{(-eN + C_g V_g)^2}{2C}, \tag{8.1}$$

where E_i is the single particle energy of the ith state, C_g is the capacitance between the quantum dot and the gate contact, V_g is the gate bias, C is the total capacitance, and N is the number of electrons on the quantum dot. The potential energy cost to add one more electron to the quantum dot with N electrons is

$$\mu_d(N+1) = U(N+1) - U(N) = E_N + \frac{(N-1/2)e^2}{C} - e\frac{C_g}{C}V_g. \tag{8.2}$$

Therefore, the chemical energy change when one electron is increased by one is

$$\mu_d(N+1) - \mu_d(N) = E_{N+1} - E_N + \frac{e^2}{C}, \tag{8.3}$$

as is shown in Fig. 8.2. This charging energy has to be overcome before an electron can pass through the barriers of the quantumm dot.

When the energy levels of both metal contacts are higher than the top energy level of quantum dot, the conductance will be zero behaving as a plateau as a function of bias. This is exactly the famous Coulomb blockade. In other word, Coulomb blockade theory is a theory describing the periodic conductance oscillations as a function of the applied gate voltage as a result of sequential single-electron tunnelling through a nanogap between two junctions [82–85]. The gate contact here can be used to raise or reduce the energy levels of quantum dot to let electrons flowing in or out of it.

The first Coulomb blockade oscillation was observed in a metallic quantum dot device [86]. The electronic states on the quantum dot are taken ad continuous because that it is a metal. The theory based on this was developed by Shekhter and Kulik which is called classical theory of Coulomb blockade. When the blockade is lifted, a few energy levels are actually filled. While in semiconductor quantum dots cases which were discovered later, the energy space between neighboring energy levels are so large that a single electron can be controlled to jump on and off the quantum dot. This type of Coulomb blockade is referred as quantum Coulomb blockade.

The Fig. 8.2 gives a more physical way to picture the electron transport involved.

Scientists and engineers are particularly interested in this phenomenon because of its realisation of controling single electron. This character implies the potential of quantum dot device to be made into even smaller size than those used in the current computer. To step further to mass production for industry, we need to find a way to obtain device consistently and easily. Among all the possible solutions, self-assembly (SA) device stands out as it is extremely to realise just by immersing substrate into the solution with nanocrystal for a period of time.

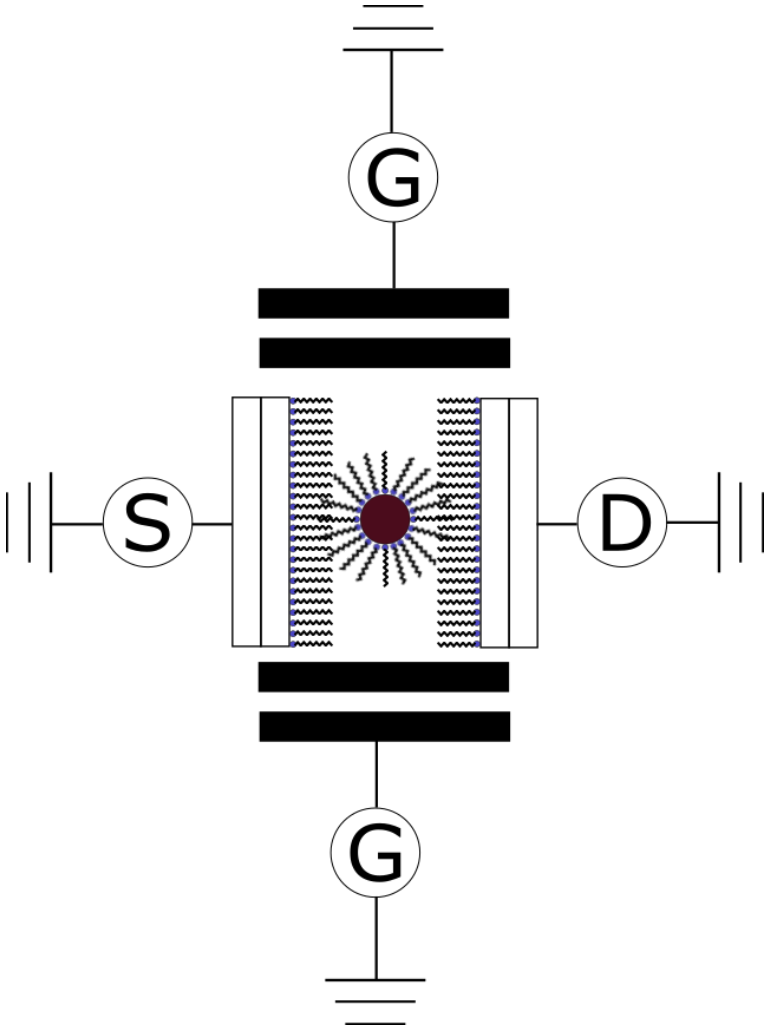

Fig. 8.1 Schematic of self-assembled quantum dot in an electrical circuit. The letters S, D, and G represent source, drain, and gate, respectively. The ligands attached to the contacts on the two sides are responsibile for anchoring the nanocrystal in the middle, and they provide a tunnel barrier to current flow through the dot. Ideally, we want only one nanocrystal to be assembled in the nanogap between the two contacts.

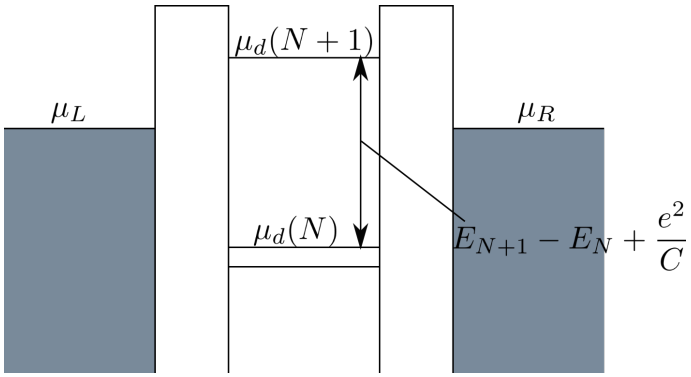

(a) On resonance

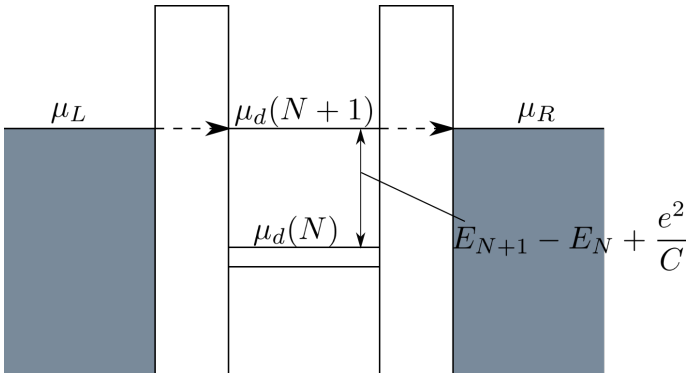

(b) Off resonance

Fig. 8.2 Schematic of the energy band diagram of a quantum-dot device. (a) Without any applied bias, the electrons are trapped in the potential well. The conductance is zero as no current can flow through the quantum dot. The electrons inside the quantum well have to overcome the energy gap between (*N*+1)th and *N*the energy levels. This is called Coulomb blockade. (b) Electrons can tunnel through the barriers on two sides and the conductance is finite when an energy level of the quantum well is lined between the chemical potentials of the left and the right metal contacts.

SA device is a type of spontaneously formed molecules on surfaces by absorption and are self-organized into crystallined structure. Their sizes can be as small as few nanometers, which dramatically expands the operation range of quantum electroncs and improves the corresponding operation time. This is going much futher beyond the conventional lithography. What's more, the size of nanocrystals used can be adjusted conveniently by chemical method. Adjusting the size of nanocrystal is actually adjusting the link between the semiconducting island and the metal electrodes around and is no doubt an essential parameter in the formed electric circuit. The other advantage of SA device is that numerous variation of composition cna be explored to synthesise new compounds acting as the semicondcuting islands providing more opportunities to discover better materials for quantum electronics. The fabrication process is as simple as immersing a chip into diluted nanocrystal solution for few hours before it is homogeneously covered. The Fig. [87] gives a typical trace of the nanocrystals moving and stacking onto the surface of the chip as a function of the time passing after the chip is dipped into the solution.

8.2 Studies of Lateral Quantum Dot Devices

Lateral quantum-dot devices can be built in a two-dimensional electron gas (2DEG) by patterning several metal contacts and gates on the surface. The most common example is devices built on a GaAs/AlGaAs hetero structure [88–90]. The 2DEG was confined by gates on the sides and gates producing tuneable tunnel barrier to the source & drain.

Such lateral quantum dots are fabricated using e-beam lithography to pattern metal gates around the dot. An alternative, possibly more successful, technique is to self-assemble a single nanocrystal in a nanometre-sized gap (nanogap).

A chemical method of assembling nanocrystals into the nano gap was to exploit three types of different linker molecules, that is ligands, to secure nanocrystals at the specific sites [91–95]. The idea is to attach nanocrystals to linker-molecules decorating Au contacts. This is the method adopted in this thesis to self-assemble nanocrystals to nanogaps.

8.3 Studies of Vertical Quantum Dot Devices

A different approach to quantum dot device is to have current flowing through a layer of large-band-gap material vertically as will be introduced in the next chapters. This also forms tunnel barriers. AlGaAs is a wide-band-gap semicondcutor which can realise this aim. The electrons are confined automatically in plane as a pillar structure is etched with the barrier layer exposed. The main challenge of the vertical structure is how to fabricate ohmic contact

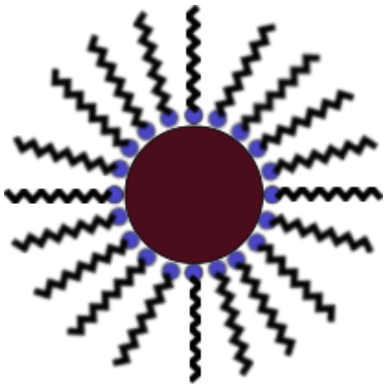

Fig. 8.3 A typical nanocrystal encapsulated by organic ligands. With various lengths of carbon chains of ligands, a series of self-assembled ligands can be produced with different ability to attach nanocrystals.

on the top layer in practice. The required ohmic contact has to form a low enough ohmic resistance and does not go too deep to spike throught the barrier layer beneath [83].

The simplest measurement for vertical quantum-dot device is the $I-V$ scan. Steps will be seen in the current as a signal of enhanced tunnelling as the topmost energy level of quantum dot moves into the energy window between the Fermi levels of the leads.

8.4 Nanocrystal Project in This Thesis

In the quantum-dot projects attempted in this thesis, we are focusing on the transport properties of PbS nanocrystal device in both vertical and lateral structures. The vertical structured quantum-dot device was fabricated based on a GaAs wafer with specific ligand design, while the lateral structured device was based on a SiO_2 substrate with gold electrodes forming nanogap. Nanocrystals of PbS were synthesed in the Optoelectrics group of the Cavendish Laboratory with around 5 nm diameter attachied to aleicacid-ligands to stop them clumping together. PbS nanocrystals are a type of lead chalcogenide quantum dot that are known to crystallise in the rock-salt structure. Normally the PbS nanocrystals hve a size-dependent energy gap[96] ranging from 0.41 eV to 2 eV as the nanocrystal size decreases[97].

Due to its exceptional electronic and optical properties in industrial applications, PbS has received a great amount of attention in the past years. Some approaches have been studied to engineer the composition or the structure of PbS to meet certain requirements in real applications [98–100]. Nanocrystals' transport sensitivity to the small change of bias also provides the possibility of producing high-resolution switches. Thus here we wish to

demonstrate the Coulomb diamonds obtained from the laterally fabricated nanogap devices with PbS acting as quantum dots. The bare fabricated nanogap devices on SiO_2/Si substrate were provided by Yutaka Majima's Group from the Department of Materials Science and Engineering, Tokyo Institute of Technology.

The vertical structured quantum dot project is a continuation of a previous nanocrystal SA project carried out by Qian Miao. The aim of the previous project was to demonstrate Coulomb steps and had the possibilities study the statistical relationship between the area of the contact and the electron tunnelling result. This was realised by fabricating a series of pillars with different sizes. In this process, all pillars were firstly etched down to expose the middle AlAs barrier layer. Then HF was employed to selectively etch into the AlAs layer to create a deep enough space for incorporating individual nanocrystal. In the actual experiments, the result of the measurement illustrated that a large number of nanocrystals were aggregated around the AlAs trenches and gave an exponentially rising, smooth tunnelling current, which means that it was not just single quantum dots being measured. A surprising observation was that there was no direct correlation between current, or success rate in achieving incorporation of nanocrystals, and the perimeter of the pillars, where one ould expect the number of independent nanocrystals to rise inproportion to the perimenter. Only the smallest pillars tended to work well. One guess for this phenomenon is that the top contacts covering the whole top on the pillars were attracting nanocrystals too much and left very few to assemble in the nanogap. One possible improvement is to isolate the the metal contacts on the top of the pillars with photoresist except for windows with specific sizes just before incorporating nanocrystals. The vertical quantum-dot project conducted in this thesis was designed with this improvement hoping to achieve some progress. The detailed mask design and the fabrication process will be presented in the next chapter.

Chapter 9

Quantum Dot: Experiments, Results, and Discussion

9.1 Fabrication of Quantum Dot Device and Self-Assembly Process

9.1.1 Vertical Structured Self-Assembled Quantum Dots

Laser Writer Technique

A laser writer technique was used in the fabrication process of the vertical structured quantum dot device. This is a type of maskless lithography which can realise UV exposure directly onto photoresist by using a single wavelength light source with pattern from the input graphic file. It is working similar to e-beam exposure scanning the wafer line by line, but with photon beam. Thus it is flexible to design whatever mask on software and to import it to the computer connected to laser writer. This is very cruicial and cost saving to early research when a final design of mask has not been settled. The resolution of laser writer can reach as small as sub-micrometre by choosing proper laser source. This technique is more likely to be used in laboratories and research institutes as the scanning time of large wafer for industrial application can be unbearably long (more than over night). A compromise decision between time cost and financial cost is normally needed with the consideration of the actual experimental requirement.

The laser writer system employed in the thesis is MicroWriter ML Baby from Durham Magneto Optics Ltd in Prof. Russell Cowburn's laboratory in the Thin Film Magnetism group, Cavendish Laboratory. This is a choice of two ultraviolet laser light sources emitting 385 mm or 405 mm, which have 1 μm resolution across the full writing area. There is

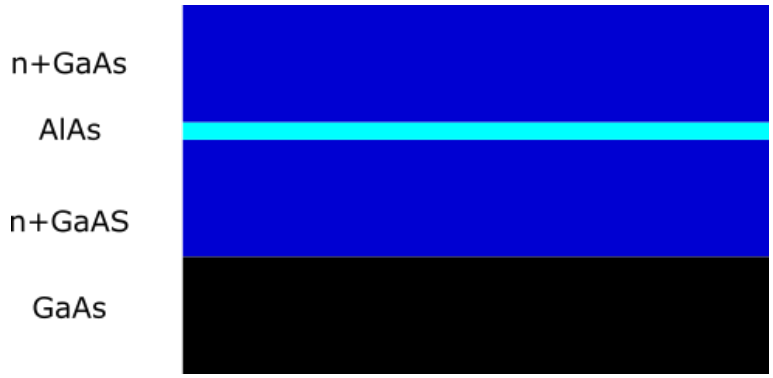

Fig. 9.1 Cross-section of GaAs wafer used for vertical quantum dot device. The substrate is pristine GaAs giving an insulating behaviour at low temperaure. Above it a 500 nm n+GaAs film was grown followed by 6 nm AlAs film as energy barrier, and a 300 nm n+GaAs cap on the top. All the layers were grown by the MBE team in the Semiconductor Physics Group in the Cavendish Laboratory, University of Cambridge.

an autofocus function which keeps the height of laser source locked with respect to the photoresist to ensure the beam remain in focus. Another three optical lenses are used to identify the position of wafer and move it simultaneously. Windows software with a user-friendly interface conducts all the functions mentioned above. The dose exposure can also be adjusted compensating for the disadvantage of single light source being scanned sequentially across the part of the chip to be patterned.

Fabrication Process and Problem Solving

The first prototype of the SA project is to use n+GaAs/AlAs/n+GaAs sandwich-structure wafer (Fig. 9.1) to construct a vertical SET. The middle layer of AlAs is etched away, to allow the nanocrystal to confineconfining semiconductor nanocrystal 5 nm PbS acting as quantum dot. The PbS nanocrystals are attached in the gap by octanethiol ligands. The schematic of a completed device is shown in Fig. 9.2. Due to the reason that AlAs is much less conducting than nanocrystal PbS at low temperature below $\sim$100 K, conduction will be through the tunnel barrier between the n+GaAs and PbS nanocrystal.

In Fig. 9.3, the fabrication process of a vertical quantum-dot device is shown. The full process recipe is given in App. 1. The wafer was first etched down to the bottom n+GaAs in order to put Pd/Ge ohmic contacts. Then the etch was applied again to expose the GaAs substrate except for the ohmic-contact region. After this step polyimide was put down to create an insulating layer for the final metal layer connecting the top ohmic contact and the GaAs substrate. The aim of this design is to prevent possible leakage from the side through the AlAs barrier. Following it the chip was dipped into buffered HF for 2 minutes, which

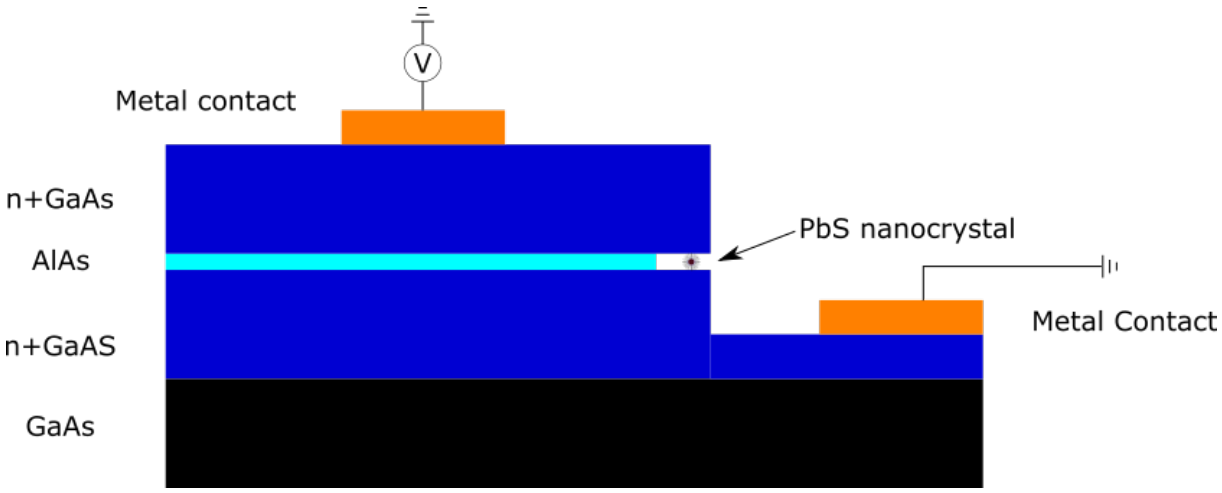

Fig. 9.2 Cross-section of the fabricated vertical structure. The yellow are metal contact which is usually annealed Pd/Ge. The middle layer of AlAs is insulating at low temperature avoiding the possible electric short from two n+GaAs layers. Part of AlAs can be selectively etched away by HF thus providing a space for accommodating nanocrystal.

will selectively remove the AlAs to a depth of about 200-500 nm into the wafer (reference Qian Miao). This leaves a gap just the right height for incorperating nanocrystals. To control the number of nanocrystals going into or around the gap, a layer of photoresist covers the whole chip, leaving only a narrow window opened just above the position targeted.

However, during the fabrication it was found that the AlAs layer is always more conducting at low temperature even down to liquid helium temperature (4.2 K). The wafer and the fabrication were then thoroughly inspected from all the possible perspectives and various methods were tested aiming to find out the problems. The possible sources of problems include the wet acid etch (the 1st step and the 3rd step), ohmic contact (the 2nd step), insulation layer (the 4th step), bonding step (the last step), and the wafer itself.

The possible problem of a wet acid etch is that the anisotropic etch rate of GaAs may cause the middle AlAs layer to be etched much faster than the top and the lower layer resulting in a short as shown in the schematic Fig. 9.4. The usual acid mixture is H_2O:H_2O_2:H_2SO_4 (ratio = 80:8:1) with an average etch rate of 8 nm/s for both GaAs and AlAs. The etch depth needs to be around 500 nm in order to expose the bottom n+GaAs layer, but not too deep so as to reach the GaAs substrate. Similarly, in the third step the contact pillars are necessary to be electrically separated from one another as well. Another 500 nm etch achieves this. However, it has the same risk of electrical shorts as described above. To carefully investigate this step, both alternatively selective etching and SEM examination were used. No sign of physical contact of the top and the bottom n+GaAs layer was observed.

To better control the acid etch direction and etch rate, an alternative acid etching was used to make sure that the middle AlAs layer was not etched deeper than necessary. Citric acid has the property of etching GaAs with a faster speed than it etches AlAs. Thus the strategy is firstly to etch away the initial 300 nm n+GaAs, and secondly to slowly etch away the part of the 6 nm AlAs layer exposed to acid which can be shown by measuring the GaAs etch rate every few seconds. After the etching, a metal contact was themally evaporated onto both the unetched top n+GaAs layer and the etched bottom n+GaAs layer for transport test later. The metal used are titanium and then gold. Generally these two metals will not form good ohmic contacts with GaAs. The reason for using them is to avoid the possiblility of ohmics spiking down to the bottom n+GaAs from the top. But they do contact enough to n+GaAs to detect strong leakage the AlAs barrier. The finished test devices were measured at room temperature as well as the liquid nitrogen temperature. Unfortunately, devices processed in this way gave similar leakage to that observed ealier.

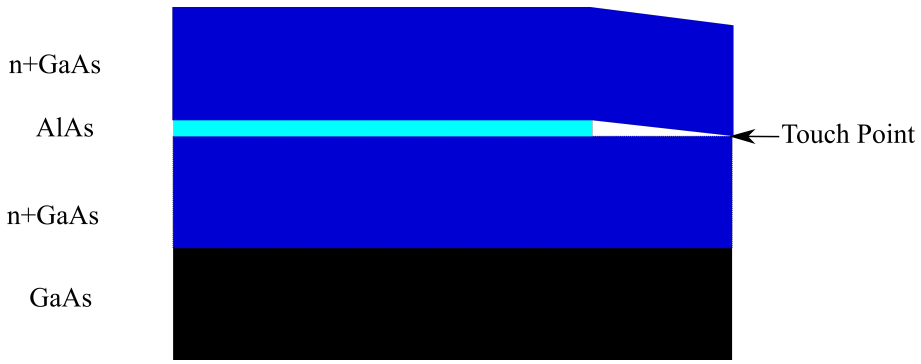

Fig. 9.4 Schematic of the possible problem with wet etch. The AlAs layer shown has been etched too much deep. The n+GaAs film above it hangs down because of its own weight and touches the bottom n+GaAl film causing electric short. This phenomenon was not observed in real fabrication.

As for the ohmic-contact problem, the main possibility suspected was that the annealing of Pd/Ge would form several metal spikes going through the midlle AlAs layer. This is a very common phenomenon for alloys like AuGiNe, which is often annealed to obtain good ohmic contact. However, the combination of palladium (Pd) and gemanium (Ge) is known for only forming a shallow ohmic contact on GaAs and it has been extensively studied. It has been confirmed that the maximum metal diffusion distance from the surface after annealing at 350 °C for 5 minutes will not be more than 200 nm, as long as the thickness ratio of Pd/Ge is kept above 1.2. This ratio is calculated from the atomic sizes of single Pd and Ge atoms aiming to match them 1:1 during annealing. The annealing recipe used to form an ohmic contact in this study is 350 °C for 5 minutes in forming gas of a mixture of nitrogen and hydrogen

with a ratio of 95:5 by volume. Before annealing Pd/Ge, the contact resistance between the contact on the top n+GaAs layer and the bottom n+GaAs layer is about 30 Ω at room temperature and few kiloohms at liquid-nitrogen temperature. Both resistances are far from satisfactory to the meet the high open-circuit resistance needed for observing nanocrystal Coulomb blockade (GΩ). A natural speculation is that some diffussion occurs during the annealing process. Thus, the annealed ohmic contacts were cleaved naturally and imaged in an SEM together with unannealed ohmic contacts and investigated carefully.

The latest FEI Helios NanoLab DualBeam microscope in the SEM suite, Cavendish Laboratory, University of Cambridge was used to capture high resolution SEM imaged. However, from the pictures of Pd/Ge ohmic contacts, spikes cannot be seen (Fig. 9.5 (a)). This is taken as sign that no real spikes from annealing occured, thus is not possibly the reason for electrical shorts.

To prove this point from a second perspective, we tested some metals which definitely do not form a ohmic contact to GaAs. One control experiment is to use a non-annealed Pd/Ge metal contact, and the other is to use a Ti/Au combination to test it. Fig. 9.5 (b) shows a SEM picture of the cross section of a unannealed Pd/Ge contact. The AlAs layer can be seen clearly. The two chips were patterned together, using the exactly same procedure to ensure the control of experimental conditions. Neither of the two devices was annealed. Instead, they were immediately tested after liftoff. The two devices gave almost the same contact resistances, roughly a few kiloOhms at room temperature and few megaohms at liquid nitrogen temperature. To further confirm this leakage, they were wedge bonded below 100 °C and retested at liquid helium temperature using a transport dewar. The resistances through the ohmic contacts on the two chips were not improved much, giving few megaohms at low bias. Even though there is a large contact ressitance, the expected resistance should be much higher still. In conclusion, the Pd/Ge ohmic contact itself is not the source of problem.

The insulation layer at the fourth step might be another source of leakage. In the experimental design, a layer of polyimide used to prevent electrical leakage from the top n+GaAs layer to the bottom n+GaAs layer through the metal lead to the bond pad, as shown in Fig. 9.5. The polyimide we used is a photodefinable polyimide HD-4014 with thinner T-9039 (Proylene Glycol Monomethyl Ether; N-Methyl-2-Pyrrolidone). Both products are produced by HD MicroSysems^{TM}. The suggested curing temperature on the data sheet is 375 °C for 1 hour in a nitrogen atmosphere. However, because 375 °C is higher than the Pd/Ge annealing temperature, and Pd/Ge might diffuse, we changed the curing method to using a long UV exposure time (200 s) instead trying to stabilise the polyimide enabling a good insulating property. The polyimide cured by this method has been proved to be resistive to chemicals like acetone and isoproparnol-2. Confirm again that the cured polyimide layer

is indeed a good insulator, a test chip was fabricated by photolithography with the simplest structure of two gold films sandwiching a layer of $\sim$0.7 μm cured polyimide HD-4104 and electrically tested at room temperature at a probe station. Applying up to 3 V was not able to break down the polyimide layer, and 3 V is much higher than the bias voltage used to test the complete nanocrystal chips. Leakage can depend on whether it goes over a step. But at the foot of the pillar the polyimide should be even thicker, and at the type of the pillar leakage does not matter Based on this result, it is concluded that polyimide should not the problem.

The last possibility is that the bonding somehow creates an electrical spark, breaking down the finished devices. A simple way of testing this is not to bond, but to probe the contacts directly using the sharp tips of a probe station to form point contacts. In this way the danger of sparking will be avoided. Unfortunately from the probe-station tests, electrical leakage was also observed.

We noted that the developer of photoresist, MF319, also etches the AlAs layer quickly. Thus the developer was switched to AZ generic developer with a much slower Al etch rate in case of AlAs damage and causing a point contact between the top n+GaAs layer and the bottom n+GaAs layer leading to leakage.

With the tests described above, it was a reasonable guess that the wafer itself are the cause the leakage. 6 nm AlAs is an extremely thin layer and may have some doped atoms inside, diffusing from the heavily electron-doped upper or lower layer. To avoid this possibility, we designed a new wafer adding two 10 nm undoped GaAs barriers on the two sides of the central AlAs layer. Fig. 9.6 illustrates two band diagrams before and after adding the GaAs barrier layers calculated using the free 1D Poisson-Schr*ö*dinger solver. It can be observed that with increasing the thickness of the GaAs, a small but wider dome appears in the conduction band around the central AlAs barrier, which creates some difficulty for electrons to tunnel. The thickness of the undoped GaAs should not be too thick to prevent electrons tunnelling through the AlAs barrier. The software ([101]) used for the design is nextnano with University license, a semiconductor nanodevice simulation tool.

With the new grown GaAs wafer, all the tests done on the old wafer W136 were repeated. However, no significant improvement was observed.

Eliminating all the possible sources of problems from fabrication, there is still one likelihood that it is the wafer itself. For the moment, there is no feasible method to detect the quality of the middle AlAs layer. Alternatively, buying a commercially made wafer from a company or other university could be worth trying. However, in the previous study, Qian Miao used 4 different wafers and never had this leakage problem, though the processing recipe was the same. His leakage current considerably small ($\sim$ 1pA at 1 V).

9.1.2 Lateral Structured Self-Assembled Quantum Dots

Having found no way of making the vertical structure work, I looked at the lithographically defined nanogaps kindly proposed by Yutaka Majima's group. These consists of e-beam defined metal wires with a 10 nm nanogap left in them on a SiO_2/Si substrates. The gold was then electroplated (an electroless technique) to reduce the width of the gap to a few nanometres. Electrodeposition is a film growth process which using electric current to reduce a target metal from one electrode and to coat the destination surface immersed in the same electrolyte. Unlike conventional metal evaporation and sputter deposition, also called a top-down technique, electrodeposition is typically a bottom-up technique. Although both are applied widely in the nano-technology industry, the bottom-up technique shows a major advantage in creating high-purity and ultra-small structures. However, the final gap size is still variable, as the original gap size had width fluctuation of few nanometres. The design for our lateral quantum dots requires a nanogap ranging from 3 nm to 10 nm, which is extremely challenging for a top-down technique, even with electron-beam lithography. Fig. 9.7 shows a typical nanogap in our batch of devices. In electrodeposition, the thickness of the deposited metal can be well controlled by the time duration of the deposition on the substrate. Normally the longer the substrate stays in the electrolyte, the thicker the deposited metal is. This technique can also be used in developing biomedical applications if polymers and biomaterials are exploited.

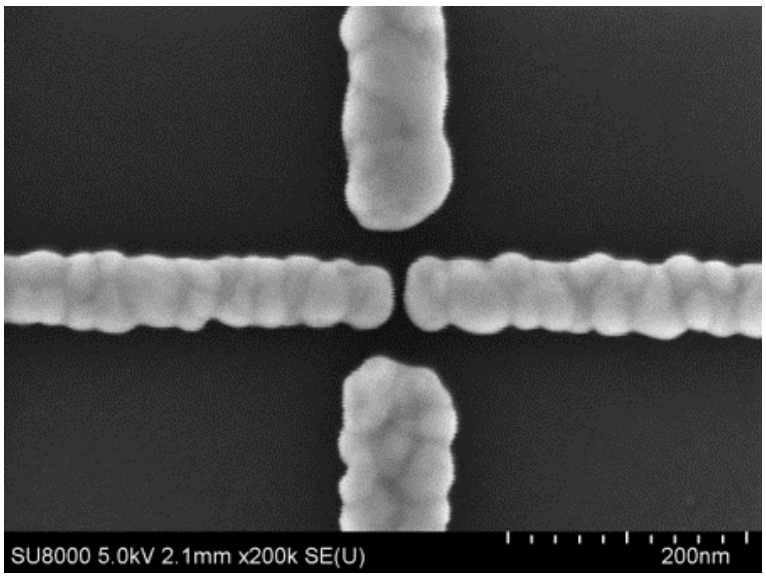

Fig. 9.7 SEM photo of a nanogap fabricated by electrodeposition by Yutaka Majima's group. The nanogap size in this photo is roughly 7 nm or smaller. A nanogap as small as this is very difficult to fabricate using a top-down technique.

In our 10×10 mm^2 chip, there are 80 devices each with a source, a drain, and two gates forming a cross layout. One source is shared with another drain. After fabrication, all the devices have been checked by Yutaka Majima's group under SEM to label the successful ones. The yield of the fabrication and the assembly was about 20 %. An optical photo in Fig. 9.8 shows part of the design of chip.

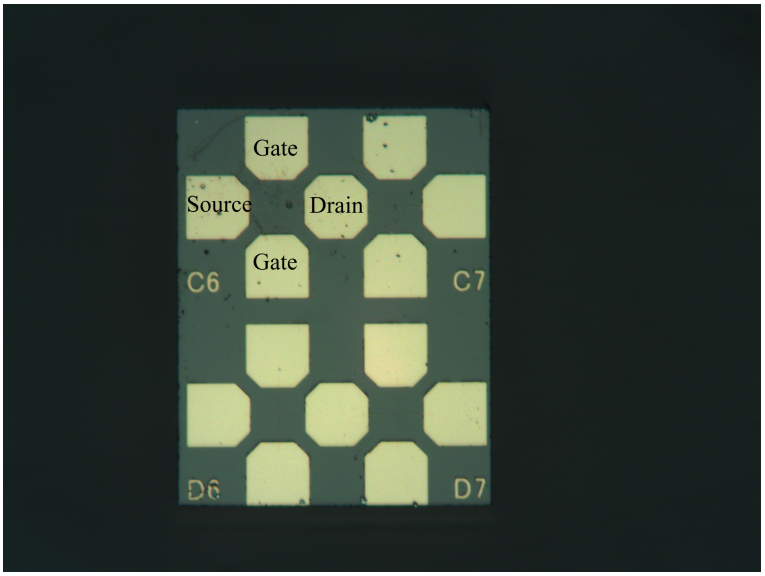

Fig. 9.8 Optical photo of devices C6, C7, D6, and D7 cut from the full chip with 80 devices. As labelled on device C6, the top and bottom Au contacts are gate pads. The source and drain contacts are aligned horizontally. C6 and C7 share a common source/drain contact. All measurements were conducted in the cryogenic probe station in the Hitachi Laboratory attached to the Cavendish Laboratory. The metals were mechanically contacted by tungsten tips. By observing the movement of the tips, it can be ensured that the contacts are well connected.

There are three steps of the nanocrystal assembly process. Firstly, the whole chip was immersed into 1 mM hexanethiol [$CH_3(CH_5)SH$, C6S] solution in toluene for 24 h to firstly form a self-assembled monolayer (SAM) C6S. The chip was then taken out, rinsed twice with toluene, and dried with flowing argon. Then the chip was immersed in 1 mM octanedithiol [$HS(CH_2)_8SH$, C8S2] solution for 24 h. After the first two steps, a layer of C8S2/C6S monolayer was obtained with a sparse array of C8S2 separately supported by the SAM of C6S. The C6S had no top S thiol group so only the C8S2 could bind to the nanocrystals, providing a spare array of nanocrystals. Lastly, the chip was rinsed in toluene and dried with flowing nitrogen again and dipped into 1 mM PbS nanocrystal solution with decanethiol [$CH_3(CH_3)SH$, C10S] as ligand for 24 h. All the procedures above were carried out in a

nitrogen-filled glovebox. Before taking the chip out of the glovebox, the chip was rinsed twice in toluene and dried with flowing nitrogen.

Two pieces of substrate with thermally evaporated gold film was tested before the actual assembly to test the whole assembly process. After completing the process, the gold films were scanned using SEM to confirm the homogeneous distribution of the nanocrystal layer as shown in Fig. 9.9.

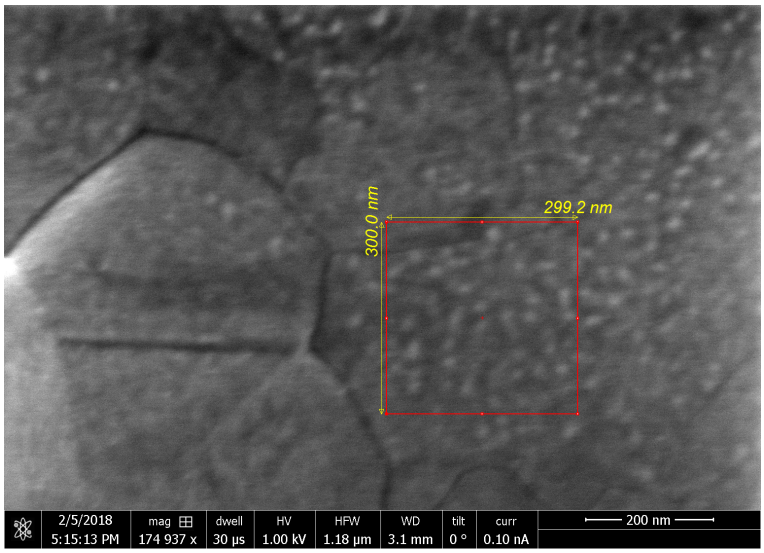

Fig. 9.9 SEM photo of self-assembled PbS nanocrystals attached with ligand octanedithiol on gold film. The red square box is about 300×300 nm^2 large in area. There are roughly 100 PbS nanocrystals inside the red box.

The original ligand used to form a shell to protect the PbS nanocrystal is oleic acid. In our experiment, in order to attach of PbS nanocrystal to the molecules C8S2 chain oleric acid ligands were exchanged for C10S. Ligand exchange is a well-developed process in nanocrystal research [102]. We followed the standard procedure in doing this. The detailed process can be found in Appex 1.

9.2 Instrument Setup and Measurement for Lateral Quantum Dot Device

9.2.1 Probe Station for Measurement

The equipment used for transport measurements of quantum-dot devices was a cryogenic probe station provided by the Hitachi Laboratory attached to the Cavendish Laboratory,

University of Cambridge. It is a dry cryogenic system installed with six probe arms for making mechanical contact with sample. The tips of the arms are tiny and sharp enough to put onto contact pads in our experiments. On the top of the sample chamber, there is an optical window as shown in Fig. 9.10 (b) for inspecting sample's condition and the movement of the contacting arms. For each arm, three directions along x, y, and z can be adjusted within a limited range. At the bottom of the sample chamber, similar to the cryogenic system in the previous section, is placed a cold head responsible for cooling. The base temperature of this system is about 25 K. Two thermometers were used for monitoring the system's temperature, one of which, on the sample stage, is with a heater for temperature controlling (25 K - 300 K), while the other one is for the cold head. A two-stage turbo pump accompanies the probe station. At the base temperaure, the chamber pressure can be as low as 1×10^{-5} mbar, or even lower with longer pumping time.

The software for controlling the probe station, displaying and recording data is CryoMears written by Prof. Chris Ford. We adapted the driver for the instrument to work with the Agilent 4156B Semiconductor Parameter Analyser in the Hitachi Laboratory. There are four channels in total as source-measure units. In the actual measurement, one of the channels was taken as the common contact, that is the source, while the other three acted as the drain and two gates.

9.2.2 Experimental Measurement

All the $I-V$ characterisation of assembled quantum dot devices were carried out using the cryogenic probe station presented above. The devices were stored in the Optoelectronics Group's glovebox filled with nitrogen to maintain the quality of the devices. They were taken out just a few minutes before putting into the probe station. To minimize the exposure of the nanocrystals to the air, the devices were sealed with Parafilm M (a plastic paraffin film produced by Bemis NA for further seal) in a small sample container in the glovebox and then transferred to the Hitachi Laboratory.

For each device, at low temperature an external bias was applied across the nanogap and swept up and down. To test the repeatability of the I-V curve, the voltage was first swept up to a positive value, back to the corresponding negative value, and then back to zero, that is a sweep loop. Because we do not know exactly for each device what the highest safe voltage is, we kept increasing the maximum bias by a small voltage in each loop. Throughout the measurement, the devices stayed at 30 K without exposure to light.

In total, 6×4 devices were measured, in which 1×4 (one chip) was bare devices without assembled nanocrystals. Two of the chips were accidentally exposed to air for about 30 minutes due to a pump failure. The rest of three chips were assembled in two different

batches. The sweep rates used in the measurement were all below 6 V/h. All the detailed results and discussion will be presented in the next section.

9.3 Result and Analysis of Electric Transport Measurement of Quantum Dot PbS

9.3.1 Empty Devices

The empty nanogaps without any processing were measured first. The result is shown in Fig. 9.11. It can be observed that the open gap demonstrated roughly 1 GΩ resistance at 30 K. The bias voltage was taken up to 2 V and the nanogap still did not broken down. The Fig. 9.11 illustrates an meausurement from a bare device without any nanocrystal or linker molecules.

9.3.2 Number Density of PbS Nanocrystals on Gold Film

To optimise the nanocrystal assembly process to achieve the best chance of success, the controlled experiments of self-assembly on thermal evaporated gold films have been conducted. Several pieces of mica sheet were used as substrate. A thin layer of 20 nm gold film was thermally evaporated onto the mica sheets. They were subsequently annealed for 5 minutes to obtain a smooth morphology with small enough gold grains on the surface. The films were immersed into hexathiol (1 mg/ml), octanedithiol (1 mg/ml), and PbS nanocrystal solution (1 mM) with decanethiol ligand for a specific period of time. The immersion time for hexathiol and PbS nanocrystal solution are both 24 h, but for octanedithiol varied. To clarify the impact of the immersion time on the density of nanocrystals assembled on the film surface, I tried three different time lengths, i.e. 6 h, 12 h, and 24 h.

As demonstrated by the SEM image in Fig. 9.12, both films give similar amount of nanocrystal density which is about 100 counts for 300×300 nm^2 area. The immersion time does not seem to make a big difference. However, this count may not be accurate as we thought, because the resolution of the SEM photos is not good enough to resolve nanocrystals clearly. To be on the safe side, the period of 24 h was selected as the recipe used for the actual devices.

9.3.3 Measurements of Assembled Quantum-Dot Devices

In this section, all measured devices will be presented as well the possible explanations for the behaviour. Three batches of devices were measured in total, with the second batch

exposed in the air accidentally for about half an hour due to the failure of the pump on the probe station. Both the first and the third batches showed conducting behaviour while the devices in the second batch were completely open.

The second batch of assembled devices (E6, E7, F6, F7, A8, A9, B8, and B9) were firstly well sealed in the sample chamber of the probe station. However, the pump station of the probe station failed in the middle of pumping down and some air leaked in for about half an hour. Studies [103–105] have demonstrated that nanocrystals exposed to air for few minutes will oxidise rapidly. A substantial insulating layer will form at the surface of the nanocrystals leading to an increase of the energy gap and thick tunnel barrier. The $I-V$ characteristics from the second batch of our devices are consistent with this conclusion that the nanocrystals oxidised.

One of the commonly observed phenomena in semiconductor devices is random telegraph signals (RTS) [106, 107] or burst noise, which is especially clear in the $I-V$ curve of device C8 presented in Fig. 9.17, Fig. 9.18, and Fig. 9.19. RTS is a spectrum of random signal switching between two states (e.g. on and off) with time in semiconductor structures. It came from the idea that charges can be trapped and released, affecting the conduction in material electrostatically, and changing the trap's average occupancy with external bias. This was proposed by Stefan Machlup in 1953 [106]. In Fig. 9.17 the blue curve illustrates the most obvious on-off switching between zero and the original value, which looked like tunneling behaviour. For our case, the conducting material is presumably one or more PbS nanocrystals in the nanogap. It can be seen that more than two states exist actually because the switching is not happening between only two values. Each distinct $I-V$ characteristic current exponentially increasing curve can be considered as a state. (Ignoring the RTS, the curve is exponentially increasing with externally applied bias, which is repeatable with the back sweep shown in Fig. 9.18 and Fig. 9.19. This stable result can be explained by the reason that more than one nanocrystals were connecting the Au contacts and they have been stabilised around the gap.)

The existence of signals in two or more charge metastates is called multiple or complex RTS [108–110]. For our self-assembled nanocrystal devices, the position and the morphology of nanocrystal layer cannot be precisely controlled during the assembly process. As described in the previous chapter, nanocrystals are self-assembled with linker molecules on the substrate mechanically and chemically. Usually together with the homogeneously formed self-assembled layer, some defects are also possible with misalignment between nanocrystal ligands and linker molecules. Under external bias, the defects are more likely to be disturbed showing switch effect.

To have 4 states, only two nanocrystals are needed, or for 8 states, 3 nanocrystals are needed. So the number of conducting nanocrystals in the gap is likely to be as low as 2. There are actually only 4 states, which are accessed by a single switching event from the highest, so it is more likely that one nanocrystal can take more than one stable positions in the gap, each with different tunnel barrier widths, hence conductance. This is the phenomenon shown in Fig. 9.17.

The device C9 from the third batch of assembly shows a nearly symmetric jump at around 0.09 V (See Fig. 9.20). It might be caused by the excitation of electrons. However, from Fig. 9.21 with the same range of sweeping bias, it gives a higher current on the positive side than in the earlier sweeps shown in Fig. 9.20. One possibility explaining the difference is coming from the movement of a nanocrystal into the nanogap by the hugh electric field of the applied bias voltage.

A different behaviour otherwise has been observed in device D9, as shown in Fig. 9.22. Less difference from two successive sweep loops are illustrated compared with device C9. If we assume that more nanocrystals were accumulating around one metal contact in device D9 and could hardly be attracted or expelled by the electric field, the $I-V$ characteristics of D9 is possibly more stable than C9.

From the results presented above, a phenomenon that excessively aggregated nanocrystals were filled in or suspending around the nanogap between Au contacts seems to dominate most of the devices. Their exponentially increasing currents under externally applied bias are typical diode tunneling behaviour through a barrier. The current steps predicted for Coulomb blockade were not observed here.

Many junctions show conduction related to the presence of nanocrystals. Studying indicates the movement of object within the gaps, and some different characteristics (Fig. 9.17) can be explained by the movement of just one nanocrystal between different position in the gap, with no current in one configuration, so no other nanocrystals conducting in parallel. However, no Coulomb staircase is observed. This may be because the nanocrystals are too unstable, or in most cases, there are too many nanocrystals in a gap and the individual step become blurred out.

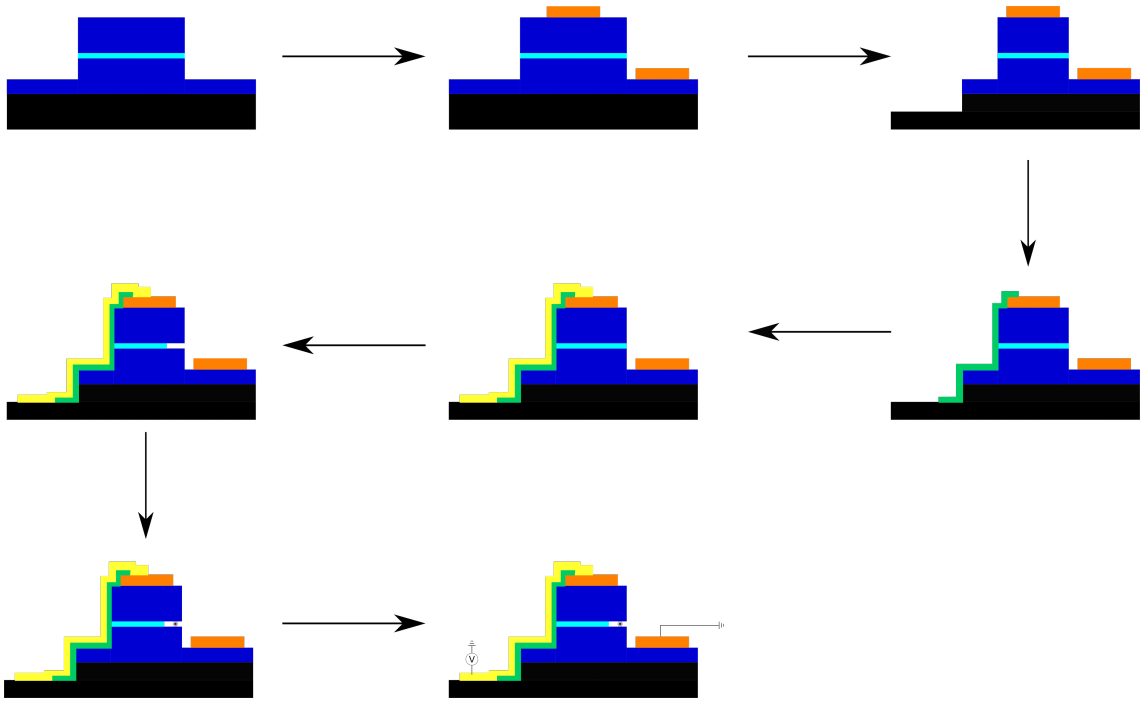

Fig. 9.3 Schematic of fabrication process of vertical quantum dot device.

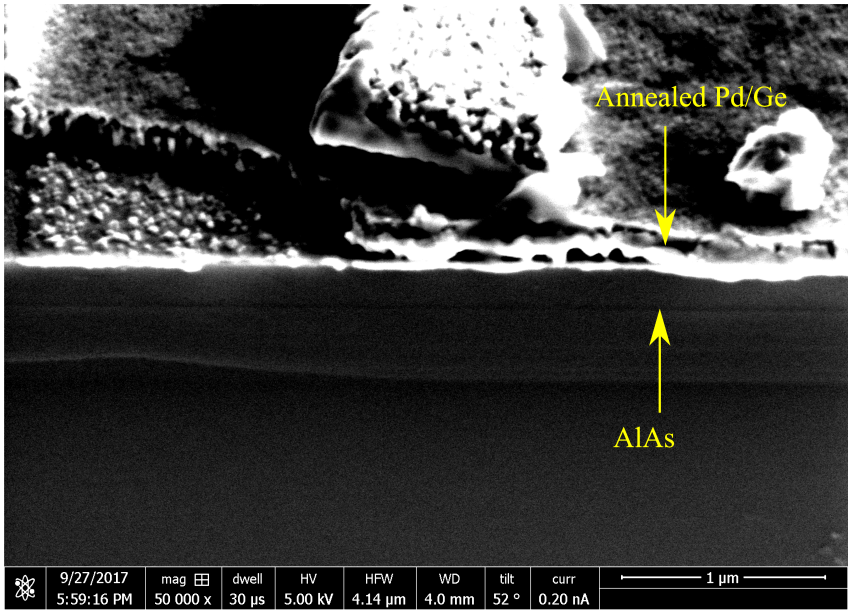

(a) Annealed Pd/Ge contact on GaAs.

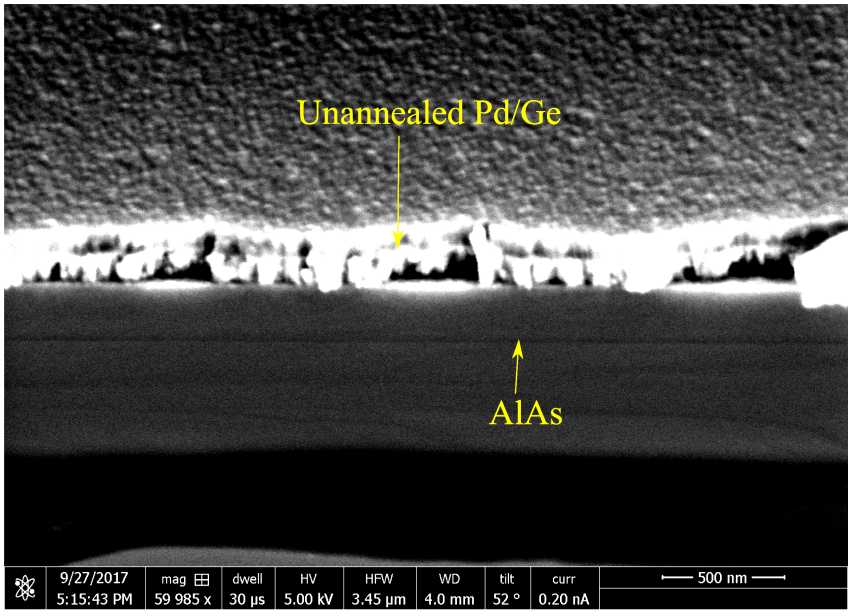

(b) Unannealed Pd/Ge contact on GaAs.

Fig. 9.5 (a) SEM photo of annealed Pd/Ge (b) SEM photo of unannealed Pd/Ge on naturally cleaved GaAs (W0136) pillars. The wall is very clean and no metal short can be spotted from the photo. There is no clear metal spike shown in (a). In (b) the top two layers of metal, Pd and Ge, were not annealed to ensure that no metal spikes are able to penetrate through the AlAs layer indicated by the lower arrow in the photo.

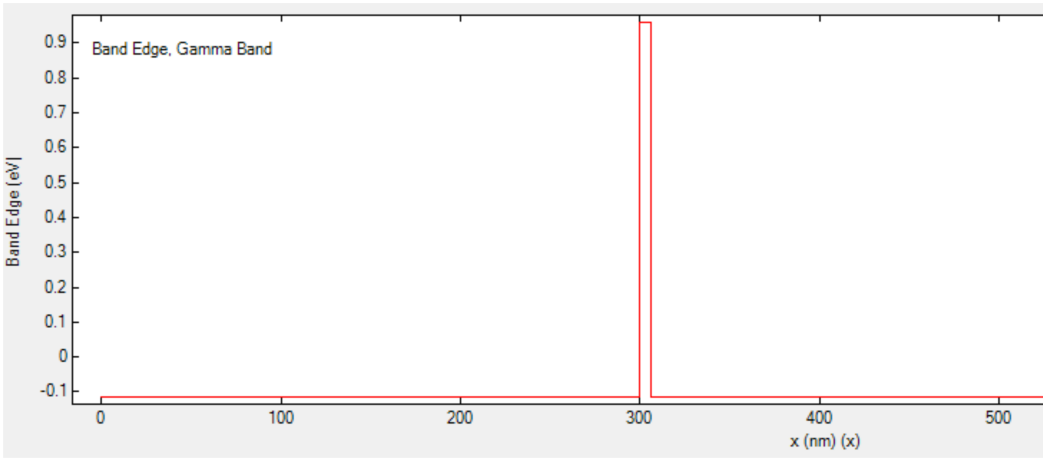

(a) Band diagram with the only central AlAs barrier, matching wafer W0136.

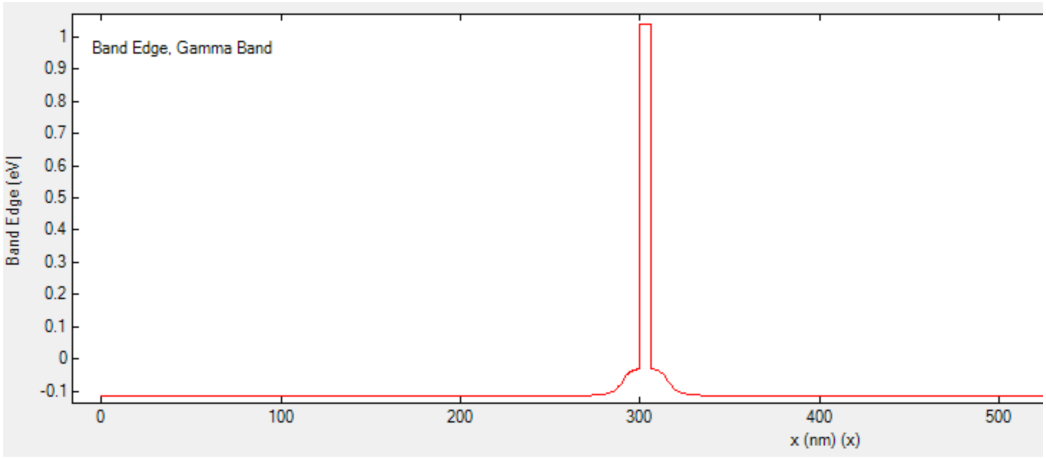

(b) Band diagram with 10 nm GaAs barrier added along the two sides of the AlAs,matching wafer V869.

Fig. 9.6 Simulated band diagram of GaAs wafers. The flat regions in two plots are heavily doped n-type GaAs with a dopant density of 10^{18} cm^{-3}. The central band barrier is from the 6 nm AlAs layer.

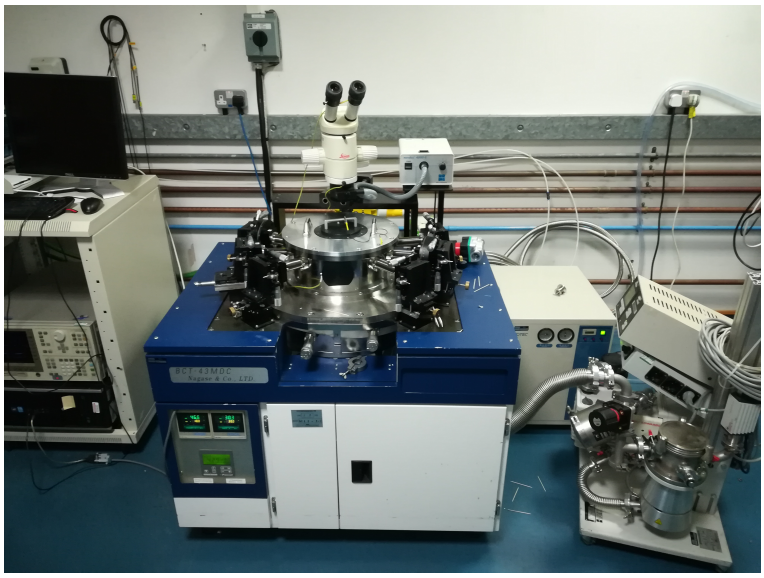

(a)

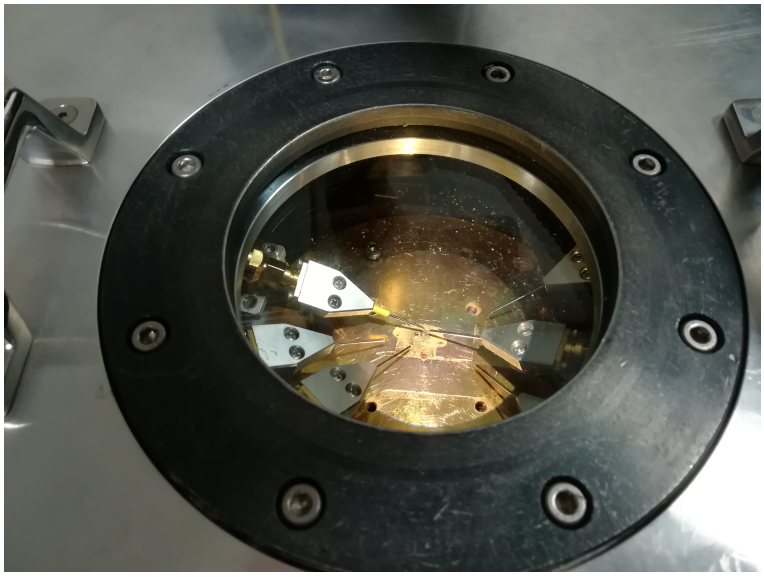

(b)

Fig. 9.10 Photos of the probe station in the Hitachi Laboratory used for quantum dot device measurement. (a) The whole system includes a pump station, compressor, and computer for control.

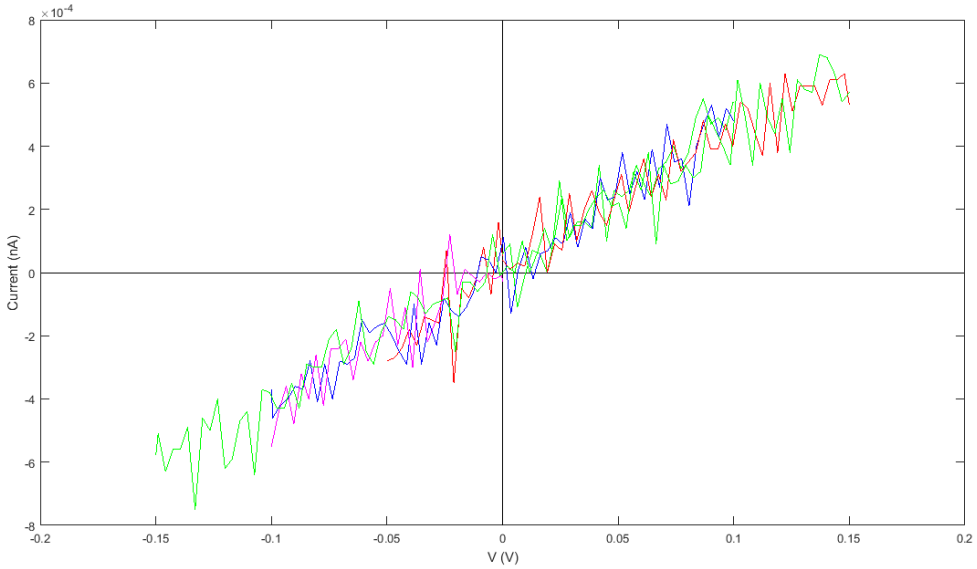

Fig. 9.11 $I-V$ characteristics through the nanogap of the bare device F9. The temperature was kept at 30 K. The measured device F9 was free from any nanocrystals and linker molecule thiols. The estimated resistance of the nanogap in this device is about 1.6×10^{10} Ω, which is taken as the reference for the more conducting devices with nanocrystals and thiols filled nanogaps.

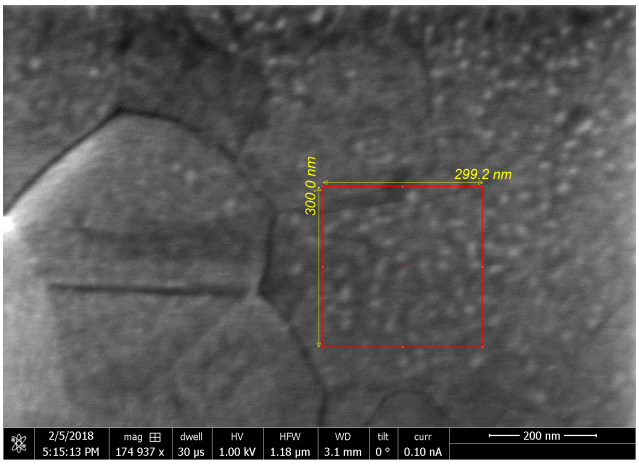

(a) SEM photo of gold film on mica plastic sheet with 6 h immersion time in octanedithiol for self-assembly process.

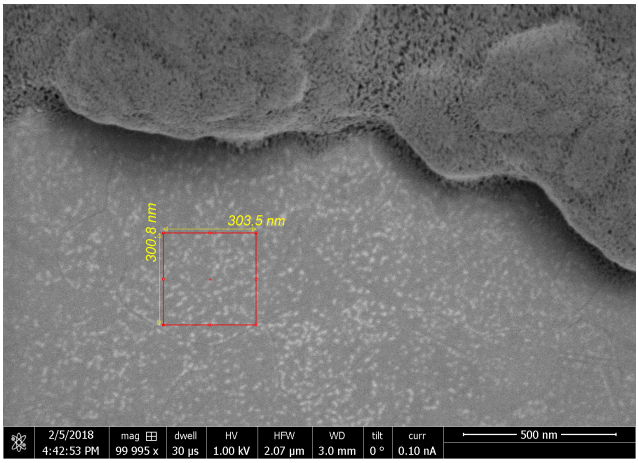

(b) SEM photo of gold film on mica plastic sheet with 24 h immersion time in octanedithiol for self-assembly process.

Fig. 9.12 Comparison of the nanocrystal number densities on the gold films that were immersed in 1 mM octandithiol for 6 h amd 24 h, respectively. The white dots on the photos are interpreted as being 5 nm PbS nanocrystals. Counting the nanocrystals, it seems that the number densities of nanocrystals assembled for 6 h and 24 h are alomost the same, about $11/\text{nm}^2$.

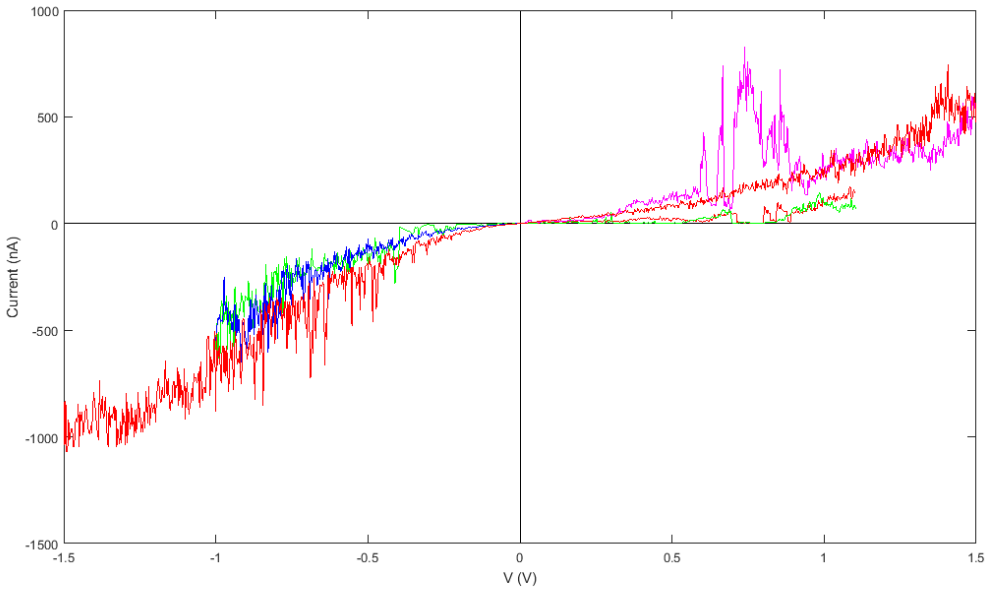

Fig. 9.13 Device G6 from the first batch nanocrystal. Two sweep loops were conducted as shown. The up sweep and the down sweep in the first loop over the smaller range, are roughly overlapping with one another, which indicates that the state of the device is repeatable and stable. However, when the bias voltage was swept to a higher voltage, an abrupt jump occurred which may have been caused by the movement of one or more nanocrystals into the nanogap. The change at negative bias was act as large as at positive bias.

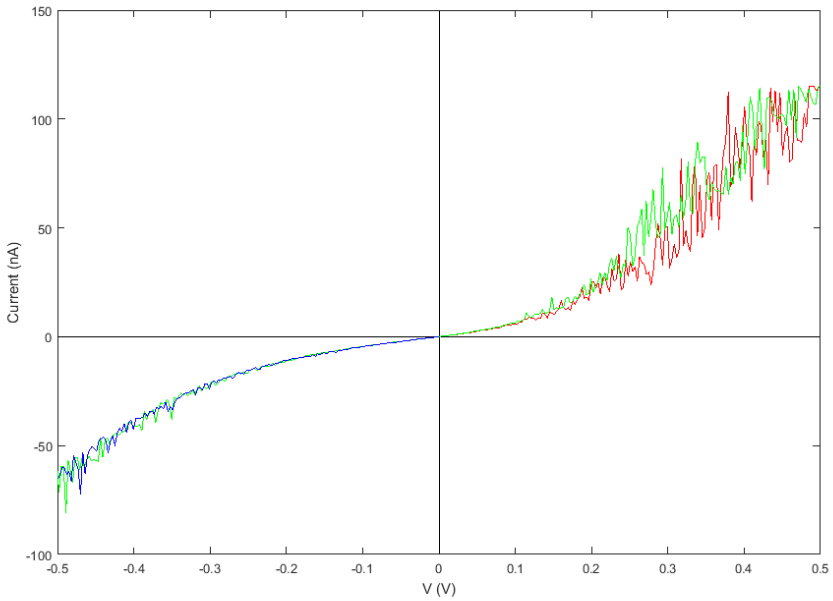

Fig. 9.14 Device G7 from the first batch nanocrystal. The bias voltage was swept between 0.5 V and -0.5 V. During the up sweep and the down sweep, the positive range gives a clearly larger random telegraph noise compared with that in the negative range. This level of the noise can be seen to be repeatable. The asymmetric $I-V$ characteristics may be caused by an asymmetric distribution of the thiols linking nanocrystals in the nanogap.

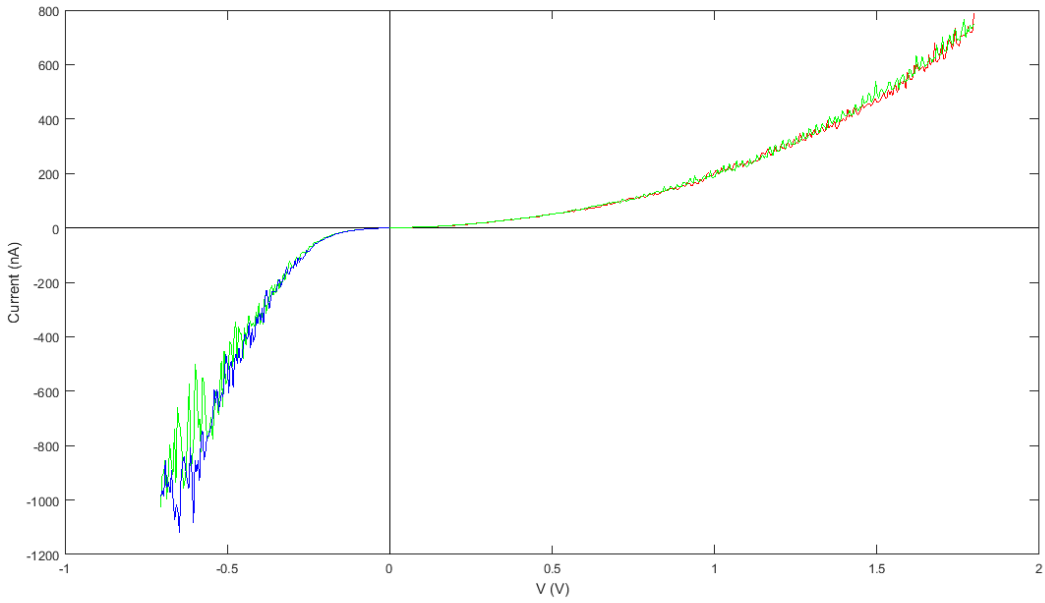

Fig. 9.15 Device H6 from the first batch of nanocrystal assembly. The exponential behaviour of the $I-V$ chracteristics indicates that multiple nanocrystals were linking the two Au contacts in the nanogap. Quantised Coulomb cannot be observed, and this may be because there are a number of dots attached in parallel, and steps in each occur at different voltages and blur out the overall characteristics.

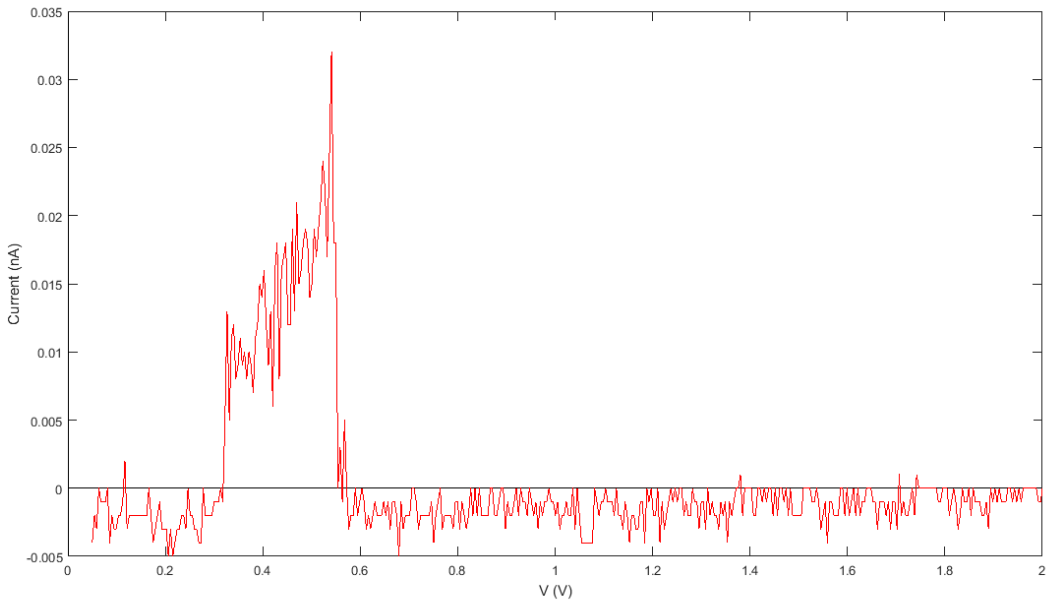

Fig. 9.16 Device H7 from the first batch of nanocrystal assembly. The nanogap is open in this case as the current through the nanogap is almost zero ven up to 2 V bias voltage. The abrupt rise and fall around 0.5 V may be caused by a sudden move of a nanocrystal into and out of the nanogap.

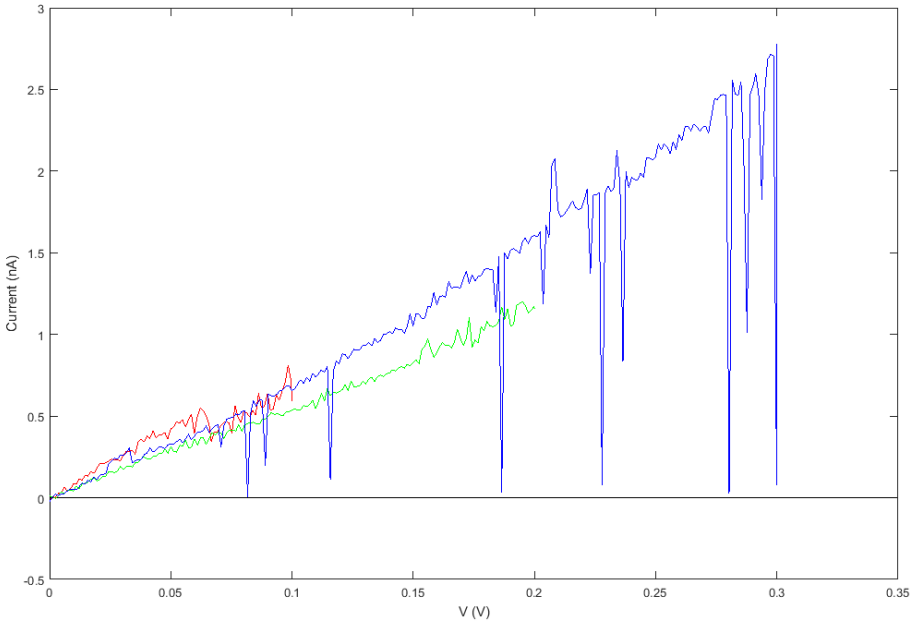

Fig. 9.17 Device C8 from the first batch of assembly. A random telegraph signal appears only on the sweep up to 0.3 V, while the other two sweeps give relatively smooth current.

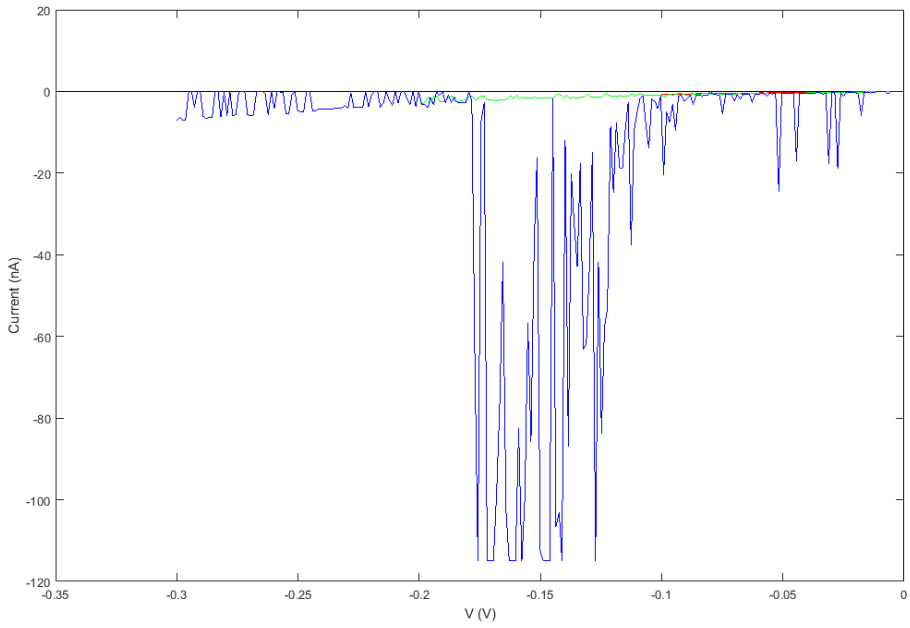

Fig. 9.18 Device C8 from the first batch of assembly. The blue curve is the last voltage sweep back to zero from -0.3 V. The drop of it at around -0.15 V might be caused by the change of state of nanocrystal by frequently stimulus of large voltage.

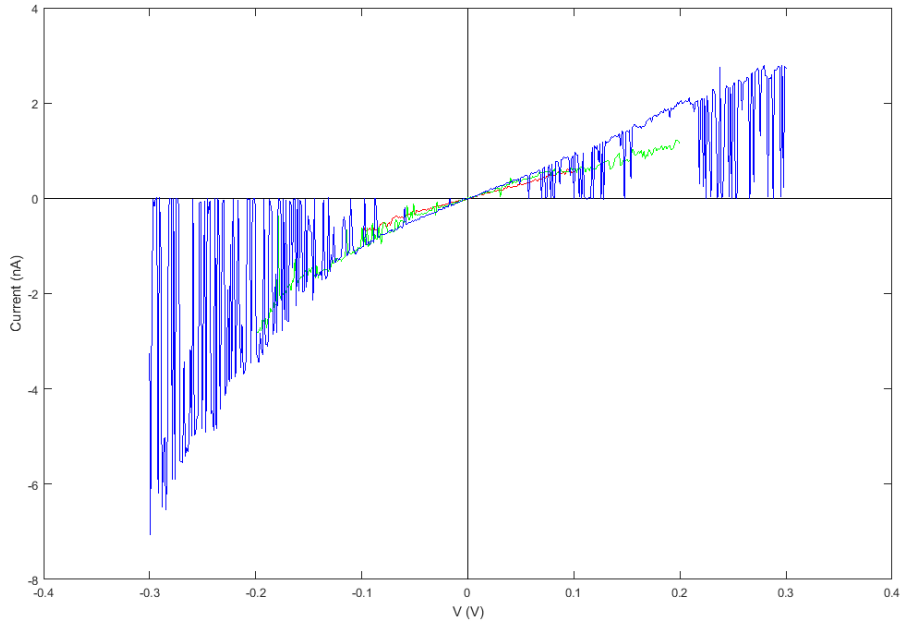

Fig. 9.19 Device C8 from the first batch of assembly. After the the largest sweep to 0.3 V shown from Fig. 9.17, the RTS occures at lower external bias than before, which may be the result of asymmetric length of the chains of the nanocrystal linker molecules to source and drain contacts.

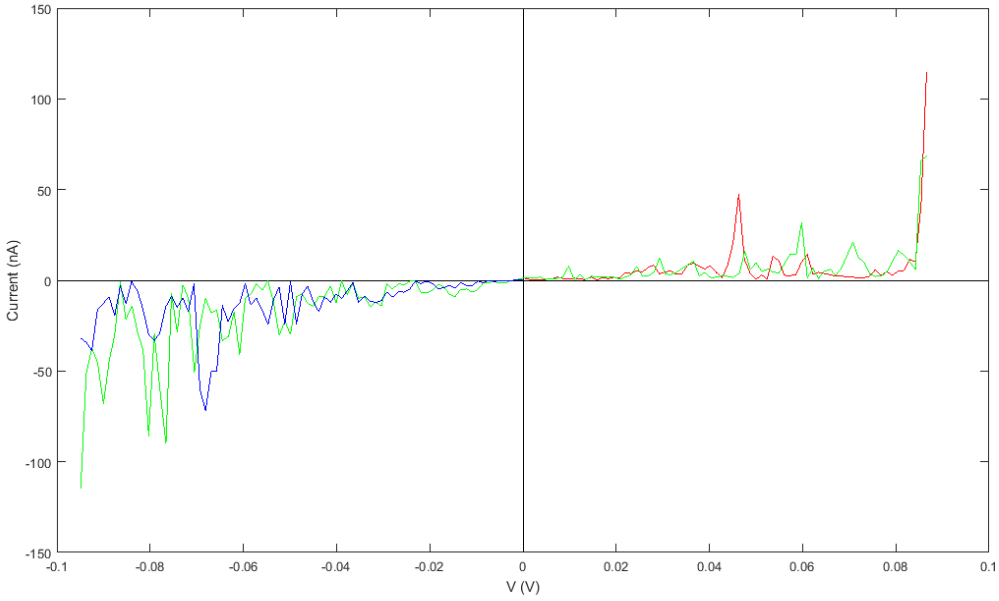

Fig. 9.20 Device C9 from the first batch of assembly, sweeps 16-18.

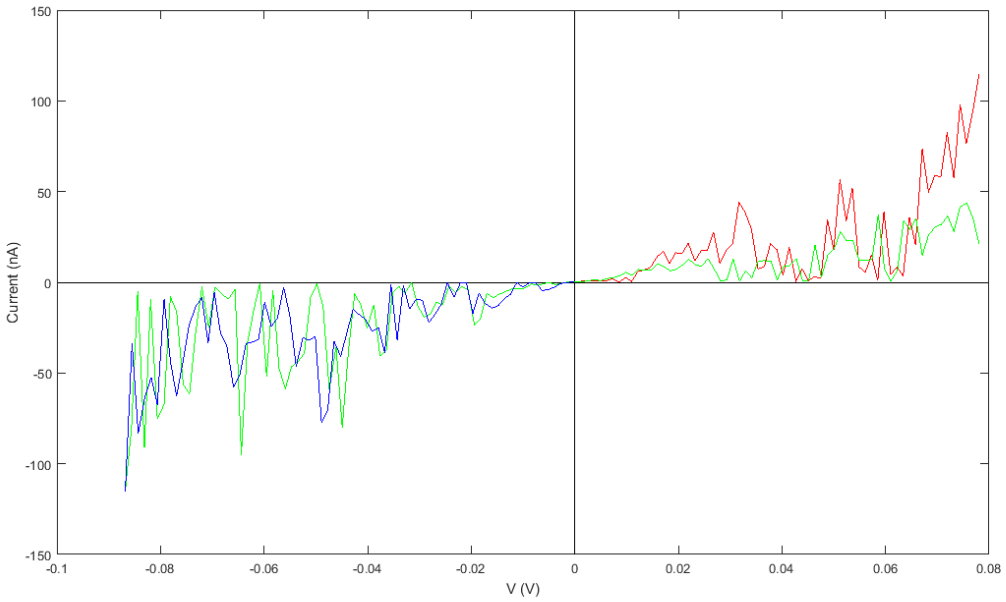

Fig. 9.21 Device C9 from the first batch of assembly, sweeps 19-21.

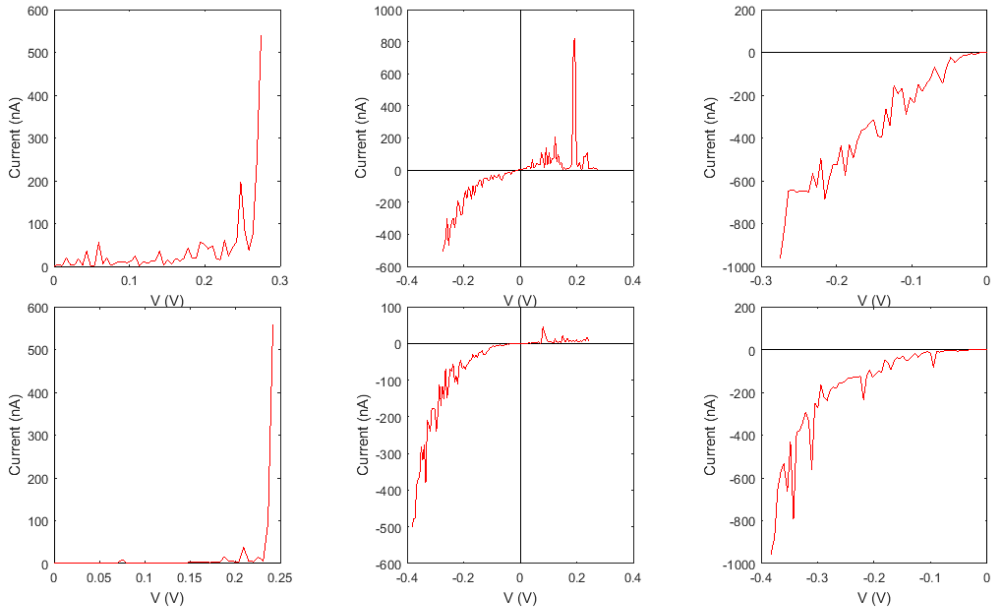

Fig. 9.22 Device D9 from the first batch of assembly. The sweeps on the top row are from sweeps 22 to 24, and at the bottom row are from sweeps 25 to 27. Unlike in Fig. 9.20 and Fig. 9.21, $I-V$ characteristics from device D9 are very similar in both shape and value, except for the spike in the second plot on the top row. If more nanocrystals were accumulating around one metal contact and could be attracted or expelled by the bias, this can possibly explain the differences from device C9 and D9.

Chapter 10

Summary & Future Work

The work for this thesis consists of three projects including an AC magnetic-susceptibility study of $YBa_2Cu_3O_{7-\delta}$, an ionic-liquid-gating study of the Mott insulator Sr_2IrO_4, and a single-electron tunnelling study of self-assembled quantum-dot. In each project, the background information and the experimental design were presented, followed by instrument setup and measurement. The results were discussed and summarised. In this chapter, all three projects will be concluded and some suggestions will be given for the future work.

10.1 $YBa_2Cu_3O_{7-\delta}$ High Pressure Project

The AC magnetic susceptibility of pressurised $YBa_2Cu_3O_{7-\delta}$ at around 90 kbar was measured with externally applied magnetic field as a function of temperature. A diamond-anvil pressure cell was employed to achieve the high hydrostatic pressure during the measurement. A small piece of ruby which can exhibit a shift of R_1 fluorescence line under different pressure was taken as calibrator of pressure. With a series of DC magnetic fields ranging from zero to 9 T, the obtained magnetic susceptibilities generate a phase diagram of vortex melting magnetic field with respect to temperature. A model of vortex-melting line for high-temperature superconductors can fit our data well, matching the experimental data from other experimental techniques too. This supports our method of tuning $YBa_2Cu_3O_{7-\delta}$ into the overdoped region by high pressure, which does not introduce extra chemical disorder into the system.

However, the large background signal in the experiment cannot be explained very well by common sources of noise. Possible explanations were given as the pressure body made of BeCu, the gasket made of MP35, and the distortion of the coils bearing the applied high pressure. Each source needs a separate control experiment to confirm. The suppliers of the

metal components of the pressure cell need to be tracked down to understand the source of the background signal.

10.2 Sr_2IrO_4 Ionic-Liquid-Gating Project

The possibility of ionic-liquid-gating the Mott insulator Sr_2IrO_4 was explored in this project. Single crystals of Sr_2IrO_4 were firstly grown by the flux growth method by heating up the mix of the raw material to high temperature and then slowly cooling down to room temperature. The obtained single crystals were then characterised by resistance and DC magnetic susceptibility measurements to identify their insulating behaviour and the magnetic transition at around 240 K, which confirm their high quality. Following the characterisation, patterning processes on the as-grown single crystal Sr_2IrO_4 were explored. Due to the irregular shape of the as-grown single crystals, focused-ion beam (FIB) lithography was employed to realise the aim. A single crystal was first naturally cleaved into flakes by the scotch-tape method and then transferred to a SiO_2/Si substrate for fabrication. Both large flakes and small flakes were tested and the possibly best recipe was given.

In a control experiment on $SrTiO_3$, the ionic liquid gating technique was firstly realised. A practical recipe of fabricating field-effect transistor on $SrTiO_3$ was explored and achieved. The details of positioning ionic liquid precisely onto the gated channel and the correct procedures for gating the material were presented. A metallic $SrTiO_3$ was observed finally at V_g=3 V in the resistance measurement. The resulted sheet resistance is in agreement with the work published, which establishes the effectiveness of the fabrication method and the gating procedures.

The future improvements can be directed to finalising the fabrication of Sr_2IrO_4 using the recipe achieved in this thesis. Repeatable resistance of fabricated Sr_2IrO_4 should be measured to ensure the robustness of the flake and the metal contacts by FIB. Following it, the actual ionic-liquid-gating technique can be applied to Sr_2IrO_4 and compare the resuls with the ungated Sr_2IrO_4.

To obtain the largest gating effect, different ionic liquids can be tested to find a best option.

10.3 PbS Self-Assembled Quantum Dot Project

To study the single-electron transport of quantum dot, both vertical and lateral quantum dot were fabricated. The vertical quantum dots were to be self-assembled into the gap formed by selectively etching away the AlAs barrier sandwiched between two heavily doped n+GaAs

layers. However, in the previous experiment, the AlAs barrier was always found to short out the gap. Despite detailed examination, simulation, and testing of all the stages of processing, the leakage could not be removed. The final possible source may be the wafer itself with some carriers diffusing from the top n+GaAs layer into the AlAs barrier beneath. Diffusion is much more likely to be caused during growth.

To confirm this assumption, wafers from other laboratories or commercially bought are good choices for test. It is also suggested that dry etching (such as RIE or ICP) is to be employed for all etching processesas it will not leave impurities on the wafer surface. From the SEM photo shown in the previous chapter, it can be observed that some white remains were left after wet acid etching. It may be better to avoid this contamination.

The lateral quantum dot device was then studied. The device was fabricated by collaborators in Japan using a electroplating technique to form an extremely small gap of nanometer scale between Au contacts. A self-assembly process was then applied to these devices to form a layer of PbS nanocrystal attached to a sparse arrays of linker molecules (thiols) attached to the Au contacts. The assembled nanocrystal devices were measured at 30 K in a cryogenic probe station. 24 h immersion in octandithiol seems to attach more than one nanocrystal to a nanogap and the results were presented in the form of exponential $I-V$ characteristics through the nanogap. The attached nanocrystals were not stable enough to exhibit continuous and smooth $I-V$ curves gave more random-telegraph signals with increasing of source-drain bias. The effect of air exposure to nanocrystals was also studied. 30 min of air exposure at low atmospheric pressure seems to be enough to oxidise PbS nanocrystals and to create an insulating shell on the surface. The $I-V$ curve, from these oxidised PbS devices always showed no conduction.

The immersion time in octanedithiol should be shortened to 12 h or less. From the SEM pictures taken for Au films immersed in octanedithiol for different periods of time, similar number densities of nanocrystals were observed. However, the resulting $I-V$ curves tell a different story. Thus the quality of SEM images should be improved to better identify the assembled nanocrystals. Then an optimum immersion time can be obtained for the actual devices.

References

[1] Rajvir Singh, R. Lal, U. C. Upreti, D. K. Suri, A. V. Narlikar, V. P. S. Awana, J. Albino Aguiar, and Md. Shahabuddin. Superconductivity in zn-doped tetragonal $LaBaCu_3O_{3-\delta}$ systems. *Physical Review B*, 55:1216–1222, Jan 1997.

[2] JD Jorgensen, MA Beno, Di G Hinks, L Soderholm, KJ Volin, RL Hitterman, JD Grace, Ivan K Schuller, CU Segre, K Zhang, et al. Oxygen ordering and the orthorhombic-to-tetragonal phase transition in $YBa_2Cu_3O_{7-x}$. *Physical Review B*, 36(7):3608, 1987.

[3] Gianni Blatter, Mikhail V Feigel'man, Vadim B Geshkenbein, Anatoly I Larkin, and Valerii M Vinokur. Vortices in high-temperature superconductors. *Reviews of Modern Physics*, 66:1125–1388, Oct 1994.

[4] JL Tallon, C Bernhard, H Shaked, RL Hitterman, and JD Jorgensen. Generic superconducting phase behavior in high-T_c cuprates: T_c variation with hole concentration in $YBa_2Cu_3O_{7-\delta}$. *Physical Review B*, 51(18):12911, 1995.

[5] Ruixing Liang, D. A. Bonn, and W. N. Hardy. Discontinuity of reversible magnetization in untwinned YBCO single crystals at the first order vortex melting transition. *Physical Review Letters*, 76:835–838, Jan 1996.

[6] PL Alireza, GH Zhang, W Guo, J Porras, T Loew, Y-T Hsu, GG Lonzarich, M Le Tacon, B Keimer, and Suchitra E Sebastian. Accessing the entire overdoped regime in pristine $YBa_2Cu_3O_{6+x}$ by application of pressure. *Physical Review B*, 95(10):100505, 2017.

[7] Jungho Kim, D Casa, MH Upton, T Gog, Young-June Kim, JF Mitchell, M Van Veenendaal, M Daghofer, J van Den Brink, G Khaliullin, et al. Magnetic excitation spectra of Sr_2IrO_4 probed by resonant inelastic X-ray scattering: establishing links to cuprate superconductors. *Physical Review Letters*, 108(17):177003, 2012.

[8] M Reehuis, C Ulrich, K Prokeš, A Gozar, G Blumberg, Seiki Komiya, Yoichi Ando, P Pattison, and B Keimer. Crystal structure and high-field magnetism of La_2CuO_4. *Physical Review B*, 73(14):144513, 2006.

[9] BJ Kim, Hosub Jin, SJ Moon, J-Y Kim, B-G Park, CS Leem, Jaejun Yu, TW Noh, C Kim, S-J Oh, et al. Novel $J_{\text{eff}} = 1/2$ Mott state induced by relativistic spin-orbit coupling in Sr_2IrO_4. *Physical Review Letters*, 101(7):076402, 2008.

[10] G Cao, J Bolivar, S McCall, JE Crow, and RP Guertin. Weak ferromagnetism, metal-to-nonmetal transition, and negative differential resistivity in single-crystal Sr_2IrO_4. *Physical Review B*, 57(18):R11039, 1998.

[11] D Haskel, G Fabbris, Mikhail Zhernenkov, PP Kong, CQ Jin, G Cao, and M Van Veenendaal. Pressure tuning of the spin-orbit coupled ground state in Sr_2IrO_4. *Physical Review Letters*, 109(2):027204, 2012.

[12] J George Bednorz and K Alex Müller. Possible high T_c superconductivity in the Ba-La-Cu-O system. *Zeitschrift f ur Physik B Condensed Matter*, 64(2):189–193, 1986.

[13] A Schilling, M Cantoni, JD Guo, and HR Ott. Superconductivity above 130 K in the Hg-Ba-Ca-Cu-O system. *Nature*, 363(6424):56, 1993.

[14] Ruixing Liang, DA Bonn, and WN Hardy. Evaluation of CuO_2 plane hole doping in $YBa_2Cu_3O_{6+x}$ single crystals. *Physical Review B*, 73:180505, May 2006.

[15] JT Kucera and JC Bravman. Transport characterization of calcium-doped $YBa_2Cu_3O_{7-\delta}$ thin films. *Physical Review B*, 51:8582–8590, Apr 1995.

[16] Gang Xiao and NS Rebello. Electrical transport and superconductivity in the $(Y_{0.8}Ca_{0.2})Ba_2Cu_3O_y$ system with variable oxygen content. *Physica C: Superconductivity*, 211(3-4):433–439, 1993.

[17] DG Hawthorn, SY Li, M Sutherland, Etienne Boaknin, RW Hill, C Proust, F Ronning, MA Tanatar, Johnpierre Paglione, Louis Taillefer, et al. Doping dependence of the superconducting gap in $Tl_2Ba_2CuO_{6+\delta}$ from heat transport. *Physical Review B*, 75:104518, Mar 2007.

[18] A.I. Ekimov, Al.L. Efros, and A.A. Onushchenko. Quantum size effect in semiconductor microcrystals. *Solid State Communications*, 56(11):921 – 924, 1985.

[19] Smita Pathak, Elizabeth Cao, Marie C Davidson, Sungho Jin, and Gabriel A Silva. Quantum dot applications to neuroscience: new tools for probing neurons and glia. *Journal of Neuroscience*, 26(7):1893–1895, 2006.

[20] Cyril Proust, Etienne Boaknin, RW Hill, Louis Taillefer, and AP Mackenzie. Heat transport in a strongly overdoped cuprate: Fermi liquid and a pure d-wave BCS superconductor. *Physical Review Letters*, 89:147003, Sep 2002.

[21] Leon N. Cooper. Bound electron pairs in a degenerate Fermi gas. *Physical Review*, 104:1189–1190, Nov 1956.

[22] Michael Tinkham. *Introduction to superconductivity*. Dover Publications, 2015.

[23] J. Bardeen, L. N. Cooper, and J. R. Schrieffer. Microscopic theory of superconductivity. *Physical Review*, 106:162–164, Apr 1957.

[24] J. Bardeen, L. N. Cooper, and J. R. Schrieffer. Theory of superconductivity. *Physical Review*, 108:1175–1204, Dec 1957.

[25] Dirk Van Delft and Peter Kes. The discovery of superconductivity. *Physics Today*, 63(9):38–43, 2010.

[26] C. W. Chu. Superconductivity at higher temperatures in the Hg-Ba-Ca-Cu-O compound system. *Journal of Superconductivity*, 7(1):1–7, Feb 1994.

[27] Ruixing Liang, Douglas A Bonn, and Walter N Hardy. Growth of YBCO single crystals by the self-flux technique. *Philosophical Magazine*, 92(19-21):2563–2581, 2012.

[28] MR Presland, JL Tallon, RG Buckley, RS Liu, and NE Flower. General trends in oxygen stoichiometry effects on T_c in Bi and Tl superconductors. *Physica C: Superconductivity*, 176(1-3):95–105, 1991.

[29] M. K. Wu, J. R. Ashburn, C. J. Torng, P. H. Hor, R. L. Meng, L. Gao, Z. J. Huang, Y. Q. Wang, and C. W. Chu. Superconductivity at 93 K in a new mixed-phase Y-Ba-Cu-O compound system at ambient pressure. *Physical Review Letters*, 58:908–910, Mar 1987.

[30] N-C Yeh, C-T Chen, G Hammerl, J Mannhart, A Schmehl, CW Schneider, RR Schulz, S Tajima, K Yoshida, D Garrigus, et al. Evidence of doping-dependent pairing symmetry in cuprate superconductors. *Physical Review Letters*, 87:087003, Aug 2001.

[31] B Fisher, J Genossar, CG Kuper, L Patlagan, GM Reisner, and A Knizhnik. Effects of substituting calcium for yttrium on the properties of $YBa_2Cu_3O_{7-\delta}$. *Physical Review B*, 47:6054–6059, Mar 1993.

[32] H. A. Ludwig, R. Quenzel, S. I. Schlachter, F. W. Hornung, K. Grube, W. H. Fietz, and T. Wolf. Hydrostatic and uniaxial pressure effect on T_c of $YBa_2Cu_3O_x$. *Journal of Low Temperature Physics*, 105(5):1385–1390, Dec 1996.

[33] Sergey L. Bud'ko, Yong Liu, Thomas A. Lograsso, and Paul C. Canfield. Hydrostatic and uniaxial pressure dependence of superconducting transition temperature of KFe_2As_2 single crystals. *Physical Review B*, 86:224514, Dec 2012.

[34] U. Welp, M. Grimsditch, S. Fleshler, W. Nessler, J. Downey, G. W. Crabtree, and J. Guimpel. Effect of uniaxial stress on the superconducting transition in $YBa_2Cu_3O_7$. *Physical Review Letters*, 69:2130–2133, Oct 1992.

[35] A. P. Drozdov, M. I. Eremets, I. A. Troyan, V. Ksenofontov, and S. I. Shylin. Conventional superconductivity at 203 kelvin at high pressures in the sulfur hydride system. *Nature*, 525(7567):73–76, 2015.

[36] A. A. Abrikosov. Nobel lecture: Type-II superconductors and the vortex lattice. *Reviews of Modern Physics*, 76:975–979, Dec 2004.

[37] P Dai, BC Chakoumakos, GF Sun, KW Wong, Y Xin, and DF Lu. Synthesis and neutron powder diffraction study of the superconductor $HgBa_2Ca_2Cu_3O_{8+\delta}$ by Tl substitution. *Physica C: Superconductivity*, 243(3-4):201–206, 1995.

[38] Charles Kittel et al. *Introduction to solid state physics*, volume 8. Wiley New York, 1976.

[39] Akihiro Ino, Changyoung Kim, Takashi Mizokawa, Zhi-Xun Shen, Atsushi Fujimori, Masamitsu Takaba, Kenji Tamasaku, Hiroshi Eisaki, and Shinichi Uchida. Fermi surface and band dispersion in $La_{2-x}Sr_xCuO_4$. *Journal of the Physical Society of Japan*, 68(5):1496–1499, 1999.

[40] Ch Renner, Bernard Revaz, J-Y Genoud, K Kadowaki, and Ø Fischer. Pseudogap precursor of the superconducting gap in under-and overdoped $Bi_2Sr_2CaCu_2O_{8+\delta}$. *Physical Review Letters*, 80(1):149, 1998.

[41] JW Loram, KA Mirza, JR Cooper, and WY Liang. Electronic specific heat of $YBa_2Cu_3O_{6+x}$ from 1.8 to 300 K. *Physical Review Letters*, 71(11):1740, 1993.

[42] Tom Timusk and Bryan Statt. The pseudogap in high-temperature superconductors: an experimental survey. *Reports on Progress in Physics*, 62(1):61, 1999.

[43] IM Vishik, WS Lee, RH He, M Hashimoto, Z Hussain, TP Devereaux, and ZX Shen. ARPES studies of cuprate Fermiology: superconductivity, pseudogap and quasiparticle dynamics. *New Journal of Physics*, 12(10):105008, 2010.

[44] Patrick A. Lee, Naoto Nagaosa, and Xiao-Gang Wen. Doping a Mott insulator: Physics of high-temperature superconductivity. *Reviews of Modern Physics*, 78:17–85, Jan 2006.

[45] Electron correlations in narrow energy bands. *Proceedings of the Royal Society of London A: Mathematical, Physical and Engineering Sciences*, 276(1365):238–257, 1963.

[46] V. J. Emery, S. A. Kivelson, and H. Q. Lin. Phase separation in the t-J model. *Physical Review Letters*, 64:475–478, Jan 1990.

[47] K. Miyake, S. Schmitt-Rink, and C. M. Varma. Spin-fluctuation-mediated even-parity pairing in heavy-fermion superconductors. *Physical Review B*, 34:6554–6556, Nov 1986.

[48] Jorge Quintanilla and Chris Hooley. The strong-correlations puzzle. *Physics World*, 22(06):32, 2009.

[49] Tôru Moriya. Developments of the theory of spin fluctuations and spin fluctuation-induced superconductivity. *Proceedings of the Japan Academy, Series B*, 82(1):1–16, 2006.

[50] Toru Moriya. *Spin fluctuations in itinerant electron magnetism*, volume 56. Springer Science & Business Media, 2012.

[51] DJ Scalapino, E Loh Jr, and JE Hirsch. D-wave pairing near a spin-density-wave instability. *Physical Review B*, 34(11):8190, 1986.

[52] K Miyake, S Schmitt-Rink, and CM Varma. Spin-fluctuation-mediated even-parity pairing in heavy-fermion superconductors. *Physical Review B*, 34(9):6554, 1986.

[53] Marc T Thompson and Richard D Thornton. Flux-canceling electrodynamic maglev suspension. II. test results and scaling laws. *IEEE Transactions on Magnetics*, 35(3):1964–1975, 1999.

[54] Alexei A Abrikosov. On the magnetic properties of superconductors of the second group. *Sov. Phys. JETP*, 5:1174–1182, 1957.

[55] P Gr De Gennes and J Matricon. Collective modes of vortex lines in superconductors of the second kind. *Reviews of Modern Physics*, 36(1):45, 1964.

[56] Uwe Essmann and Hermann Träuble. The magnetic structure of superconductors. *Scientific American*, 224(3):74–85, 1971.

[57] PL Gammel, DJ Bishop, GJ Dolan, JR Kwo, CA Murray, LF Schneemeyer, and JV Waszczak. Observation of hexagonally correlated flux quanta in $YBa_2Cu_3O_7$. *Physical Review Letters*, 59(22):2592, 1987.

[58] James S Schilling. What high pressure studies have taught us about high-temperature superconductivity. In *Frontiers of high pressure research II: Application of high pressure to low-dimensional novel electronic materials*, pages 345–360. Springer, 2001.

[59] Nikolay Plakida. *High-Temperature Cuprate Superconductors: Experiment, Theory, and Applications*, volume 166. Springer Science & Business Media, 2010.

[60] John Robert Schrieffer and James S Brooks. *Handbook of high-temperature superconductivity: theory and experiment*. Springer New York, 2007.

[61] H Takagi, T Ido, S Ishibashi, M Uota, S Uchida, and Y Tokura. Superconductor-to-nonsuperconductor transition in $(La_{1-x}Sr_x)_2CuO_4$ as investigated by transport and magnetic measurements. *Physical Review B*, 40(4):2254, 1989.

[62] Deirdre D Ragan, David R Clarke, and David Schiferl. Silicone fluid as a high-pressure medium in diamond anvil cells. *Review of Scientific Instruments*, 67(2):494–496, 1996.

[63] Stanley Block and Gasper Piermarini. The diamond cell stimulates high-pressure research. *Physics Today*, 29:44–55, 1976.

[64] BJ Ramshaw, James Day, Baptiste Vignolle, David LeBoeuf, P Dosanjh, Cyril Proust, Louis Taillefer, Ruixing Liang, WN Hardy, and DA Bonn. Vortex lattice melting and H_{C2} in underdoped $YBa_2Cu_3O_y$. *Physical Review B*, 86(17):174501, 2012.

[65] G Grissonnanche, O Cyr-Choiniere, F Laliberté, S René De Cotret, A Juneau-Fecteau, S Dufour-Beauséjour, M-E Delage, D LeBoeuf, J Chang, BJ Ramshaw, et al. Direct measurement of the upper critical field in cuprate superconductors. *Nature Communications*, 5:3280, 2014.

[66] T Shibauchi, N Katase, T Tamegai, and K Uchinokura. Temperature dependence of anisotropic penetration depth in under-and overdoped $Bi_2Sr_2CaCu_2O_{8+y}$. *Physica C: Superconductivity*, 264(3-4):227–232, 1996.

[67] T. Pereg-Barnea, P. J. Turner, R. Harris, G. K. Mullins, J. S. Bobowski, M. Raudsepp, Ruixing Liang, D. A. Bonn, and W. N. Hardy. Absolute values of the London penetration depth in $YBa_2Cu_3O_{6+y}$ measured by zero field ESR spectroscopy on Gd doped single crystals. *Physical Review B*, 69:184513, May 2004.

[68] J Lu, VJ Toplosky, RE Goddard, and K Han. Low temperature physical properties of Co-35Ni-20Cr-10Mo alloy MP35N®. *Cryogenics*, 86:106–111, 2017.

[69] Q Huang, JL Soubeyroux, O Chmaissem, I Natali Sora, A Santoro, RJ Cava, JJ Krajewski, and WF Peck Jr. Neutron powder diffraction study of the crystal structures of Sr_2RuO_4 and Sr_2IrO_4 at room temperature and at 10 K. *Journal of Solid State Chemistry*, 112(2):355–361, 1994.

[70] MA Subramanian, MK Crawford, RL Harlow, T Ami, JA Fernandez-Baca, ZR Wang, and DC Johnston. Sr_2RhO_4 and Sr_2IrO_4: Structural and magnetic studies of 4*d* and 5*d* transition metal analogs of La_2CuO_4. *Physica C: Superconductivity*, 235:743–744, 1994.

[71] NS Kini, AM Strydom, HS Jeevan, C Geibel, and S Ramakrishnan. Transport and thermal properties of weakly ferromagnetic Sr_2IrO_4. *Journal of Physics: Condensed Matter*, 18(35):8205, 2006.

[72] OB Korneta, Tongfei Qi, S Chikara, S Parkin, LE De Long, Pedro Schlottmann, and G Cao. Electron-doped $Sr_2IrO_{4-\delta}$ ($0 \leq \delta \leq 0.04$): Evolution of a disordered $J_{\text{eff}} = 1/2$ Mott insulator into an exotic metallic state. *Physical Review B*, 82(11):115117, 2010.

[73] Y Klein and I Terasaki. Insight on the electronic state of Sr_2IrO_4 revealed by cationic substitutions. *Journal of Physics: Condensed Matter*, 20(29):295201, 2008.

[74] CH Ahn, J-M Triscone, and J Mannhart. Electric field effect in correlated oxide systems. *Nature*, 424(6952):1015, 2003.

[75] Harold Y Hwang, Yoh Iwasa, Masashi Kawasaki, Bernhard Keimer, Naoto Nagaosa, and Yoshinori Tokura. Emergent phenomena at oxide interfaces. *Nature Materials*, 11(2):103, 2012.

[76] Anthony J DeMarco and John Melngailis. Contact resistance of focused ion beam deposited platinum and tungsten films to silicon. *Journal of Vacuum Science & Technology B: Microelectronics and Nanometer Structures Processing, Measurement, and Phenomena*, 19(6):2543–2546, 2001.

[77] Abhishek Motayed, Albert V Davydov, Mark D Vaudin, Igor Levin, John Melngailis, and SN Mohammad. Fabrication of GaN-based nanoscale device structures utilizing focused ion beam induced Pt deposition. *Journal of Applied Physics*, 100(2):024306, 2006.

[78] David C Look. Electrical characterization of GaAs materials and devices. 1989.

[79] Mingyang Li, Wei Han, Xin Jiang, Jaewoo Jeong, Mahesh G Samant, and Stuart SP Parkin. Suppression of ionic liquid gate-induced metallization of $SrTiO_3$ (001) by oxygen. *Nano Letters*, 13(10):4675–4678, 2013.

[80] K Ueno, S Nakamura, H Shimotani, A Ohtomo, N Kimura, T Nojima, H Aoki, Y Iwasa, and M Kawasaki. Electric-field-induced superconductivity in an insulator. *Nature Materials*, 7(11):855, 2008.

[81] Sara Drvarič Talian, Marija Bešter-Rogač, and Robert Dominko. The physicochemical properties of a [DEME][TFSI] ionic liquid-based electrolyte and their influence on the performance of lithium-sulfur batteries. *Electrochimica Acta*, 252:147–153, 2017.

[82] H Van Kempen, PJM Van Bentum, and RTM Smokers. Coulomb blockade effects in STM-type tunnel junctions. *Physica Scripta*, 1992(T42):153, 1992.

[83] U Meirav and EB Foxman. Single-electron phenomena in semiconductors. *Semiconductor Science and Technology*, 11(3):255, 1996.

[84] David L Klein, Paul L McEuen, Janet E Bowen Katari, Richard Roth, and A Paul Alivisatos. An approach to electrical studies of single nanocrystals. *Applied Physics Letters*, 68(18):2574–2576, 1996.

[85] SH Magnus Persson, Linda Olofsson, and Linda Gunnarsson. A self-assembled single-electron tunneling transistor. *Applied Physics Letters*, 74(17):2546–2548, 1999.

[86] DV Averin and KK Likharev. Coulomb blockade of single-electron tunneling, and coherent oscillations in small tunnel junctions. *Journal of Low Temperature Physics*, 62(3-4):345–373, 1986.

[87] George M. Whitesides, Jennah K. Kriebel, and J. Christopher Love. Molecular engineering of surfaces using self-assembled monolayers. *Science Progress*, 88(1):17–48, 2005.

[88] CG Smith, M Pepper, H Ahmed, JEF Frost, DG Hasko, DC Peacock, DA Ritchie, and GAC Jones. The transition from one-to zero-dimensional ballistic transport. *Journal of Physics C: Solid State Physics*, 21(24):L893, 1988.

[89] BJ Van Wees, Leo P Kouwenhoven, CJPM Harmans, JG Williamson, CE Timmering, MEI Broekaart, CT Foxon, and JJ Harris. Observation of zero-dimensional states in a one-dimensional electron interferometer. *Physical Review Letters*, 62(21):2523, 1989.

[90] LP Kouwenhoven, BJ van Wees, W Kool, CJP Ṁ Harmans, AAM Staring, and CT Foxon. Transition from Ohmic to adiabatic transport in quantum point contacts in series. *Physical Review B*, 40(11):8083, 1989.

[91] Yasuo Azuma, Seiichi Suzuki, Kosuke Maeda, Norio Okabayashi, Daisuke Tanaka, Masanori Sakamoto, Toshiharu Teranishi, Mark R Buitelaar, Charles G Smith, and Yutaka Majima. Nanoparticle single-electron transistor with metal-bridged top-gate and nanogap electrodes. *Applied Physics Letters*, 99(7):073109, 2011.

[92] Shinya Kano, Daisuke Tanaka, Masanori Sakamoto, Toshiharu Teranishi, and Yutaka Majima. Control of charging energy in chemically assembled nanoparticle single-electron transistors. *Nanotechnology*, 26(4):045702, 2015.

[93] Yasuo Azuma, Yuto Onuma, Masanori Sakamoto, Toshiharu Teranishi, and Yutaka Majima. Rhombic Coulomb diamonds in a single-electron transistor based on an Au nanoparticle chemically anchored at both ends. *Nanoscale*, 8(8):4720–4726, 2016.

[94] Xinheng Li, Yuhsuke Yasutake, Keijiro Kono, Masayuki Kanehara, Toshiharu Teranishi, and Yutaka Majima. Au nanoparticles chemisorbed by dithiol molecules inserted in alkanethiol self-assembled monolayers characterized by scanning tunneling microscopy. *Japanese Journal of Applied Physics*, 48(4S):04C180, 2009.

[95] Shinya Kano, Kosuke Maeda, Daisuke Tanaka, Masanori Sakamoto, Toshiharu Teranishi, and Yutaka Majima. Chemically assembled double-dot single-electron transistor analyzed by the orthodox model considering offset charge. *Journal of Applied Physics*, 118(13):134304, 2015.

[96] Sotirios Baskoutas and Andreas F. Terzis. Size-dependent band gap of colloidal quantum dots. *Journal of Applied Physics*, 99(1):013708, 2006.

[97] Y. Wang, A. Suna, W. Mahler, and R. Kasowski. PbS in polymers. from molecules to bulk solids. *The Journal of Chemical Physics*, 87(12):7315–7322, 1987.

[98] Xinzheng Lan, Silvia Masala, and Edward H. Sargent. Charge-extraction strategies for colloidal quantum dot photovoltaics. *Nature Materials*, 13(3):233–240, 2014.

[99] Maria Ibáñez, Rachel Korkosz, Zhishan Luo, Pau Riba, Doris Cadavid, Silvia Ortega, Andreu Cabot, and Mercouri G. Kanatzidis. Correction to "Electron Doping in Bottom-Up Engineered Thermoelectric Nanomaterials through HCl-Mediated Ligand Displacement". *Journal of the American Chemical Society*, 137(36):11854–11854, Feb 2015.

[100] Jianbing Zhang, Jianbo Gao, Elisa M. Miller, Joseph M. Luther, and Matthew C. Beard. Diffusion-controlled synthesis of pbs and PbSe quantum dots with in situ halide passivation for quantum dot solar cells. *ACS Nano*, 8(1):614–622, 2013.

[101] Stefan Birner, Tobias Zibold, Till Andlauer, Tillmann Kubis, Matthias Sabathil, Alex Trellakis, and Peter Vogl. Nextnano: general purpose 3-D simulations. *IEEE Transactions on Electron Devices*, 54(9):2137–2142, 2007.

[102] Angang Dong, Xingchen Ye, Jun Chen, Yijin Kang, Thomas Gordon, James M. Kikkawa, and Christopher B. Murray. A generalized ligand-exchange strategy enabling sequential surface functionalization of colloidal nanocrystals. *Journal of the American Chemical Society*, 133(4):998–1006, 2011. PMID: 21175183.

[103] David JH Cant, Karen L Syres, Patrick JB Lunt, Hanna Radtke, Jon Treacy, P John Thomas, Edward A Lewis, Sarah J Haigh, Paul O'Brien, Karina Schulte, et al. Surface properties of nanocrystalline PbS films deposited at the water-oil interface: a study of atmospheric aging. *Langmuir*, 31(4):1445–1453, 2015.

[104] Samantha JO Hardman, Darren M Graham, Stuart K Stubbs, Ben F Spencer, Elaine A Seddon, Ho-Ting Fung, Sandra Gardonio, Fausto Sirotti, Mathieu G Silly, Javeed Akhtar, et al. Electronic and surface properties of PbS nanoparticles exhibiting efficient multiple exciton generation. *Physical Chemistry Chemical Physics*, 13(45):20275–20283, 2011.

[105] Milan Sykora, Alexey Y Koposov, John A McGuire, Roland K Schulze, Olexandr Tretiak, Jeffrey M Pietryga, and Victor I Klimov. Effect of air exposure on surface properties, electronic structure, and carrier relaxation in PbSe nanocrystals. *Acs Nano*, 4(4):2021–2034, 2010.

[106] Stefan Machlup. Noise in semiconductors: spectrum of a two-parameter random signal. *Journal of Applied Physics*, 25(3):341–343, 1954.

[107] MJ Uren, DJ Day, and MJj Kirton. 1/f and random telegraph noise in silicon metal-oxide-semiconductor field-effect transistors. *Applied Physics Letters*, 47(11):1195–1197, 1985.

[108] MJ Uren, MJ Kirton, and S Collins. Anomalous telegraph noise in small-area silicon metal-oxide-semiconductor field-effect transistors. *Physical Review B*, 37(14):8346, 1988.

[109] Akiko Ohata, Akira Toriumi, Masao Iwase, and Kenji Natori. Observation of random telegraph signals: Anomalous nature of defects at the Si/SiO_2 interface. *Journal of Applied Physics*, 68(1):200–204, 1990.

[110] Nuditha Vibhavie Amarasinghe and Zeynep Çelik-Butler. Complex random telegraph signals in 0.06 μm^2 MDD n-MOSFETs. *Solid-State Electronics*, 44(6):1013–1019, 2000.

Appendix A

Device Fabrication Process of Quantum Dot Devices

A.1 Vertical Quantum Dot Device

1. Cleave wafer (W0134, V869) into square samples (11×11 mm^2 for 3×3 chips).
2. Clean the cleaved wafer by ultrasonic bath. Immerse the chip in acetone followed by IPA for 3 min each. Dry with N_2 and bake on hot plate at 150 °C for 1 min to evaporate the solvent on the surface.
3. Layer 1 Mesa Photolithography (top left layer on the mask)
   (a) Spin Shipley 1813 at 5500 rpm for 30 s.
   (b) Bake at 115 °C for 2 min.
   (c) Align the sample to layer 1 and expose for 6.5 s.
   (d) Develop by MF319 for about 50 s + 15 s (develop until pattern can be clearly seen, rinse in DI water and dry by N_2. Do it by 30 s period). Don't over develop it. Use small petri dish.
   (e) Clean the residual photoresist by RF asher for 1 min.
   (f) RIE or wet etching for about 400 nm $\sim$ 500 nm. For wet etchant (H_2O:H_2O_2:H_2SO_4=80:8:1, volume ratio), 1 min will roughly etch 500 nm at room temperature.
   (g) Clean the photoresist by acetone and IPA in ultrasonic bath for 3 min each.
4. Layer 2 First Metal Layer Photolithography (top middle on the mask)

(a) Spin LOR5B by 6000 rpm for 1 min and bake at 180 °C for 10 min.

(b) Spin Shipley 1813 at 5500 rmp for 1 min.

(c) Bake the sample for 1 min at 115 °C.

(d) Aligh to the first metal (layer 2 of the mask) and expose for 6.5 s.

(e) Develop in MF 319 for about 50 s + 15 s, rinse in DI water and dry with N_2.

(f) RF asher to remove the photoresist residual. Do acid etching to remove the oxide layer. Use HCl : H_2O = 1 : 4 for 30 seconds.

(g) Evaporate metal layer by Pd/Ge (= 25 nm/75 nm) using the e-beam evaporator or the pink evaporator.

(h) Use SVC14 in thermal bath (60°C) for 1 h to remove the LOR5B layer. Dry with N_2 gas.

(i) Anneal the evaporated Pd/Ge at 200 °C for 1 min to form the ohmic contacts. The 200 ° is based on our annealer in SP cleanroom. Note that this may not be calibrated properly.

(j) Check the resistance between Pd/Ge electrodes on GaAs by the probe station.

5. Layer 3 Pillar Etch (top right on the mask)

(a) Spin Shipley 1813 at 5500 rpm for 30 s.

(b) Bake the sample for 1 min at 115 °C.

(c) Aligh the sample to layer 3 and expose for 6.5 s.

(d) Develop the sample in MF 319 for 50 s + 15 s until the pattern can be identified clearly. Rinse in DI water and dry with N_2.

(e) Descum the residual photoresist by RF asher for 1 min.

(f) RIE for about 400 nm $\sim$ 500 nm.

6. Layer 4 Polyimide layer (New mask)
The polyimide used in the this layer is the only one currently available in the SP cleanroom. It's a mixture of HD4104 and solution T9039 (3:1) in volume.

(a) Bake sample 3 minutes at 125 °C.

(b) Flush spinner with N_2 to reduce the humidity inside down to $30\% - 40\%$. This roughly takes 3 minutes.

(c) Spin polyimide 60 s with a speed of 7500 rpm (ramp up from $\sim$3000 rpm).

(d) Bake sample 2 minutes at 65 °C and 3 minutes at 90 °C.

(e) Aligh the mask and expose 80 s. (can be doubled for safe)

(f) Wait for at least 5 minutes.

(g) Bake 1 minute at 80 °C.

(h) Develop with PA401D 40 s. Note that polyimide is a negative type. Rinse in PA400R for about 30 s. Be careful with those chemicals, use them only when necessary.

(i) RF 2 minutes.

(j) Bake in tube furnace 1 hour at 250 °C. Ramp up with a rate of 125 °C/h. Adjust gas flow rate to be 1 unit.

7. Layer 5 Second Metal Layer Photolithography (bottom middle on the mask)

(a) Spin LOR5B by 6000 rpm for 1 min and bake at 180 °C for 10 min.

(b) Spin Shipley 1813 photoresist at 5500 rpm for 1min.

(c) Bake the sample for 1 min at 115 °C.

(d) Align the sample to the second metal layer and expose for 6.5 s.

(e) Develop in MF 319 for about 50 s + 15 s and rinse in DI water and dry by N_2.

(f) RF asher for 1 min to remove the photoresist residual. Use HCl : H_2O = 1 : 4 for 30 seconds.

(g) Metal evaporation (Ti/Au = 25 nm/175 nm).

(h) Lift off by SVC14 in thermal bath (60°C) for 1 h to remove the LOR5B layer. Use brush when necessary.

8. Layer 6 Photoresist window (bottom right on the mask)

(a) Spin Shipley 1805 photoresist for 1 min at 7000 rpm using the right spinner.

(b) Bake the sample for 2 min at 115 °C.

(c) Align the sample to the layer 6 and expose for 13 s.

(d) Develop in MF 319 for about 50 s+ 10 s until a clear pattern shows. Rinse in DI water and dry with N_2.

(e) RF for 1 min.

(f) Bake at 115 °C for 3 more minutes to make it harder to resist BHF and other chemicals.

9. HF etching through the photoresist window. BHF for 2 min with 100 nm/min etching rate. Dry with N_2 gas.

10. Fill in the nanocrystals PbS.

    (a) Drop BHF etched sample into thiel solution (1 mM/L or 1 m mol/L) immediately after it's dried.

    (b) Leave the sample in thiel for 30 minutes. Transfer the bottle with thiel and device to OE glovebox.

    (c) Clean the thiel remain by IPA with spinner (30s $\times$ 3, 2000 rpm). Transfer the device into nanocrystal solution in glovebox filled with nitrogen. Wait for 24 hours.

    (d) Wash away the nanocrystals remaining on the surface by octane (This is also the solvent of nanocrystals.) with spinner (30s $\times$ 4, 2000 rpm).

    (e) Put device in a bottle and seal it in glovebox.

    (f) Transfer device back to SP cleanroom and quickly spin a layer of photoresist on the top to protect the opened gaps. Do edge bead to uncover the bonding pads.

The sample is ready to cut and bond. Use wedge bonder and ion fan to avoid the possible static charge which may potentially break the device.

Below is the print of the mask design used for fabricating vertical quantum dot device.

A.2 Lateral Quantum Dot Device

1. Use electron ebeam lithograohy to thermally deposite a very thin layer gold on the destined suface.

2. Apply electrodeopsition with the previously deposited thin gold layer as a electrode.

3. Check the device under SEM to confirm the quality of devices.

A.3 Self-assembly Process of Nanocrystal

1. Ligand exchange process

    (a) Well mix 0.5 ml PbS nanocrystal solution (25 mg/ml) and 0.5 ml 10% (volume ratio) C10S solution for 10 minutes.

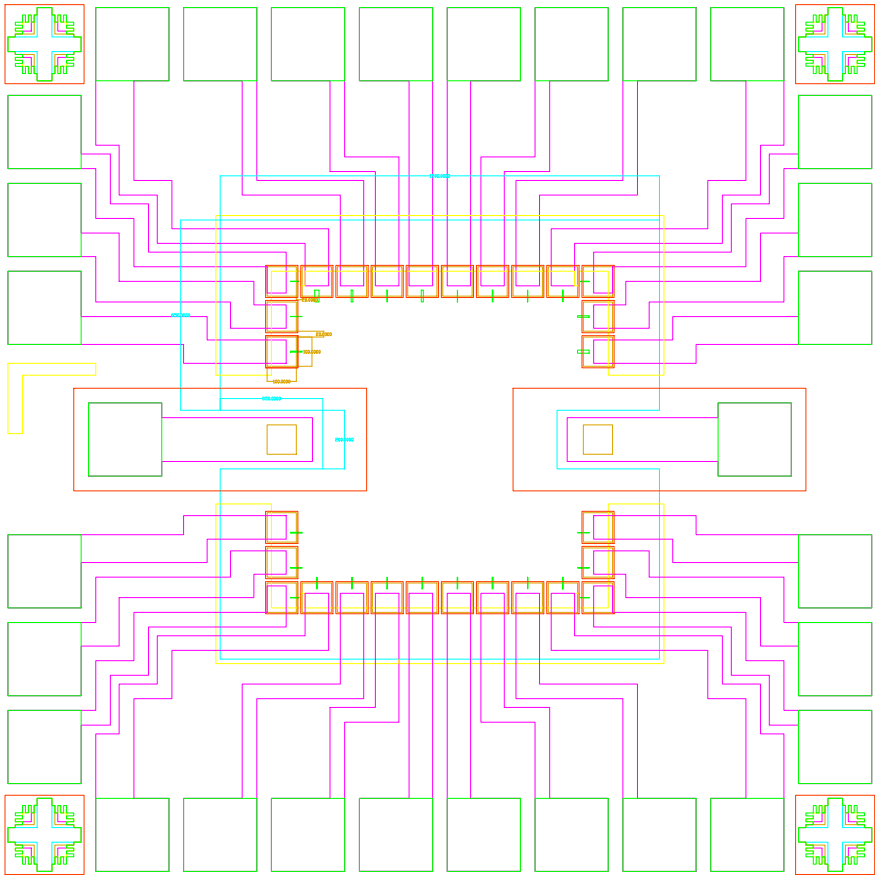

Fig. A.1 Mask desige for vertrical quantum dot device.

   (b) Add 6 ml acetone to the mixture of the previous step and centrigue it for 1 minute at 4000 rpm.

   (c) Decant acetone and dry the nanocrystal with flow nitrogen.

   (d) Add 1 ml toluene and heat at 60 °C for few minutes until the nanocrystals are homogeniously distributed in tolune.

   (e) The concentration of the finished nanocrystal solution is 12.5 mg/ml. Dilute it more to the wanted concentration. For our case, it is 1 mM.

2. Immerse the toluene-cleaned chip into 1 mM C6S solution for 24 hours. Rinse it by toluene and dry it with nitrogen flow.

3. Immerse the chip into 1 mM C8S2 solution for 24 hours. Rinse it by toluene and dry it wiht nitrogen flow.

4. Immerse the chip into 1 mM PbS solution with C10S ligand for 24 hours. Rinse it by toluene and dry it with nitrogen flow.

5. The chip is ready for measurement. Seal it in a box with parafilm and tranfer it quickly to probe station to recude the possible exposure to the air.